UNIVERSIDAD DE CHILE
FACULTAD DE CIENCIAS FÍSICAS Y MATEMÁTICAS
DEPARTAMENTO DE ASTRONOMÍA

GAS-PHASE ABUNDANCES OF THE MILKY WAY PROBED BY QUASAR SIGHTLINES

TESIS PARA OPTAR AL GRADO DE
MAGÍSTER EN CIENCIAS, MENCIÓN ASTRONOMÍA

FELIPE IGNACIO CORRO GUERRA

PROFESOR GUÍA:
SEBASTIAN LOPEZ MORALES

PROFESOR CO-GUÍA:
TRYSTYN MUNRO BERG

MIEMBROS DE LA COMISIÓN:
VALENTINO GONZÁLEZ CONVARVALÁN
RENÉ MÉNDEZ BUSSARD

SANTIAGO DE CHILE
2024

Resumen

Abundancias de la fase gaseosa de la Vía Láctea sondeado por lineas de vision de quásares

El medio circumgaláctico (CGM) media los procesos cruciales que regulan la formación de estrellas en las galaxias al restringir la entrada de gas prístino del medio intergaláctico (IGM) y las salidas de gas enriquecido con metales del medio interestelar (ISM). El estudio de la composición química y cinemática de su gas ha llevado a una mejor comprensión de la historia de la formación estelar de una galaxia. En esta tesis, he utilizado espectros UV de espectros de archivo HST/COS de 209 QSOs a $z = 0.002 - 1.648$ para estudiar los reservorios de gas de la Vía Láctea (MW) en absorción tomográficamente. De cada uno de los espectros UV de la muestra, he derivado densidades de columna para varios elementos (H, Fe, Ni, C, Si, S, Al) usando perfiles de Voigt para modelar los perfiles de absorción y encontré que ~ 38 de las líneas de visión presentan N(H I) lo suficientemente alto como para ser llamado *Damped Lyman-alpha systems* (DLAs). La metalicidad resultante y $[\alpha/\mathrm{Fe}]$ en cada línea de visión muestran variaciones impulsadas por diferencias químicas en lugar de variaciones impulsadas por la incertidumbre. Estas variaciones se contrastan con los resultados de la literatura de 314 sistemas Damped Lyman-α únicos encontrados en una sola línea de visión QSO.

Los resultados pueden resumirse como sigue: 1) Para las líneas de visión DLA de la Vía Láctea la metalicidad media ponderada N(H I) es $[\mathrm{M/H}] = -0.4 \pm 0.2$, donde las metalicidades más bajas se pueden encontrar en la mayoría de los entornos ricos en H I. 2) La desviación estándar en metalicidad encontrada en $z = 0$ en la MW es 40 % de la desviación estándar en metalicidad medida en DLAs de $z \sim 0$ a $z \sim 5$. Esto significa que las variaciones químicas dentro de una sola galaxia son un componente significativo de la dispersión en la metalicidad a la relación z. 3) La media $[\alpha/\mathrm{Fe}]$ medida en la MW es 0.5 dex superior a la misma media medida en los DLA, lo que significa que es probable que provengan de diferentes poblaciones de galaxias. Asumiendo que la condensación a polvo afecta a ambas poblaciones de DLA de manera similar, el $[\alpha/\mathrm{Fe}]$ de la MW está más de acuerdo con los patrones observados en las estrellas de MW, por otro lado, los DLA de alto z $[\alpha/\mathrm{Fe}]$ están más de acuerdo con los patrones observados en las galaxias enanas. Esto significa que el tipo de galaxia dominante en los huéspedes DLA sea probablemente las galaxias enanas.

Abstract

The circumgalactic medium (CGM) mediates the crucial processes that regulate star formation in galaxies by constraining the inflow of pristine gas from the intergalactic medium (IGM) and outflows of metal-enriched gas from the interstellar medium (ISM). Studying the chemical composition and kinematics of its gas has led to a better understanding of the star formation history of a galaxy. In this thesis, I have used UV spectra from HST/COS archival spectra of 209 QSOs at $z = 0.002 - 1.648$ to study the gas reservoirs of the Milky Way (MW) in absorption tomographically. From each UV spectra in the sample, I have derived column densities for several elements (H, Fe, Ni, C, Si, S, Al) using Voigt profile fitting and found that $\sim 38\%$ of the sightlines present N(H I) high enough to be called *Damped Lyman-α systems* (DLAs). The resulting metallicity and [α/Fe] at each sightline show variations driven by chemical differences rather than uncertainty-driven variations. These variations are contrasted with literature results from 314 unique DLAs found on a single QSO sightline at $0.008 < z < 5.179$.

The results can be summarized as follows: 1) For the Milky Way DLA sightlines the N(H I) weighted mean metallicity is $[\mathrm{M/H}] = -0.4 \pm 0.2$, where the lowest metallicities can be found in the most H I-rich environments. 2) The standard deviation in metallicity found at $z = 0$ in the MW is 40% of the standard deviation in metallicity measured in DLAs from $0.008 < z < 5.179$. This means that chemical variations within a single galaxy are a significant component of the scatter in the metallicity to z relation. 3) The mean [α/Fe] measured in the MW is +0.5 dex higher than the same mean measured in DLAs, meaning MW DLAs are likely to come from a different galaxy population compared to DLAs at higher z. Assuming dust depletion affects both DLA populations similarly, the MW's [α/Fe] agrees more with the patterns observed in MW stars, on the other hand, high-z DLAs' [α/Fe] is in closer agreement with patterns observed in dwarf galaxies. This means that the dominant galaxy type in DLA hosts is likely to be dwarf galaxies.

Estoy sobre hombros de gigantes y gracias a ellos el horizonte es cada vez más claro.

Acknowledgments

Mis mayores agradecimientos son para mis padres José Luis Corro, Paula Guerra y mi hermana Katherine Corro. Ellos son los primeros que creyeron en mi, nunca lo han dudado, y su apoyo me ha llevado a donde estoy.

A mi pareja Francisca Cordero le doy las gracias por haber sido siempre un pilar de apoyo, sobretodo cuando más lo necesité, por haberme ha acompañado en los momentos claves de esta tesis y por el amor que hemos podido cultivar juntos.

Los amigos que conocí en la Universidad de Chile me acogieron en este nuevo ambiente fuera de mi casa e hicieron de Santiago un lugar acogedor. Me gustaría agradecer especialmente a Marie Rodriguez, Melissa Aguilar, Alejandra Meza, Paula Cáceres, Aiswarya Arun, Silvio Ulloa y Benjamin Navarrete. También quiero agradecer a quienes conocí en la PUCV y me acompañaron en todo aunque estudiemos en otras universidades, en especial a Pablo Orellana y Soraya Sanchez Meyer.

Quiero agradecer encarecidamente a Trystyn Berg por ser desde siempre un buen profesor y supervisor conmigo, siempre tuvo palabras de apoyo cuando las necesité y espero con ansias trabajar con él nuevamente. También quiero agradecer profundamente a Sebastián Lopez, quien siempre tuvo altas expectativas de mi y me motivó a siempre buscar algo más allá. Adicionalmente me gustaría agradecer a Nicolás Tejos por guiarme en mi primera investigación astronómica y me dió las herramientas y motivación para postular a un magíster en la Universidad de Chile.

A los miembros de la comisión por sus comentarios y notas, los que me permitieron crear la mejor versión de mi tesis.

Finalmente quiero agradecer a la Universidad de Chile por permitirme estudiar y desarrollarme en un ambiente que me permitió crecer académicamente y personalmente.

Table of content

List of Tables

List of Figures

Chapter 1

Introduction

1.1 Motivation for this work

The chemical composition of the gas in a galaxy is governed by the accretion of pristine gas from the intergalactic medium (IGM) to the circumgalactic medium (CGM; Tumlinson et al. 2017). The global process that controls the ejection, accretion, and recycling of gas in a galaxy is called the *baryon cycle*. The most sensitive technique to probe the very diffuse gas around galaxies has proven to be quasar sightline spectroscopy, which studies the absorption lines foreground galaxies imprint into the spectra of bright background quasars.

Quasars (QSOs) are energetic astrophysical sources powered by accretion onto supermassive black holes in galaxies and present unique observational signatures that cover the full electromagnetic spectrum over more than twenty orders of magnitude in frequency (Padovani et al. 2017). The light from QSO that we see on Earth has the chemical composition of all the gas that happened to be between us and the QSO imprinted into the spectrum of that QSO. One QSO spectrum can be used to study the chemical composition of several absorption systems present in the light path, however, more than one QSO rarely probes a single galaxy, thus the total chemical composition of a galaxy is derived from a single measurement on a random point of the galaxy gas reservoir. Contrarily, our position within the Milky Way provides us with a unique vantage point from where it is possible to use the light from hundreds of QSOs to study the chemical composition of a single galaxy in a tomographic way. This tomographic view of the gas chemical composition in a single galaxy provides important insight into the distribution of these abundances in galaxies at earlier cosmic times. This tomographic approach has been used before to study high-velocity clouds in the Milky Way halo (Richter et al. 2017), to study galaxies in the local group like the Magellanic clouds (Konstantopoulou et al. 2024) and the Andromeda galaxy (Lehner et al. 2020).

The motivation is to use this interesting approach to study one CGM and try to answer questions, which are impossible to answer in galaxies beyond the Local Group.

$$\text{PP–I}\quad \left\{ \begin{array}{rcl} {}^1\mathrm{H} + {}^1\mathrm{H} & \longrightarrow & {}^2\mathrm{H} + \mathrm{e}^+ + \nu_\mathrm{e} \\ {}^2\mathrm{H} + {}^1\mathrm{H} & \longrightarrow & {}^3\mathrm{He} + \gamma \\ \Downarrow {}^3\mathrm{He} + {}^3\mathrm{He} & \longrightarrow & {}^4\mathrm{He} + {}^1\mathrm{H} + {}^1\mathrm{H} \\ & \text{–or–} & \end{array} \right.$$

$$\text{PP–II}\quad \left\{ \begin{array}{rcl} {}^3\mathrm{He} + {}^4\mathrm{He} & \longrightarrow & {}^7\mathrm{Be} + \gamma \\ \Downarrow {}^7\mathrm{Be} + \mathrm{e}^- & \longrightarrow & {}^7\mathrm{Li} + \nu_\mathrm{e}(+\gamma) \\ {}^7\mathrm{Li} + {}^1\mathrm{H} & \longrightarrow & {}^4\mathrm{He} + {}^4\mathrm{He} \\ & \text{–or–} & \end{array} \right.$$

$$\text{PP–III}\quad \left\{ \begin{array}{rcl} {}^7\mathrm{Be} + {}^1\mathrm{H} & \longrightarrow & {}^8\mathrm{B} + \gamma \\ {}^8\mathrm{B} & \longrightarrow & {}^8\mathrm{Be} + \mathrm{e}^+ + \nu_\mathrm{e} \\ {}^8\mathrm{Be} & \longrightarrow & {}^4\mathrm{He} + {}^4\mathrm{He} \end{array} \right.$$

Figure 1.1: Equation representation of the pp-chain types.

1.2 Metallicity in galaxies

Astronomers refer to elements heavier than H and He as *metals*. Metals originate inside the nuclei of stars. With increasing stellar mass the temperature and pressure in the core increase, this allows for different modes of nuclear fusion each yielding heavier elements. Elements as heavy as Fe can be fused in this process.

Stars with a mass of less than 1.5 $M_\odot$ during their life in the main sequence produce most of their energy with the proton-proton chain (*pp-chain*), this process comes in three flavors, *pp-I*, *pp-II*, and *pp-III*, they use different nuclei, but always yield ^{4}He in the end (Bethe 1939; Hansen et al. 2004). The different pp-chains are illustrated in Figure 1.1 and Figure 1.2, both Figures can be found in Hansen et al. (2004) Section 6.3.

In the nuclei of massive stars, the dominant process to generate energy during their time in the Main Sequence is the CNO-cycle, a process in which carbon, nitrogen, and oxygen (CNO) isotopes are consecutively capturing protons and β^+ decaying ending in a proton capture that yields a He nuclei. The reactions are shown in Figure 1.3 where each block is a type of CNO-cycle, and the *or* means that that particular reaction can either mark the end of the cycle or connect to the other chain. Figure 1.4 shows a CNO-cycle diagram from Gamow (1952).

After the main-sequence atomic nuclei start to fuse into metals via triple-α and He-burning. Triple-α takes place when the nuclei $T \lesssim 10^8$K and takes two ^{4}He to form ^{8}Be and another ^{4}He to form an stable ^{12}C, and subsequently absorb one more ^{4}He to form ^{16}O.

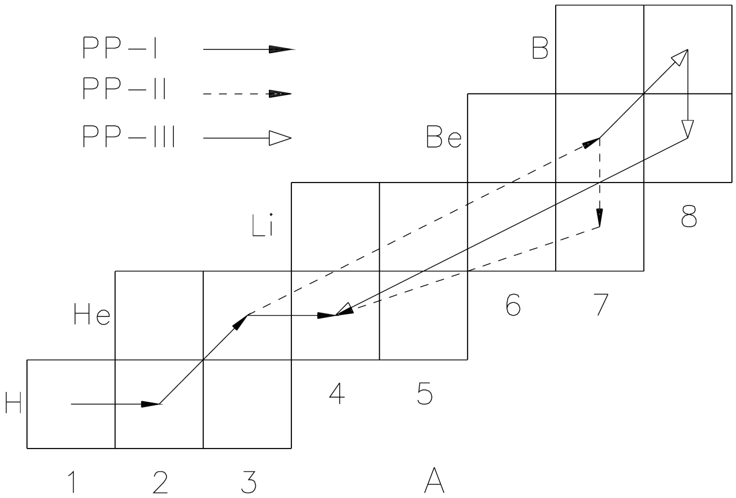

Figure 1.2: Graphical representation of the pp-chain types. Here the vertical axis represents the atomic number Z, and the horizontal axis the mass number A. Each arrow represents one type of pp-chain and the end product is ^{4}He.

$$
\begin{array}{rcl}
{}^{12}\mathrm{C} + {}^{1}\mathrm{H} & \longrightarrow & {}^{13}\mathrm{N} + \gamma \\
{}^{13}\mathrm{N} & \longrightarrow & {}^{13}\mathrm{C} + \mathrm{e}^{+} + \nu_{\mathrm{e}} \\
{}^{13}\mathrm{C} + {}^{1}\mathrm{H} & \longrightarrow & {}^{14}\mathrm{N} + \gamma \\
{}^{14}\mathrm{N} + {}^{1}\mathrm{H} & \longrightarrow & {}^{15}\mathrm{O} + \gamma \\
{}^{15}\mathrm{O} & \longrightarrow & {}^{15}\mathrm{N} + \mathrm{e}^{+} + \nu_{\mathrm{e}} \\
\Downarrow\ {}^{15}\mathrm{N} + {}^{1}\mathrm{H} & \longrightarrow & {}^{12}\mathrm{C} + {}^{4}\mathrm{He} \\
 & \text{–or–} & \\
{}^{15}\mathrm{N} + {}^{1}\mathrm{H} & \longrightarrow & {}^{16}\mathrm{O} + \gamma \\
{}^{16}\mathrm{O} + {}^{1}\mathrm{H} & \longrightarrow & {}^{17}\mathrm{F} + \gamma \\
{}^{17}\mathrm{F} & \longrightarrow & {}^{17}\mathrm{O} + \mathrm{e}^{+} + \nu_{\mathrm{e}} \\
\Downarrow\ {}^{17}\mathrm{O} + {}^{1}\mathrm{H} & \longrightarrow & {}^{14}\mathrm{N} + {}^{4}\mathrm{He} \\
 & \text{–or–} & \\
{}^{17}\mathrm{O} + {}^{1}\mathrm{H} & \longrightarrow & {}^{18}\mathrm{F} + \gamma \\
{}^{18}\mathrm{F} + \mathrm{e}^{-} & \longrightarrow & {}^{18}\mathrm{O} + \nu_{\mathrm{e}} \\
{}^{18}\mathrm{O} + {}^{1}\mathrm{H} & \longrightarrow & {}^{19}\mathrm{F} + \gamma \\
{}^{19}\mathrm{F} + {}^{1}\mathrm{H} & \longrightarrow & {}^{16}\mathrm{O} + {}^{4}\mathrm{He}
\end{array}
$$

Figure 1.3: Equation representation of the CNO-cycles, where each block represents a CNO-cycle, and the most commonly referred to as CNO-cycle is the connection between the first and second cycle. The end of a cycle is reached when the reaction yields the isotope of C, N, or O it started with plus a ^{4}He nuclei.

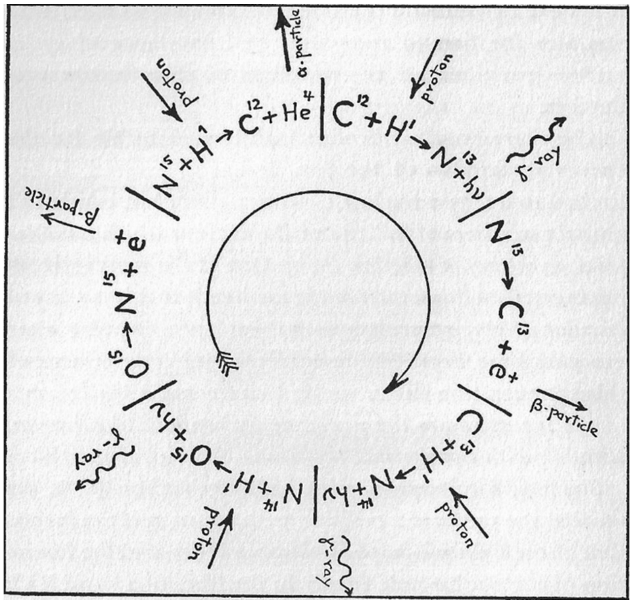

Figure 1.4: CNO-cycle diagram from Gamow (1952). The cycle begins with the ^{12}C at the top of the diagram, and ends in the reaction that yields back a ^{12}C and a α-particle (^{4}He).

He-capture, or α-capture is responsible for fusing nuclei starting from ^{16}O into ^{20}Ne, then through another α-capture, fuse into ^{24}Mg, and so on until the Iron-peak elements, around Ti, Fe or Ni. Elements created by He-capture are called *α-elements*. Examples of these elements are C, O, Ne, Mg, Si, S, Ca, and Ni. Carbon and oxygen are also created via triple-α, and Ti, Fe, and Ni are also called Iron-peak elements, thus these elements are not usually referred to as *α-elements*.

While metals are created during the star's life, they are *locked in* the nuclei and are rarely expelled from the star. However, some processes can bring metals to the star's surface and after a coronal flare, these metals may be released from the star. For example, dredge-ups occur to medium-mass stars in the red giant branch when the convection zone of the star extends into the surface, this brings metals from the core into the surface of the star (Mowlavï 1999).

After massive stars leave the main sequence and enter the He fusion phase, the He-flash can evacuate part of the star mass into the interstellar medium, thus enriching the medium around them. However, the main process that enriches the gas of a galaxy is supernovae (SNe) (Tinsley 1979; Binney and Tremaine 2008).

There are two main SN types: *thermonuclear* SN (SN Ia) and *cataclysmic* SN (SN II). SN II occurs at the end of the life of massive stars due to gravitational collapse when nuclear fusion stops generating energy. SN type II occurs quickly after the star formation event by no more than $\sim 40\,$Myr. On the other hand, SN Ia occurs after one component of a stellar binary system evolves into a compact object like a white dwarf and later accretes sufficient mass from the companion to start a runaway nuclear fusion reaction releasing enough energy to explode in an SN. SN type Ia needs a longer process to start, thus presenting a lag from 0.5 to 10 Gyr with respect to star formation (Binney and Tremaine 2008).

When an SN explodes it enriches the interstellar medium (ISM) with the metals that were once locked into the nuclei of the star, plus, depending on the initial condition of the SN, neutron capture elements, which are elements heavier than Fe, formed in environments with heavy isotopes and overdensities of neutrons.

SN type II yields mostly α-elements (C, O, Ne, Mg, Si, S, and Ca) and Fe-peak elements (Ti, V, Cr, Mn, Fe, Co, and Ni), while SN Ia yields mostly Fe-peak elements.

This makes it so that the ratio between the number of α-elements and Fe-peak elements ($[\alpha/\mathrm{Fe}]$) is sensitive to the ratio between the number of SN II and the number of SN Ia that have happened in a galaxy, and since SN events are related to star formation events, studying $[\alpha/\mathrm{Fe}]$ delivers information about the star formation history (SFH) of a galaxy. Further discussion about this is found in section 4.3 and section 5.2.

1.2.1 The Circumgalactic Medium at high redshift

The replenishment of gas from the IGM into a galaxy is necessary to explain the star formation (SF) rate measured in galaxies at all redshift, which is large enough to consume all resources within a few Gyrs (Fox and Davé 2017). The CGM is the gas that surrounds a galaxy typically within a virial radius (R_{vir}) and the ISM, while outflows of gas can reach further than this limit they are also considered part of the CGM. The CGM is of the utmost importance because it mediates interactions between galaxies and the larger-scale IGM. The CGM is multi-phased and the total gas mass and, metal mass can exceed their corresponding masses inside the galaxy (Tumlinson et al. 2017). Galactic-scale winds driven by AGN or by SN control star formation by expelling metal-enriched gas into the CGM, where it can cool down and be cycled back into the ISM or if it has enough energy it can flow out into the IGM.

A schematic view of the CGM is shown in Figure 1.5, it shows the dynamic and rich constitution of the CGM and how important it is to study it in a large range of scales.

The physical properties of the CGM depend on competing gravitational gas infall and gas-cooling, whether the free fall time is faster or slower with respect to cooling will determine if the gas is hot (roughly virial temperature) or cold ($T \sim 10^4$ K) respectively (Faucher-Giguère and Oh 2023).

Cold gas is the main observational probe of the CGM because it is observed in absorption with high resolution by QSO sightline spectroscopy and in emission by integral field units (IFU) on large ground-based telescopes in Keck or VLT (Faucher-Giguère and Oh 2023). On the other hand, hot gas direct observations come far and between, except for X-ray observations on the most hot environments, like galaxy clusters, groups, or massive elliptical galaxies. In this work, I will focus on the cold gas that can be seen in absorption.

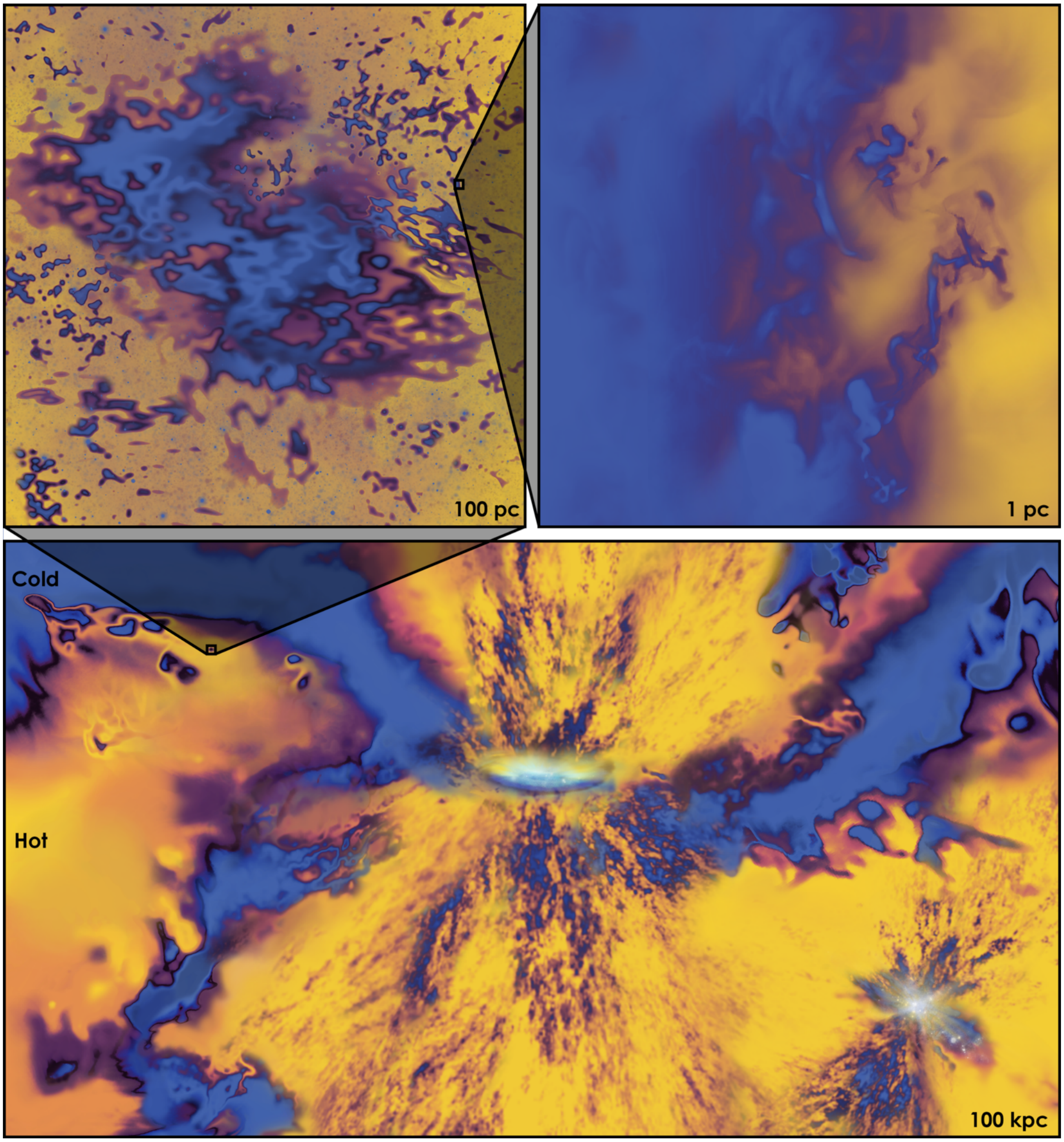

Figure 1.5: Figure 1 from Faucher-Giguère and Oh (2023) showing the complex multiple phases with dynamics ranging from 100 kpc to as small as sub-parsec scales. The bottom panel shows a central galaxy whose star formation is fueled by a mix of cold (blue) and hot (yellow) accreting gas, which powers a multi-phase galactic wind. The top two panels zoom onto a highly structured cloud complex (left) and a turbulent mixing layer (right). Figure credit: Aaron M. Geller (Northwestern University/CIERA/IT Research Computing Services). ©2022 Aaron M. Geller

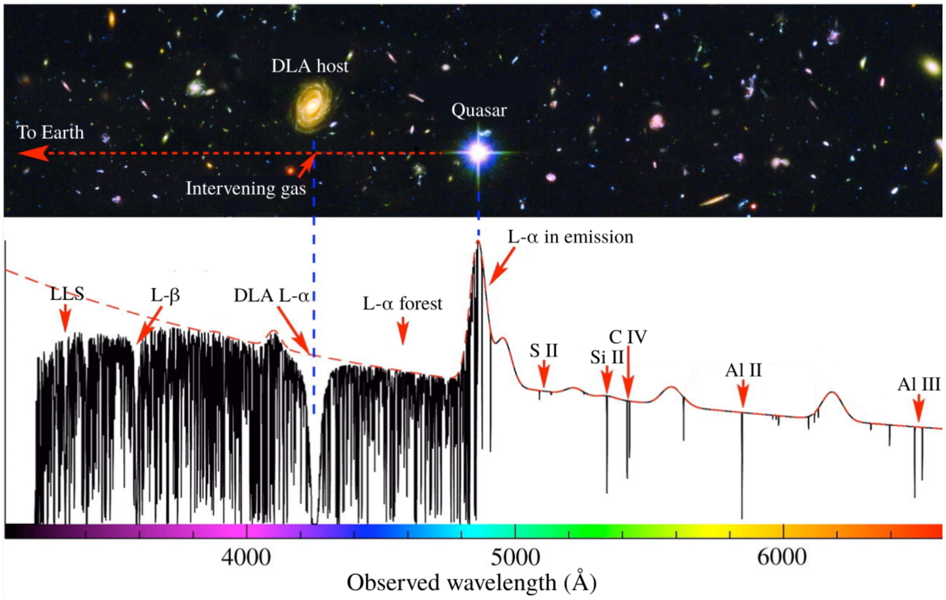

Figure 1.6: Representation of a QSO spectrum where the different absorption system classes can be seen. The metal lines marked are associated with the DLA because they are at the same redshift. The Lyman-α forest is associated with the pristine gas from the IGM, thus they present a *forest* of narrow lines starting from the Lyman-α of the QSO.

1.2.2 Damped Lyman Alpha systems

To classify absorption systems seen in QSO spectroscopy astronomers classify them by their H I column density. In increasing H I column density there are: Lyman-α forest, Lyman Limit systems, which have N(H I)$< 10^{19}$cm^{-2}; sub-Damped Lyman alpha systems (sub-DLAs), with 10^{19}cm^{-2} $<$ N(H I) $< 2 \times 10^{20}$cm^{-2}; and finally Damped Lyman systems (DLAs) that have N(H I) $> 2 \times 10^{20}$cm^{-2}. Figure 1.6 shows an example of absorption systems, where the most prominent absorption feature is a DLA and its associated metal lines. An example of the absorption profile of a DLA is shown in Figure 1.7.

The most common systems are the ones with the lowest N(H I), and DLAs and sub-DLAs are the least abundant systems. This can be seen in Figure 1.8, from Noterdaeme et al. (2009), which shows the frequency of encountering a system given its N(H I), where the most common systems are the ones with the lowest

Despite being less frequent than any other absorption system 20% of the total mass density of H I in the Universe is contained in sub-DLAs, and a larger portion of the total is associated with DLAs (Noterdaeme et al. 2009; Prochaska and Wolfe 2009a). Figure 1.9, from Noterdaeme et al. (2009) shows the cumulative total density of N(H I), and it is clear to see that the most dense systems dominate the H I cosmic budget.

Indeed, DLAs are distinctive because at log(N(H I)) > 20.3 the Lyman-α absorption shows large damping wings, as can be seen in Figure 1.7. At such high N(H I) the absorption system becomes self-shielded from ionization, therefore abundances for chemical elements are mostly on their neutral phase (Wolfe et al. 2005), thus effectively for the chemical element present in the DLA the dominant ionization states is such that the ionization potential is greater than

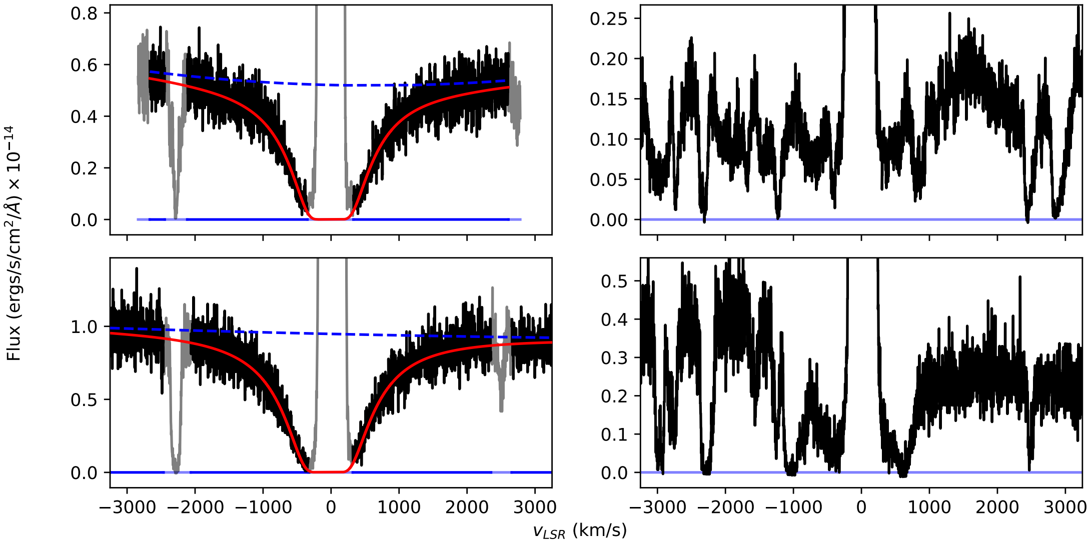

Figure 1.7: Example of a DLA-like absorption. The solid black line is the absorption profile, the red line is the Voigt profile fitted that characterizes the absorption and the dashed blue line shows the continuum. The most stand-out feature in DLA profiles is the damping wings seen at $|v| > 500$ km/s. Velocity is measured with respect to $z = 0$

H I (13.598 eV). For example for O and N the dominant ionization state is O I and N I, and for C and S the dominant ionization state is once ionized C II and S II. A table compiling the ionization potential of elements can be found on Lide (2008).

As DLAs contribute the majority of the neutral gas in the Universe they arise as important tracers for metallicity evolution. The metallicity evolution of DLAs across cosmic time has been studied thoroughly. Rafelski et al. (2012), Rafelski et al. (2014), and Berg et al. (2016) study the metallicity evolution of DLAs and find a consistent trend of increasing metallicity at lower redshift as can be seen in Figure 1.10.

One important feature of the metallicity enrichment history is the large scatter found at every redshift studied which cannot be explained by the uncertainty in the measurements. This large scatter in the metallicity evolution is then explained physically by different origins such as differences in stellar mass on the DLA host leading to differences in metallicities at the same redshift (Baker and Maiolino 2023), or even differences in metallicity within the same galaxy can affect the measured metallicity depending on the path the QSO sightline takes through the CGM or ISM in the host galaxy (Péroux et al. 2020).

Most DLAs nowadays are only observed in absorption and are not associated with any galaxy in emission, especially at $z > 1$ (Kulkarni et al. 2022). DLA hosts are often referred to as a *mixed bag* of galaxies for this reason, and the dominant galaxy type associated with DLAs is still under debate (Wolfe et al. 1986; Rao et al. 2003; Cooke et al. 2015; Kulkarni et al. 2022).

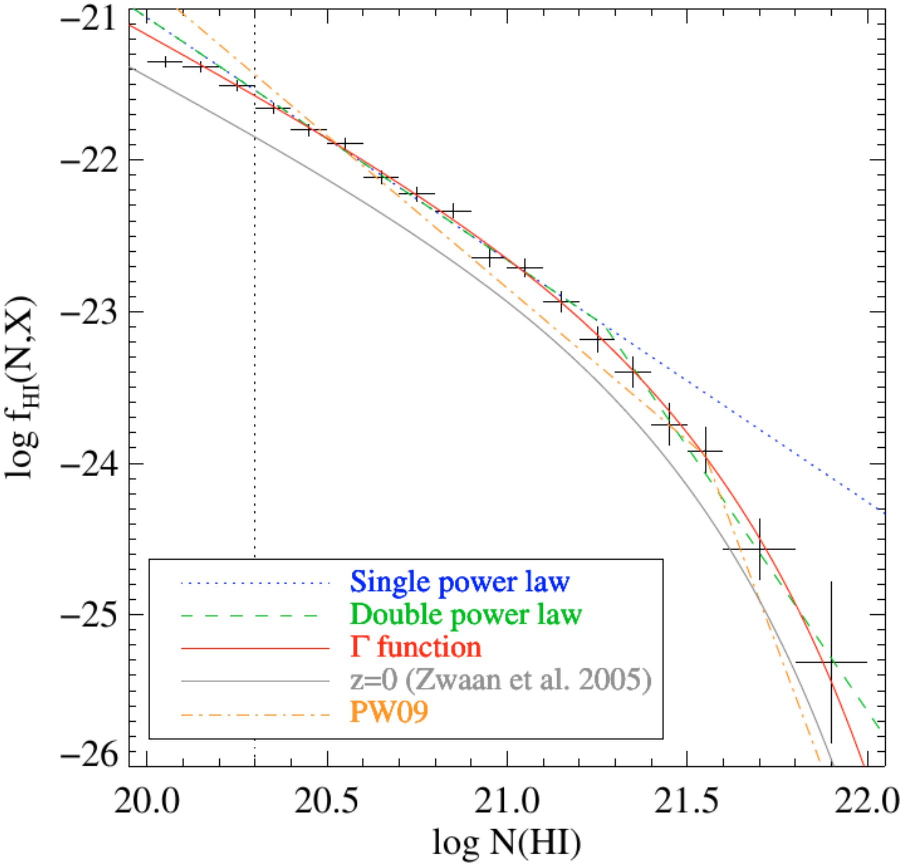

Figure 1.8: Figure and caption from Figure 11 in Noterdaeme et al. (2007). N(H I) frequency distribution of DLA systems in SDSS-DR7 from their automatic procedure. Fits to the observations by a single power law, a double power law and a gamma function are given as, respectively, a dotted blue, dashed green and solid red line. The double-power law fit to the Prochaska and Wolfe (2009a) sample is indicated by the dashed orange line. The Γ-function fit to the frequency distribution obtained by Zwaan et al. (2005) from 21-cm observations at $z = 0$ is also indicated as a solid grey line for direct comparison.

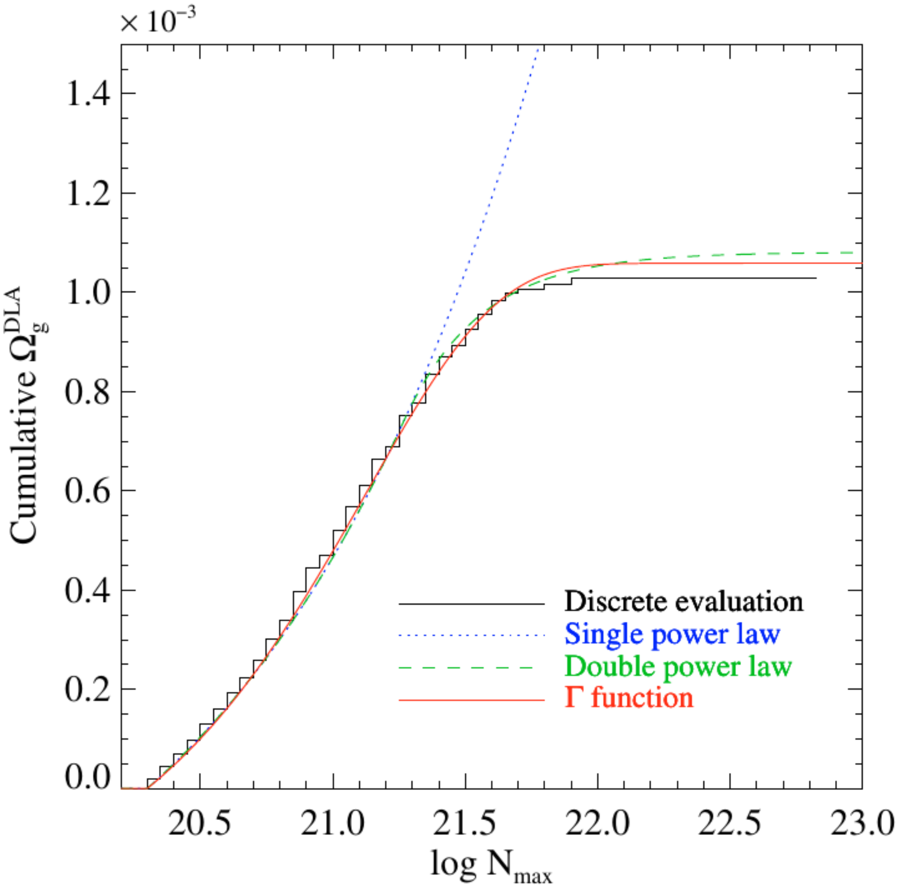

Figure 1.9: Figure and caption from Figure 13 in Noterdaeme et al. (2007). Cumulative cosmological mass density of neutral gas in DLAs as a function of maximum column density. This figure highlights the importance of DLAs to the total budget of H I in the Universe. The apparent flattening of the curve at log N(H I) ~ 21.7 implies convergence.

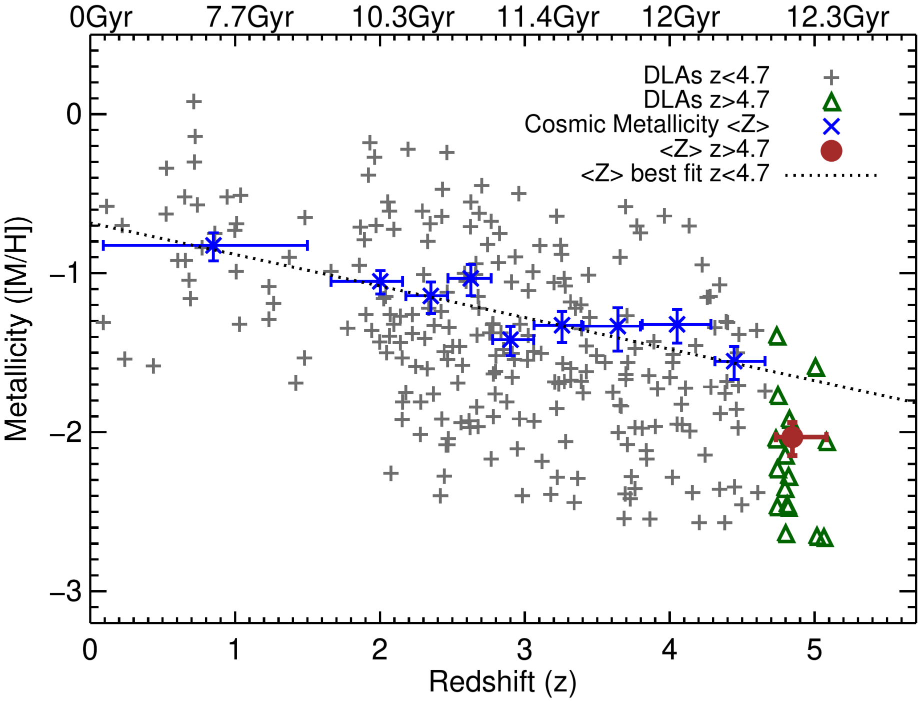

Figure 1.10: Figure and caption from Figure 3 in Rafelski et al. (2014). DLA metallicity versus redshift, showing a sharp decrease in metallicity at $z > 4.7$. The gray plus signs are metallicities of DLAs at $z < 4.7$, and the green triangles are DLAs at $z > 4.7$. The blue crosses show the cosmic metallicity, $\langle Z \rangle$, with the vertical error bars representing 1σ confidence levels from our bootstrap analysis. The black dotted line is a linear fit to the $\langle Z \rangle$ data points in redshift space for DLAs $z < 4.7$. The brown circle is $\langle Z \rangle$ deduced from DLAs at $z > 4.7$ and is significantly below the linear fit.

1.3 Metals in the Milky Way

Stars in our galaxy are usually so bright they can be studied individually and metallicities can be obtained one by one modelling their atmosphere using models such as local thermodynamic equilibrium (LTE) (Reddy et al. 2003; Reddy et al. 2006; Frebel 2010). These metallicities measured in the atmosphere of stars reflect the metal content of the gas they are made of, thus, in combination with age estimates, they are useful to study the enrichment history of a galaxy.

The metallicity or metal content in the Milky Way's gas can be measured directly using emission line ratios from star-forming regions in molecular hydrogen (H II) clouds (Arellano-Córdova et al. 2020; Arellano-Córdova et al. 2021); in the atmosphere of stars, using spectroscopic observations, and different models for the atmosphere of these stars it is possible to retrieve accurate. This is not possible in the case of other galaxies, except for galaxies in the Local Group, like the Magellanic Clouds and Andromeda galaxy, because of the difficulty of resolving individual stars with spectrographs.

In this thesis, however, the focus is on the cold neutral gas that can be studied with quasar sightline spectroscopy. Studying the Milky Way's (MW) gas in this way has the advantage that the light from any visible QSO must have gone through the MW's ISM and CGM to reach Earth.

QSO sightline spectroscopy allows astronomers to study the present-day chemical abundances in the cold gas reservoirs of galaxies in the direction of the QSO, and in cases where N(H I)$> 2 \times 10^{20}$ the gas is neutral in that sightline and the MW can be studied the same way a DLA is.

1.4 This thesis

In this thesis, I study metallicity variations in the neutral gas reservoirs of the Milky Way. I discuss these variations in metallicity and [α/Fe] in the context of the MW's gas to see if it is comparable to similar studies that use different methods. I discuss the use of metallicity variations in the neutral gas reservoirs of one evolved galaxy to explain the same variations seen on high redshift DLAs.

Thus, the goals of this thesis are to address the following questions:

- What is the metal content of the MW's neutral gas?
- Is it possible to find the distribution of metals by using quasar sightline spectroscopy?
- What can the metallicity variations in the MW tell us about the cosmic metallicity evolution of DLAs?

The rest of this thesis is organized as follows: chapter 2 describes the sample of QSO spectra used; biases, and their possible consequences are discussed as well. In chapter 3 the method followed to fit voigt profiles to the spectra in the sample, the calculation of the column density is described and the limitations of the modeling are discussed. Chapter 4 discusses the variations in the metallicities and [α/Fe] measured in the previous chapter, in the context of the Milky Way. Chapter 5 discusses the same variations in chemical abundances in the context of the cosmic chemical evolution of DLAs. Finally, chapter 6 summarizes and discusses the results. Additionally, chapter 7 describes ways of moving forward with this work in the future.

Chapter 2

Data

In this chapter, I characterize the QSO spectra sample used. I used publicly available QSO spectra in rest-frame UV observed by the Cosmic Origin Spectrograph (COS) aboard the Hubble Space Telescope (*HST*) from the COS-Galactic Absorption Lines (COS-GAL) archive (Zheng et al. 2019). The resolving power $R = 12.000 - 20.000$ enables fitting Voigt profiles, measuring column densities, and therefore estimating chemical abundances of several important metal lines, and the Lyman-α absorption.

In addition, in this chapter, I also asses the biases in the sample selection because of possible dust reddening of the QSO, and how the contamination of high redshift absorbing systems can affect the column densities measured.

2.1 Sample selection

The Milky Way is seen in absorption at $z \sim 0$ and rest-frame, furthermore, most element transitions lie in the near and far-UV; hence, UV spectroscopy is essential to study chemical abundances of several key elements that have different ionization levels and nucleosynthetic origin in the gas phase of galaxies. However, the UV range is absorbed by the Earth's atmosphere, making it necessary to use space-based telescopes.

In this thesis data obtained with the *Cosmic Origin Spectrograph* (COS) are used. The COS is a UV spectrograph aboard *Hubble Space Telescope* (HST) that across the years has accumulated a large amount of now publicly available data. The Hubble Spectroscopic Legacy Archive (HSLA Peeples et al. 2017) provides combined spectra of publicly available data from COS, data from different epochs, grating, observing programs of the same target are co-added to increase the S/N and the wavelength coverage. The COS-GAL (Zheng et al. 2019) archive is a compilation of 401 QSO spectra with S/N > 5 from the HSLA reduced with the goal of studying the absorption lines of the MW. Spectra in the COS-GAL archive have been continuum-fitted with *Linetools* (Prochaska et al. 2016), however, those authors do recommend users to be on the lookout for intervening absorption of higher z systems as they did not run a detailed analysis into the presence of higher redshifts interlopers. For this

ID	Glon	Glat	S/N	z	ID	Glon	Glat	S/N	z
	(°)	(°)				(°)	(°)		
J141949.39+060654.0	351.9189	60.2851	6.8	1.648	SBS1122+594	141.8033	54.7097	11.9	0.851
PG-1630+377	60.3421	42.9393	36.8	1.478	SDSSJ101622.60+470643.3	169.0288	53.7423	6.7	0.822
HB89-0232-042	174.4627	-56.1555	17.5	1.437	VV2006-J222836.3-095009	53.2369	-52.1801	8.7	0.797
PG-1522+101	14.8922	50.1217	22.6	1.328	SDSS-J141038.39+230447.1	24.5712	71.6404	10.3	0.795
LBQS-1435-0134	348.7184	51.3746	31.1	1.31	SDSSJ234500.43-005936.0	88.7929	-59.3884	6.4	0.79
SDSS-J135726.27+043541.4	340.7675	62.5141	10.0	1.234	SDSSJ102218.99+013218.8	242.16	46.0656	6.7	0.79
HE0435-5304	261.0247	-41.3746	11.5	1.231	SDSSJ100102.55+594414.3	152.5697	46.3865	10.8	0.747
PG-1338+416	90.587	72.4837	16.6	1.217	VV2006-J125901.7+413055	117.238	75.5287	9.6	0.745
PG-1206+459	144.6291	69.6209	22.8	1.164	SDSSJ091440.38+282330.6	198.1323	42.4466	7.4	0.735
FIRST-J020930.7-043826	165.9922	-60.8074	10.4	1.128	SDSSJ155304.92+354828.6	57.2591	50.6668	7.2	0.722
SDSS-J100535.24+013445.7	238.5271	42.7859	10.5	1.08	SDSSJ155504.39+362848.0	58.3163	50.2662	5.7	0.714
VV2006-J092542.3+344108	189.9464	45.7029	7.6	1.067	SDSSJ124511.25+335610.1	133.7244	83.0607	5.8	0.711
HE0439-5254	260.6931	-40.9014	16.9	1.053	SDSSJ113457.62+255527.9	212.6185	72.8679	6.9	0.709
LBQS-0107-0235	134.0062	-64.7985	10.8	0.957	SDSSJ144511.28+342825.4	56.7398	64.5904	5.9	0.697
HB89-0107-025-NED05	134.0292	-64.7794	11.4	0.956	PKS0552-640	273.4656	-30.6114	29.7	0.68
PG-1407+265	34.6687	72.5886	38.8	0.94	3C57	173.0773	-67.2617	24.3	0.67
SDSSJ112244.89+575543.0	143.6452	55.4883	6.2	0.906	SDSSJ105958.82+251708.8	210.811	64.9832	7.9	0.662
SDSSJ141910.20+420746.9	78.5766	66.6566	5.7	0.874	SDSSJ080908.13+461925.6	173.3223	32.2889	11.6	0.658
VV2006-J095243.0+515121	163.927	48.5444	9.1	0.862	PKS0637-752	286.3684	-27.1584	24.8	0.653
Q2251+155	86.111	-38.1839	5.4	0.859	3C263	134.1592	49.744	37.4	0.646

Table 2.1: The 20 QSO with highest z_{QSO}. Columns from left to right are: ID name as they appear in HSLA first data release (Peeples et al. 2017), Galactic Longitude in degrees, Galactic latitude in degrees, S/N ratio as reported in HSLA first data release.

reason section 3.2.1 describes the process to find possible interlopers, and more details on the reduction process are available on (Zheng et al. 2019).

The sample of QSO spectra used in this work was retrieved from COS-GAL with a Python script shared with me by Trystyn Berg in private communication. I downloaded every spectra from the COS-GAL archive that had coverage of both G130M and G160M gratings, in order to have access to H I, low ionization ions, and the high ions C IV and Si IV. From these spectra those that present higher-redshift Lyman Limit Systems (LLS) whose higher-order Lyman-α lines are blended with the MW Lyman-α were discarded from the sample because the column density of H I is important to later measure metallicity-more details into this can be seen on Section 3.3 and the Lymanα for these sightlines is available in Annex D.

In the COS-GAL archive, there were 223 QSO spectra observed with both G130M and G160M gratings, from which 14 spectra were discarded because the Lyman-α of the MW was completely covered by the geocoronal Lyman-α emission, or was obscured by Lyman limit absorption from higher z systems, and did not allow for the measurement of H I column density [1]. Using these criteria the sample is composed of 209 QSO spectra, their position on the sky and S/N can be seen in Figure 2.1. A table characterizing 20 spectra from the used sample is shown in Table 2.1, and the full table can be found in Annex G.

Each spectrum in the COS-GAL archive has a resolving power $R = 12.000 - 16.000$ for the G130M grating, and $R = 13.000 - 20.000$ for the G160M. Figure 2.3 shows a representation of every spectrum in the COS-GAL archive that has coverage to both G130M and G160M grating and the wavelength of the absorption lines at z_{MW} that were analyzed later on Chapter 3. A representative spectrum in terms of S/N can be found in Figure 2.2.

---

[1] For these 14 systems the unobscured metal lines were fitted for completion, but these results were not taken into account for the later analysis

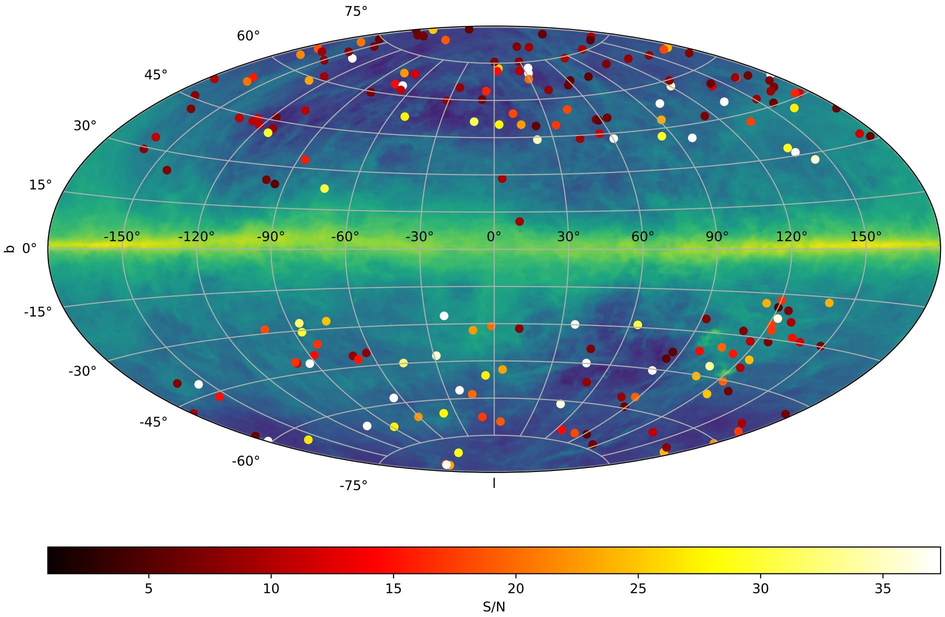

Figure 2.1: Present sample of 209 COS spectra in galactic coordinates in Hammer-Aitoff projection, symbol color represents S/N as measured in ~ 1300(Å). The background is a 21-cm emission map of the Milky Way from (HI4PI Collaboration et al. 2016).

Spectra in this sample are characterized by MW absorption lines, but also by intervening systems outside the MW at wildly different z plus the absorption and emission of the MW at $z \sim 0$. The representation of the spectra in Figure 2.3 shows absorption lines as red spots and emission lines with white, while black regions show regions with no coverage. The narrow vertical red lines are absorption lines of the Milky Way at $z \sim 0$, the narrow vertical white line at 1215 Å is the geocoronal H I emission, and the one at 1302 Å is the airglow line of O I. This figure also shows that the spectra taken from QSO at higher z – shown higher in the plot – present more absorption lines of absorption systems at high redshift, some of these are metal lines, but most of them are just absorption from the Lyman-α forest, which also explains why at the lower right part of the figure there are fewer absorption lines other than the MW's.

2.2 Sample Biases

The sight lines in this sample lie mostly above the galactic plane – 90% of sightlines are at $|b| > 30\,\mathrm{deg}$ – this is because most of the QSO are selected for observations using an optical color criteria and the presence of dust in the MW, or the QSO host, or in a foreground absorber can lead to a reddening effect in the optical, which introduces a bias to preferentially observe unreddened QSO (Pontzen and Pettini 2009; Krogager et al. 2015; Krogager et al. 2023). Observing QSOs through the MW's disk would allow us to see sightlines with much

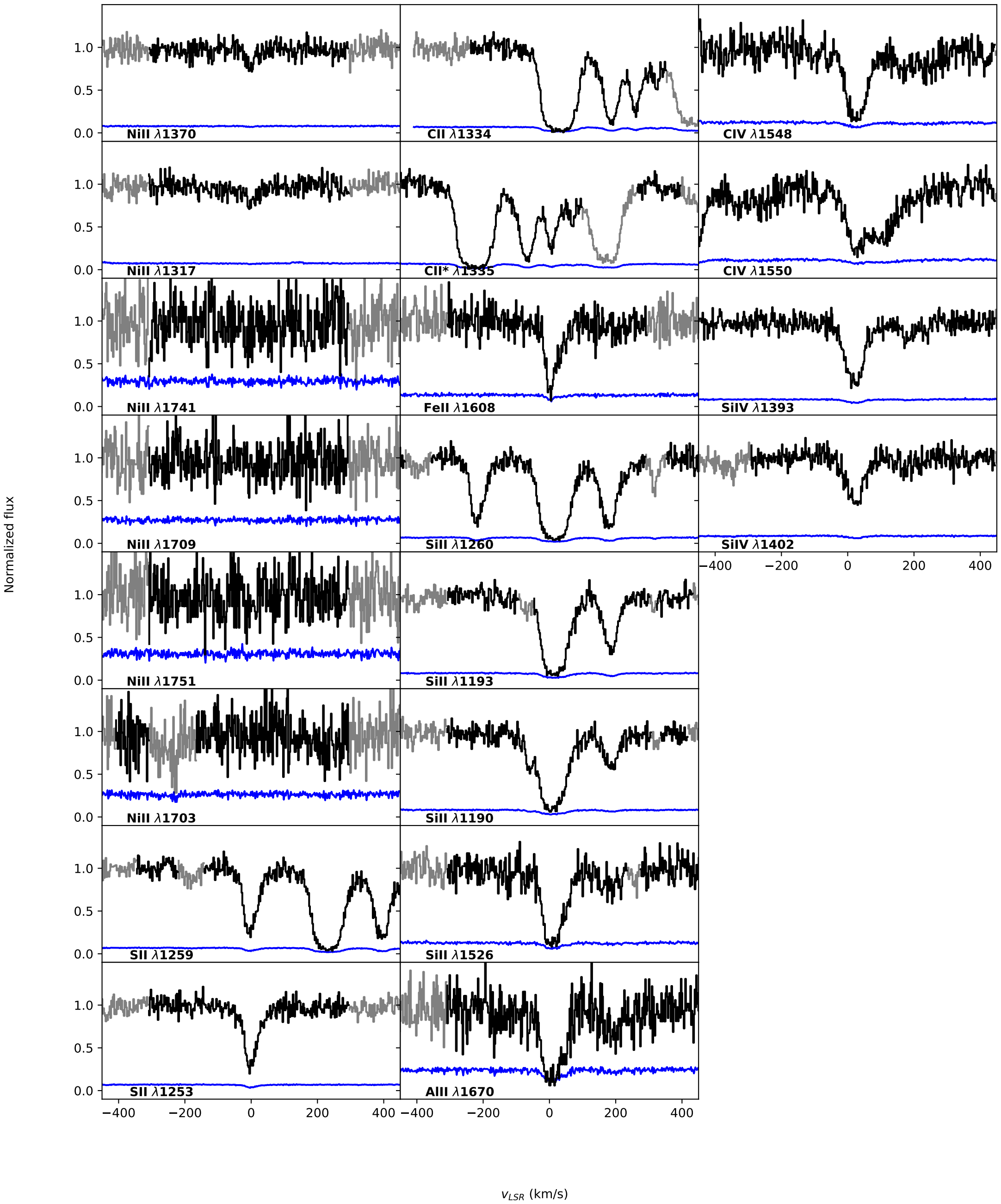

Figure 2.2: Example spectra of one of the lines of sight with a representative signal-to-noise ratio of S/N $\sim$ 38, *rxs-j23218-7026* as called in the HSLA data release. Each panel shows the velocity region used to fit the metal lines at $z = 0$. In black is the normalized flux, in grey is the flux not used for fitting, and in blue is the 1-σ error array.

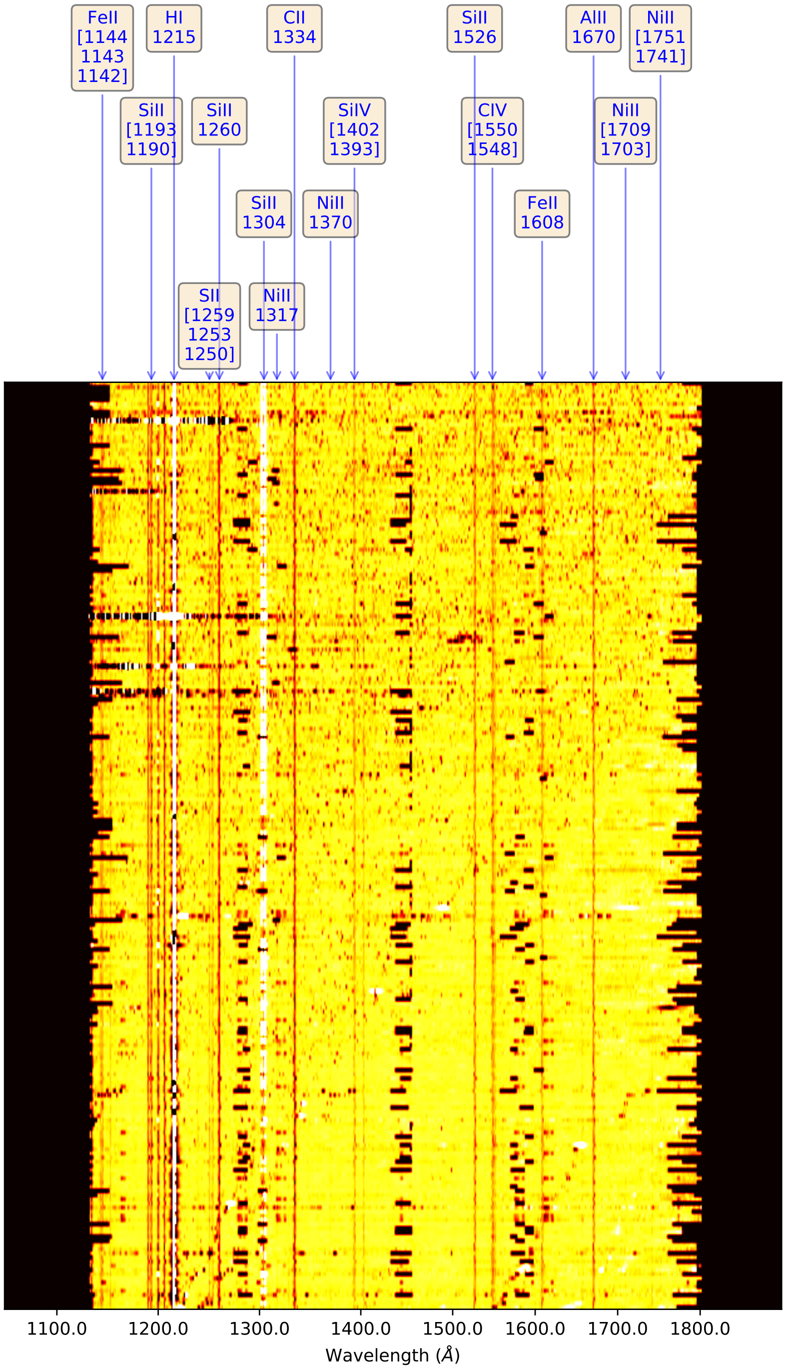

Figure 2.3: Every spectra in the COS-GAL archive with coverage using both G130M and G160M gratings. The horizontal axis is the spectral axis, and in the vertical axis is every sightline ordered from top to bottom by decreasing z_{QSO}. White regions are emission lines, and black regions are regions with no coverage, and red spots are absorption lines. The boxes on the upper part of the Figure have the name of ion transitions fitted in this work, and the blue arrow points towards the wavelength of these lines. For clarity lines of the same ion close to each other occupy the same box.

more dust because this component of the Galaxy is more dense than the Halo. The ISM is the component of the galaxy where star formation happens, so this is the place where it is expected to find the most metals and these metals to condense back into dust. As there are few observations of QSOs across the MW disk, the metallicity measured here may be underestimating the metallicity of the MW.

Higher redshift quasars show more contamination from absorption systems at higher redshift, these extra lines make it more likely that MW lines are blended. This effect can be seen in Figure 2.3 where the spectra on the upper part have more dark regions compared to the spectra at the lower part of the Figure.

To avoid contamination from absorption systems at higher redshift I thoroughly looked for every absorption system in the spectra, by looking for the Lymanα of these systems between the Lymanα of the QSO and the Lymanα of the MW, the method used is explained in detail in Section 3.2.1. But if $z_{QSO} > 0.561$ then the Lymanα of the QSO is outside the wavelength range of COS, and therefore it is possible for intervening systems to have their Lymanα outside the wavelength range too, making them harder to find, hence for these sightlines it is possible that some absorption systems are unaccounted for.

Figure 2.4 shows a histogram of the redshift distribution of the QSOs in this sample, the red dashed line marks $z = 0.561$, the limit below which I am confident about having found all the intervening systems.

I am confident to have found every absorption system present in the spectra of quasars with $z_{QSO} < 0.561$. For 23% of the $z_{QSO} > 0.561$ population, blending by higher redshift systems does not affect the present results. This is because, for the Voigt profile fitting process, multiple lines were used for many of the species, and since these lines have known f-value ratios it is possible to identify blending of intervening systems. However some species show just one transition in COS wavelength coverage and if they are blended it would be difficult to distinguish possible blends, for this reason, these elements are not used for the following analysis but fitted anyway for the sake of completion.

Using voigt profile fitting to measure column density in saturated lines can be inaccurate, and just saturated lines can appear unsaturated on a first glance. This phenomena is called hidden saturation and it will be discussed in section 3.4.2.

2.3 Note on velocity plots

In this thesis, spectra are mostly plotted using velocity as the independent variable because it is more meaningful for the later analysis of the velocity structure. This is because velocity components in a velocity profile share the same z and here they are easier to spot. The transformation from wavelength λ to velocity v used here is

$$\frac{\Delta v_l}{c} = \frac{\Delta\lambda}{\lambda_0} \qquad\qquad v = \frac{\lambda - \lambda_l}{\lambda_l} \times c + v_0 \tag{2.1}$$

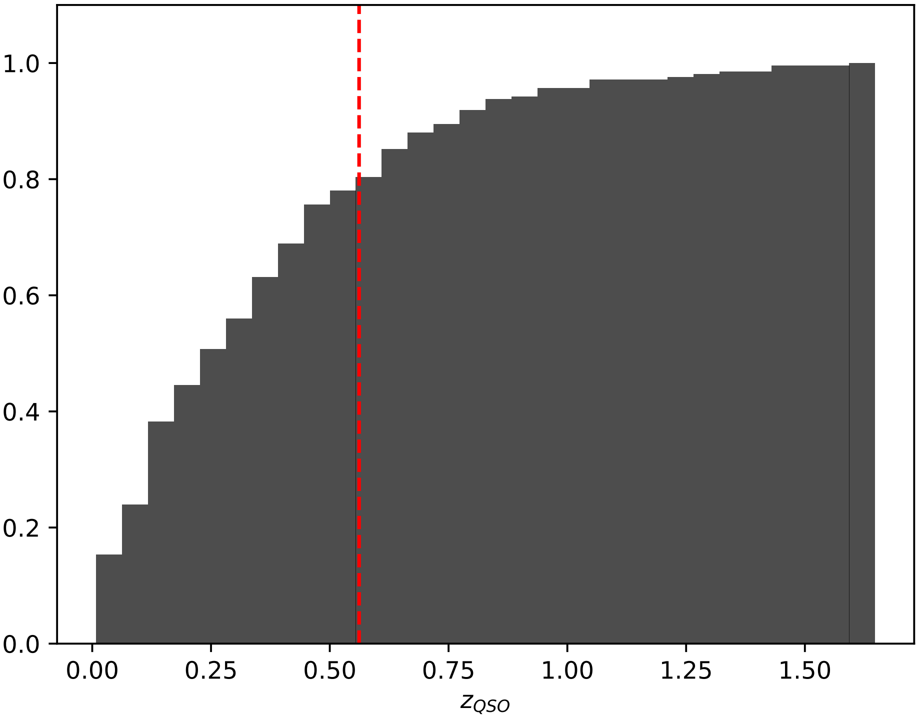

Figure 2.4: Cumulative histogram of the z_{QSO} in this sample. Red dashed line marks $z = 0.561$, maximum z at which the QSO's Lymanα is covered by the COS G130M and G160M grating. Spectra of QSOs at larger redshift may exhibit contain more intervening systems at high redshift.

where λ_0 is the rest-frame wavelength of transition l c is the speed of light, and v_0 is an arbitrary velocity offset that depends on the frame of reference used.

The velocity offset is not relevant to the measurement of column density but is necessary for display reasons. I decided to use the Local Standard of Rest (LSR) as the frame of reference. The LSR is the frame of reference that follows a circular motion around the galactic center that passes the position of the sun today and has a circular velocity equal to the mean circular velocity of the stars in the solar neighborhood (Bland-Hawthorn and Gerhard 2016). In the LSR frame of reference, the directions are for a coordinate system based at the Sun, where the i unit vector points towards the Galactic Centre, j in the direction of rotation, and k is upwards from the disk, $v_\odot = U_\odot i + V_\odot j + W_\odot k$.

The peculiar motion of the sun with respect to the LSR used here is $(U_\odot, V_\odot, W_\odot) \sim (9, 12, 7)$ km/s from Delhaye (1965), which was later revised by Bland-Hawthorn and Gerhard (2016). This velocity vector in galactic coordinates has a magnitude of 16.5 km/s in the directions $b_\odot = +25°$ and $l_\odot = 53°$.

To use the LSR as the frame of reference for a particular QSO sightline, the velocity offset was calculated using the dot product of the peculiar velocity in the direction of the QSO sightline. In galactic coordinates, this is calculated using the law of cosine in spherical coordinates

$$v_0 = v_\odot \times [cos(b_\odot)cos(b_{QSO})(cos(l_\odot - l_{QSO})) + sin(b_\odot)sin(b_{QSO})] \tag{2.2}$$

where v_0 is calculated for each QSO with it's angular coordinates (b_{QSO}, l_{QSO}).

Chapter 3

Voigt profile fitting

The spectral resolving power of COS enables a component-by-component analysis, with a precise measurement of column density and Doppler parameters, as long as the components are not saturated. In this chapter, I describe the Voigt profile fitting process of features at $z = 0$ in the spectral sample presented in the previous chapter, and the physical interpretation of the results of the fits.

3.1 Why Voigt profile fitting

To extract the column densities from an absorption profile there are three main methods:

1. Equivalent width measurements (Draine 2011, see Figure 3.1, Equation 3.1) where the measured *missing power* is directly translated to column density using the curve of growth (COG; Figure 3.2), this method is useful even when the resolving power is low and the lines are unresolved. Equivalent width (EW) and the conversion to column density when the line is not saturated is defined as

$$EW = \int \left(1 - \frac{I_0(\lambda)}{I(\lambda)}\right) \frac{d\lambda}{\lambda_0} = \int \left(1 - \frac{I_0(v)}{I(v)}\right) \frac{dv}{c} \tag{3.1}$$

$$N_l = 1.130 \times 10^{12} \mathrm{cm}^{-1} \frac{EW}{f\lambda_0} \qquad \text{if } \tau_{max} \ll 1 \tag{3.2}$$

   where I_0 is the continuum flux, I is the observed flux, λ_0 is the central wavelength of the transition in (cm), c is the speed of light, and f is the oscillator strength of the transition. This method is the fastest at the same time it is subject to blending issues. Without enough resolving power it is impossible to measure the Doppler parameter b and the formula used to calculate column density from EW in saturated lines is very sensitive to b. This formula is:

$$N_l = 46.29 \left(\frac{b}{f\lambda_0}\right) \exp\left[\left(\frac{cEW}{2b}\right)^2\right] \mathrm{cm}^{-2}\mathrm{s} \qquad \text{if } 10 \lesssim \tau_{max} \lesssim \tau_{\mathrm{damp}} \tag{3.3}$$

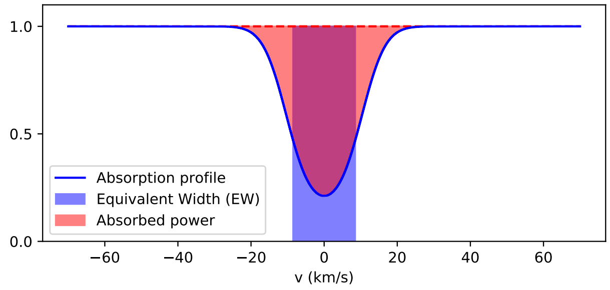

Figure 3.1: Equivalent width and missing power demonstration. The blue line is a normalized absorption profile and the red and blue areas are the same. The red area corresponds to the integral in Formula 3.1, while the blue area corresponds to a rectangle with $height = 1$ and $base = EW$, hence the blue area corresponds to $EW \times 1$.

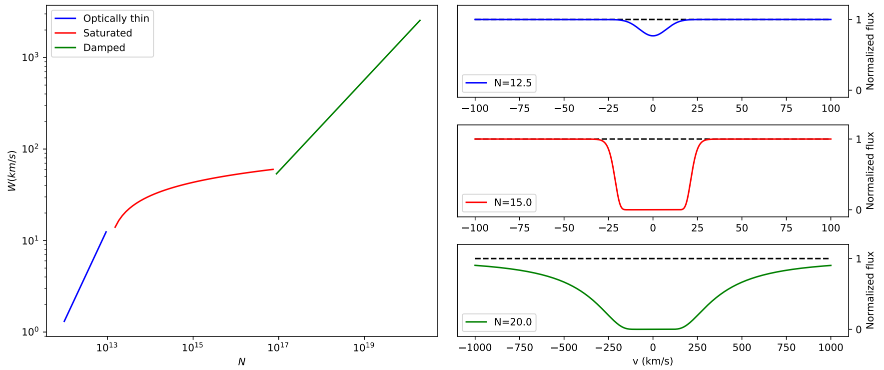

Figure 3.2: (Left) The curve of growth and the different regimes (Right) an example absorption belonging to each regime. Blue the line is optically thin, red is a saturated line, and green is a damped line. This COG was modelled from the Lyman-α transition using $b = 10\,\mathrm{km/s}$.

.

2. Apparent Optical Depth Method (AODM) (Savage and Sembach 1991) which converts the observed absorption line profile to apparent optical depth ($\tau_a(v)$) to apparent column density per unit velocity ($N_a(v)$). The total apparent column density is obtained by integrating the $N_a(v)$ profile over the velocity limits of the absorption profile.

$$N_a = \int N_a(v)dv = \frac{m_e c}{\pi e^2 f\lambda}\int \tau_a(v)dv = \frac{m_e c}{\pi e^2 f\lambda}\int ln\left(\frac{I_0(v)}{I(v)}\right)dv \tag{3.4}$$

When multiple transitions of the same ion are available with different $f\lambda$ values, each $N_a(v)$ profile should agree with each other. Any saturation or blend in one of the lines can be identified by analyzing the differences in the $N_a(v)$ profiles, so long there is at least one unsaturated profile. When the $N_a(v)$ profiles agree with each other then $N = N_a$, otherwise N_a is underestimating the total column density.

3. Voigt profile fitting (VPF), a Voigt profile is a function that uses physical properties of the absorbing gas −namely column density, oscillator strength, thermal and turbulent

broadening − to model the optical depth of an absorption profile. A Voigt profile is defined as

$$V(x;\sigma,\gamma) = \int_{\infty}^{\infty} G(y;\sigma)L(x-y;\gamma)dy \tag{3.5}$$

where $G(x,\sigma)$ is a Gaussian profile of standard deviation σ and $L(x;\gamma)$ is a Lorentzian profile with $FWHM = \gamma$. Finally, y is the convolution parameter and x is the dimensionless frequency offset from the line center in units of the Doppler frequency $\Delta\nu_D$,

$$x = \frac{\nu - \nu_0/(1+z)}{\Delta\nu_D} \qquad\qquad \Delta\nu_D = \frac{b}{\lambda_0} = \frac{\sqrt{b_{th}^2 + b_{tur}^2}}{\lambda_0} \tag{3.6}$$

where $\Delta\nu_D$ is the Doppler frequency, and b is the Doppler parameter, which is decomposed in quadrature into a turbulent component, b_{tur}, accounting for macroscopic velocity motions in the cloud, and a temperature component, $b_{th} = \sqrt{\frac{2kT}{m_{atom}}}$, accounting for microscopic atomic motions, where k is the Boltzmann constant, m_{atom} is the atomic mass of the ion.

Effectively a single component line profile is modeled as

$$I(\lambda) = I_0(\lambda)e^{-\tau} = I_0(\lambda)e^{-Na_0H(a,x)}$$

where I is the observed flux, I_0 is the continuum, N is the column density, a_0 contains the atomic parameters of the line and $H(a,x)$ is the Voigt integral, both given by

$$H(a,x) = \frac{a}{\pi}\int_{\infty}^{\infty} \frac{\exp{(-y^2)}dy}{(x-y)^2 + a^2}$$

$$a_0 = \frac{\sqrt{\pi}e^2}{m_ec^2}\frac{f}{\Delta\nu_D} \qquad\qquad a = \frac{\Gamma}{4\pi\Delta\nu_D} \tag{3.7}$$

where f, λ_0, Γ are the oscillator strength, rest-frame wavelength, and transition rate of the line respectively, a is the damping parameter, and T is the temperature of the gas. Therefore using Voigt profiles to model the absorption profile directly provides physical properties of the absorbing gas. On the other hand, this method is significantly more time-consuming because of the large amount of parameters it has to fit.

The COG method is susceptible to blending and hidden saturation, and to prevent such issues a visual inspection is necessary, and hope the EW is within the linear regime. With the AODM it is possible to identify blends or saturation in an absorption profile, only when multiple lines of the same ion are available, which is not always the case. COS resolution allows one to resolve velocity components in an absorption profile, and perform Voigt profile fitting, this makes VPF the best method among those available. The biggest advantage VPF has over the other methods is that all absorption profiles of the ions present in one absorbing cloud are characterized by the same z, b_{tur}, T, which means that it is possible to draw information about the cloud from the absorption profile of every ion present in the cloud.

Ion	Transition	Wavelength (Å)	$f-$value	Ion	Transition	Wavelength (Å)	$f-$value
H I	λ1215	1215.6700	0.4164	Ni II	λ1751	1751.9157	0.0277
Al II	λ1670	1670.7886	1.740	S II	λ1250	1250.5780	0.0054
C II*	λ1335b	1335.7077	0.1150	S II	λ1253	1253.8110	0.0109
C II*	λ1335a	1335.6627	0.0127	S II	λ1259	1259.5180	0.0166
C II	λ1334	1334.5323	0.1278	Si II	λ1190	1190.4158	0.2920
Fe II	λ1142	1142.3656	0.0040	Si II	λ1193	1193.2897	0.5820
Fe II	λ1143	1143.2260	0.0192	Si II	λ1260	1260.4221	1.180
Fe II	λ1144	1144.9379	0.0830	Si II	λ1304	1304.3702	0.0863
Fe II	λ1608	1608.4508	0.0577	Si II	λ1526	1526.7070	0.1330
Ni II	λ1317	1317.2170	0.057	C IV	λ1548	1548.2049	0.1899
Ni II	λ1370	1370.1320	0.056	C IV	λ1550	1550.7784	0.0947
Ni II	λ1703	1703.4119	0.0060	Si IV	λ1393	1393.7601	0.513
Ni II	λ1709	1709.6042	0.0324	Si IV	λ1402	1402.7729	0.254
Ni II	λ1741	1741.5531	0.0427				

Table 3.1: Lines fitted with ALIS. Wavelength is in Angstrom. Rest-frame wavelengths and $f-$values come from the atomic data file provided in Cooke (2013)

3.2 Voigt profile fitting

In this thesis, I use Absorption LIne Software (ALIS; Cooke 2013) [1] to perform Voigt profile fitting on the MW absorption profile. ALIS is a χ^2 minimizing Voigt profile absorption line fitting software, similar to *VPFIT* (Carswell and Webb 2014), out of these two software ALIS is more user-friendly and self-contained, as all tools necessary to use it are readily available in the same repository. ALIS is a physically inspired Python code that simultaneously models emission and absorption using all information from all ion lines available in the data provided to the program. ALIS models are flexible with several functions to use, plus the possibility to add custom functions if needed. The input data must be provided with a Line Spread Function (LSF), which could be a simple constant $FWHM_v$, or an instrument-specific LSF, which is very useful in this case because it has implemented an easy-to-use option to include COS' LSF. This is very useful for this work because when fitting ions with saturated lines and ions with unsaturated lines simultaneously it is possible to break the degeneracy between b and N and can therefore obtain reliable N values even on saturated lines.

To carry out the fits a default starting template was used, and was adjusted on a sightline-by-sightline basis. Table 3.1 shows the ions, rest-frame wavelength, and f-values of the lines available in the wavelength coverage of the data used when fitting Voigt profiles with ALIS. Ions with largely different f-values lines in the UV were selected because fitting unsaturated lines constrains b values for all the elements for the same cloud, which is important because saturated lines poorly constrain b values, as was discussed in Section 3.1.

For each transition in Table 3.1, the absorption profile was modeled in a region of the spectra that allows one to see the full absorption profile and has enough featureless continuum. For low-ionization species a region of $\pm 300\,\mathrm{km/s}$ from $z = 0$ was used, for high ionization species a region around $\pm 450\,\mathrm{km/s}$ from $z = 0$ was used, finally, for Ly-α a region as large

---

[1] https://github.com/rcooke-ast/ALIS

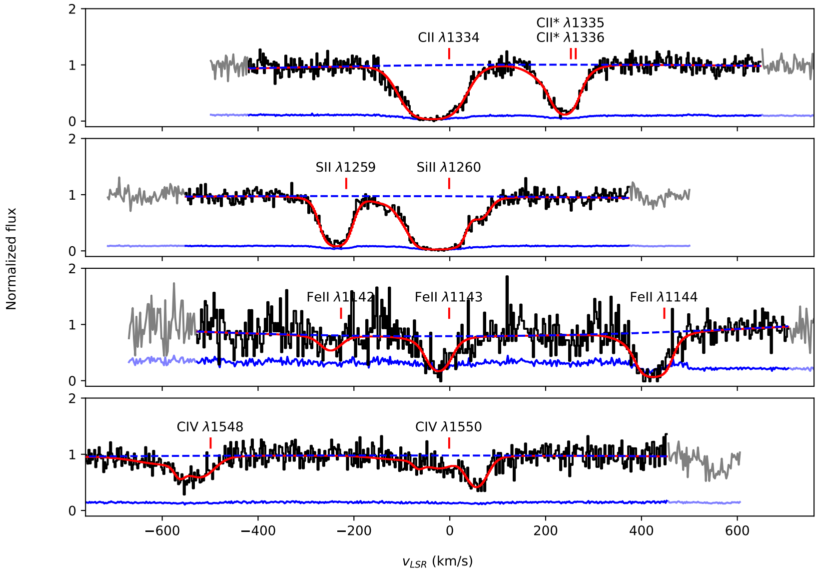

Figure 3.3: Example of Voigt profile fitting with ALIS. In this case, all transitions use the same spectral region to do the Voigt profile fitting. The grey line is the masked-out flux to run the fit, the dashed blue line is the continuum fitted by ALIS, and the red line is the fit by ALIS, red vertical lines denote the centroid of the transition at $z = 0$ and do not represent the centroid of any component in this case.

as necessary, usually ±2000 km/s from $z = 0$, this larger regions is necessary to cover the damping wings. Any absorption flagged in Section 3.2.1 was masked out and to make sure the continuum could be correctly fitted the fitting region velocity limit was increased.

In some cases, lines lie within 300 km/s from each other, so for ALIS to get a reliable fit of the continuum the wavelength ranges for those lines were merged into one, this is not a problem for ALIS because it uses all the spectral regions at the same time to model all lines. The larger spectral range considered spectra within −300 km/s from the bluer line, and 300 km/s from the redder line. This was the case for C II λ1334 with C II* λ1335b and C II* λ1335a; Fe II λ1143 and Fe II λ1142; Si II λ1260 and S II λ1259; and, when the S/N was too low for a good continuum estimation, for C IV λ1548 and C IV λ1550 too. As seen in Figure 3.3.

The optical depth profile of a given line in a given ion was modeled as a sum of (l) Voigt profiles as

$$I(\lambda) = I_0(\lambda)\exp\left(\sum_l -N_l a_{0,l} H(a_l, x)\right) \tag{3.8}$$

where x, a, a_0, are defined in 3.6 and 3.7 and are related to b_{tur}, T, and z.

Each Voigt profile in a given ion has independent z, column density (N), turbulent Doppler parameter (b_{tur}), and temperature (T). Each of these Voigt profiles is referred to as a velocity component.

Each velocity component represents a single cloud of gas along the line of sight. One cloud of gas has a set of physical properties that all ions present in the cloud should share, like z, T, and b, if b_{tur} dominates b, so all ions in a velocity component share these values, however, it is a different case for N where the relative abundance of each ion is unknown and so N is independent of each species alone.

Since the spectra are already normalized by the COS-GAL pipeline and the spectral windows are small, it is expected that the relative flux should already be close to 1, so the continuum is modeled as a second-degree Legendre polynomial with low initial values for the first and second-order coefficients and 0 for higher coefficients as

$$L(\lambda) = C_0 + C_1(\lambda - \lambda_0) + C_2 \frac{3(\lambda - \lambda_0)^2 - 1}{2} \tag{3.9}$$

where C_0 sets the continuum level at the center of the absorption, C_1 is the slope at the center of the absorption, and C_2 represents the curvature at the center of the absorption. The initial values of C_0, C_1, and C_2 were set to 1.00; 0.01; 0.01 respectively. In a few cases, the continuum had additional curvature not modeled by a second-degree polynomial to model the continuum correctly so a third-degree polynomial was used.

Before adjustment of the starting template of the model, the starting parameters for each velocity component were:

- A typical N value for that given ion, acquired by trial and error.
- z to get the line centered at the velocity centroid of the absorption relative to the systemic redshift= 0.
- b_{turb} =10 km/s to match the velocity dispersion of the metal lines typically measured in DLAs of 5-10 km/s (Noterdaeme et al. 2007).
- T was always fixed to 10 000 K because the temperature dispersion in velocity is too small to measure at this resolution. For example at T =10 000 K and b_{tur} =10 km/s

$$b_{th} = \sqrt{\frac{2kT}{m_{atom}}} = 3.2\,\mathrm{km/s}$$
$$b = \sqrt{b_{th}^2 + b_{tur}^2} = 10.5\,\mathrm{km/s} \approx b_{tur}$$

so the typical values of the Temperature and b_{th} in DLAs $\Delta b = b - b_{tur}$ are lower than what can be resolved at this resolution.

3.2.1 Interloper systems identification

To account for blends with absorption systems from outside the MW that can affect column density measurements, I visually inspected every spectrum to identify all absorption systems at z higher than the z of the MW.

The finding algorithm followed for the visual inspection was:

1. Visually inspect the spectra from the Ly-α at z_{QSO} to the Ly-α at $z = 0$ looking for Ly-α of possible intervening systems.
2. When any strong absorption line was found it was assumed to be Ly-α, then to confirm the system I looked for more Lyman-series or metal lines at that redshift, specific lines from Table F.1, this would confirm that line to be Ly-α, and the presence of an absorption system.
3. If no other lines were found at that redshift the system was discarded and the visual inspection continued.

For most intervening systems it was only possible to detect some Ly-series lines, and high ionization species such as C IV, Si IV, and O VI. The lines found at this stage were later used to mask out any portion of the spectra contaminated by absorption from gas that does not belong to the MW.

3.3 Ly-alpha fitting

To measure metallicities it is essential to quantify the total abundance of H, which can be estimated by the abundance of H I in the case the system is a DLA, as they contain mostly neutral gas. The best way to measure H I column densities is by performing a Voigt profile fitting on the only available H I transition covered: λ1215 (Ly-α).

H I λ1215 in the MW shows intense saturation, having large damping wings, as seen in the left panels of Figure 3.4. The H I column density is high enough to suspect the MW is a DLA or sub-DLA. Absorption systems that have a $N(\text{H I}) > 2 \times 10^{20}$ cm^{-2} are shielded from ionization and the ions are mostly in the neutral phase (Wolfe et al. 2005), thus hydrogen is mostly in its neutral form H I. When absorption lines are damped the column density can be accurately determined with the absorption wings.

There is a geocoronal Ly-α emission line from the H in Earth's atmosphere that blends with the absorption and can obscure the Ly-α absorption of the MW at low $N(\text{H I})$. However, if N is that low, then it is definitely not a DLA, and the H I column density would underestimate the H column density, and metallicity measurements would be inaccurate. Cases like this are discussed later in this section. This simple picture allowed me to run these fits automatically using a simple model in manually selected fitting regions.

The kinematic structure of the metal line profiles is much narrower than H I λ1215 and the continuum placement is simple, the Ly-α wings also extend much more, which makes the continuum fitting by COSGAL unreliable. Since the main source of error in the fitting of such wide absorption is continuum placement, to avoid this it was preferred to use the un-normalized spectra and let ALIS fit the continuum.

For each sightline, the wavelength range was manually selected to contain the H I λ1215 absorption and as much continuum as needed to fit the emission of the QSO. Any other absorption line contained in this range and the H I emission from the atmosphere were masked out. As seen in the left panels of Figure 3.4.

ALIS fits simultaneously the continuum and the absorption. The continuum was modeled as a second-degree Legendre polynomial, as described in Section 3.2, where the initial parameters were set to start the fitting with a flat continuum at the level of the flux near H I $\lambda1215$, which contrary to the continuum in the metal lines is not expected to be flat, because of the emission lines from the QSO, but it is a reasonable point to start. The absorption was modeled as a single Voigt profile with initial parameters: $z = 0$, $\log(N) = 20.3$, $b = 10\,\mathrm{km/s}$.

A fit is considered successful when the wings of the absorption are well-fitted and the continuum fitted by ALIS is not bent in any unnatural way.

ALIS was ran in series in all spectra, without human intervention, and yielded successful fits for 196 spectra out of the 223. Twelve systems had poor continuum fits and needed a third-order polynomial to fit the continuum. In these cases, it was necessary to use a larger region to fit the continuum and/or add a higher order to the polynomial for the continuum. In the end, it was possible to have reliable H I measurements for 209 systems. However, there were 14 systems for which it was impossible to fit Ly-α because it was either completely blended with lines from unidentified systems, or the QSO continuum was completely absorbed by Ly-limit absorption from high z absorption systems. The Ly-α fit for the first 20 QSO in alphabetical order can be seen in the right panels of Figure 3.5, and the rest is in Annex D.

A sub-sample of H I $\lambda1215$ fits can be seen in Figure 3.5, while the full sample of fits is in Annex C. In Figure 3.5 each panel shows the H I $\lambda1215$ fit, the continuum estimation, and the velocity centroid of the fit. The continuum for most sightlines is very flat and follows well the trend of the continuum. The sightline *1saxj1032.3+5051* is one of the systems that needed a third-order Legendre polynomial for the continuum fitting, in this case, to compensate for the emission near $-1500\,\mathrm{km/s}$ from $z = 0$.

3.4 Metal lines fitting

To model the absorption profile of the metal lines in a spectrum the low-ionization species and high ionization species were modeled separately because they are expected to occur in different gas volumes and do not share physical properties with the rest of the gas. The high ionization ions were modeled and the column densities were reported for completeness but were not considered for the latter discussion.

Before modeling a visual inspection of all the spectral regions around the lines fitted (Table 3.1) was done to identify the number of velocity components, check that every region was wide enough to model the continuum, and check if there were any blends or unidentified lines near the fitting regions.

When absorption lines unrelated to the MW were present within the velocity range around the MW absorption they were in most cases masked out and more spectra were added to the range. In cases where there was no remaining flux or it was heavily blended, the blends were also modeled, but the column density from the blended lines was not included in the final column density of the Milky Way.

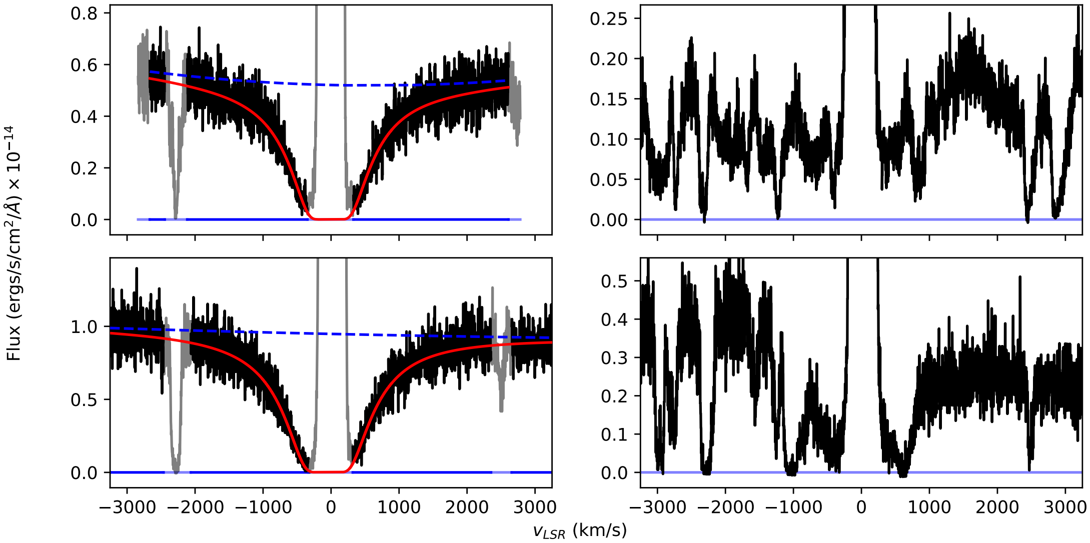

Figure 3.4: Example of H I λ1215 absorption. The left panels are spectra for which a fit was possible, and the panels on the right side show spectra for which Ly-α absorption was dominated by absorption from interlopers. In black is the un-normalized spectra, in grey is the masked-out spectra, and in solid blue is the $1-\sigma$ error array. On the left panels, the red solid line is the fit, and the dashed blue line is the fitted continuum.

A template model was used where the initial parameters and number of velocity components were adjusted manually for each spectrum in the sample.

Figure 3.6 shows the result of the ALIS fit to the metal lines of the low and high ionization species. The next few paragraphs describe the fitting process followed to model the absorption of metal lines in one spectrum applied to the system *RXS-J23218-7026* as an example of the logic used to model these lines in the sample.

The number of components in each model is selected via a visual inspection using all transitions available, where a velocity component is identified if it can be seen in more than one transition at the same ionization level. The system in Figure 3.6 has three velocity components for the low-ionization ions, and, coincidentally, three for the high-ionization ions. Red vertical lines represent the center of each component, and blue vertical lines represent blended lines from other systems, vertical lines with a star are from the MW but are not from the same absorption profile.

For the low-ionization ions, the main absorption feature at $v \sim 0$ has asymmetric wings which indicates the presence of at least two velocity components with similar velocities. In this case the bluest component has the largest N out of the three, and the middle component has a lower N but has a larger b which gives the asymmetric wings. The red-most component is completely resolved from the other two, but it is much weaker than the first component and is not detected on the weaker lines like Ni II lines. It is possible to see that Si II λ1190 is blended with S III λ1190, also the blends on C II λ1334 and other Si II lines are H I lines from an absorption system at $z = 0.3013$ identified previously in Section 3.2.1.

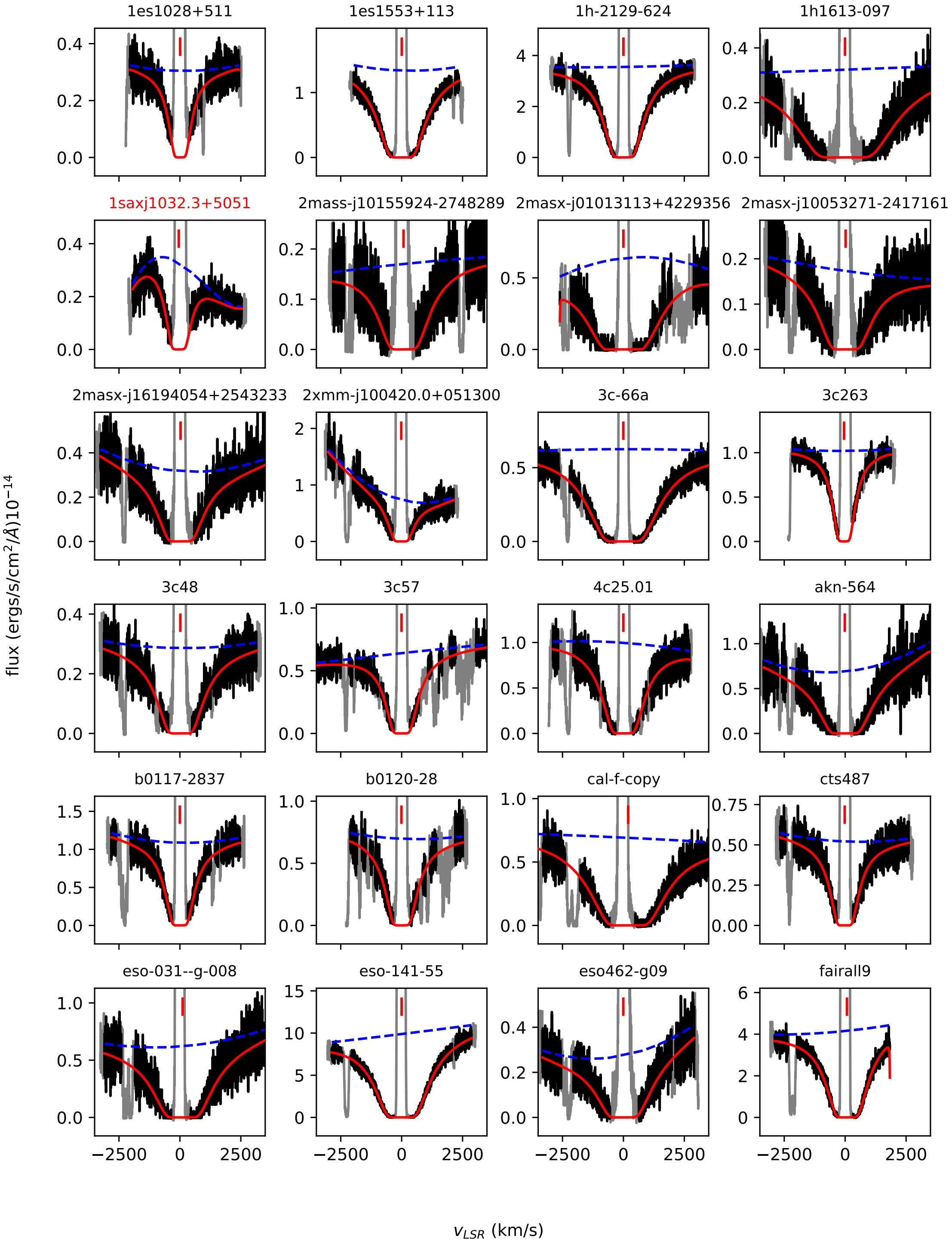

Figure 3.5: Each panel shows the ALIS fit to H I λ1215 and the name for each sightline. The black line is the un-normalized flux in ergs/s/cm^2/Å used to run the fit. The grey line is the masked-out flux to run the fit, including the geocoronal emission of H I from Earth's atmosphere, the dashed blue line is the continuum fitted by ALIS, and the red line is the fit by ALIS, red vertical lines denote the centroid of H I λ1215.

For the high ionization ions (C IV and Si IV) there are three velocity components, the bluest component is the main component, but the other two are similar in N, and b and resolved from the main component. In the C IV $\lambda1550$ profile there are two blends, these are lines from unidentified systems. Since they are unresolved from the C IV $\lambda1550$ profile I decided not to mask them out and instead fit them as metal lines from two independent systems outside of the MW. These blends are not accounted for when measuring total column density but are necessary to include to have a good fit to the data and not overestimate the column density of C IV.

The fits for all the spectra can be seen in Annex A.

3.4.1 Observation on the Line spread function

For a model to be accurate it is important to use the correct Line Spread Function (LSF), which is all the more important for COS spectra because COS LSF is unique, and changes depending on the grating used and the Lifetime Position[2](LP).

Figure 3.7 shows a simple Gaussian with a $FWHM$ similar to COS LSF's $FWHM$ and their difference. The main difference between the Gaussian profile and the LSF of COS is that the COS LSF decays slower compared to a Gaussian, meaning the lines measured by COS expand wider than when convolved by a Gaussian profile. For this reason, it is important to use the correct LP, grating, and central wavelength of the spectra to obtain the corresponding LSF for each spectra, rather than using a simple Gaussian LSF.

3.4.2 On saturated lines

Once every spectrum is fitted, it is important to review the limitations of the fitting method used, the interpretation of the results obtained, and the possible issues presented.

COS resolution is rather low to resolve the kinematic structure present in the MW gas when velocity components are blended. This means that the b value of the velocity components is not always constrained even when fitting multiple lines. VPF performed to saturated lines at this R underestimates column density and can only be used as lower limits.

Hidden saturation is also a problem that comes from the spread of absorption lines when observed with an instrument. A saturated line can be identified because the flux reaches zero, but when a saturated line is convolved with the LSF the observed profile looks like an unsaturated line. This effect is illustrated in Figure 3.8, here narrow and barely saturated lines when observed with COS can be saturated even when the minimum of the profile does not reach 0.

To address possible hidden saturation I modeled narrow just saturated lines for every transition of every ion fitted using different b values, these modeled lines were then convolved

---

[2] To mitigate the effect of gain sag, COS FUV spectra are obtained at multiple positions on the detector that are offset from each other in the cross-dispersion direction (Soderblom 2023)

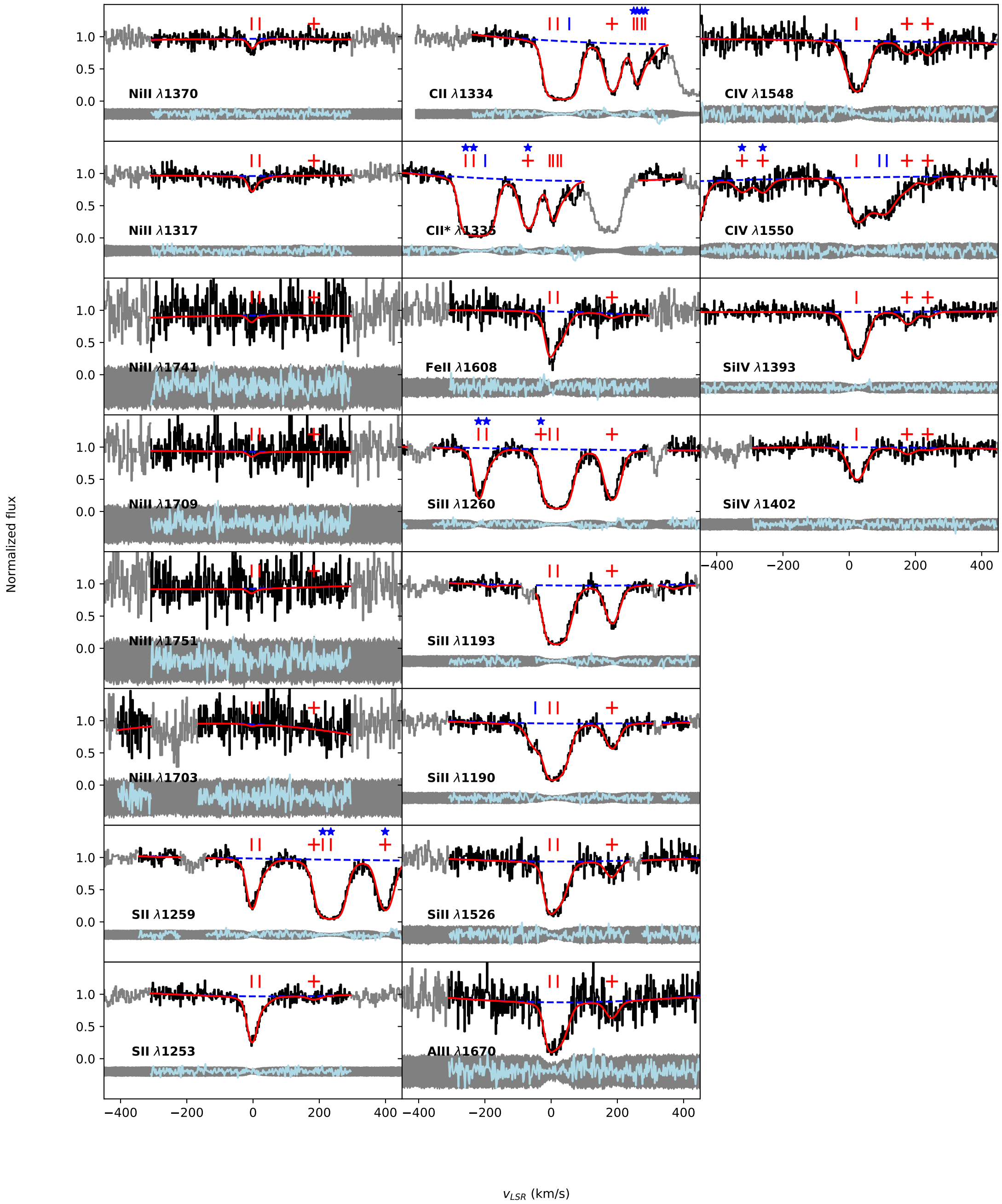

Figure 3.6: Example metal line fit. The black line is the normalized spectra for the system in QSO *RXS-J23218-7026*, the grey line is the normalized flux masked out, the dashed blue line is the continuum fitted by ALIS, the red line is the profile fitted by ALIS, red vertical lines denote the velocity centroid of Milky Way lines, red crosses mark the velocity centroid of high-velocity clouds (HVCs), blue vertical lines denote velocity centroid of blend lines, a blue star above a vertical line means a line from the MW from another species, the grey area shows 2σ contours, and finally, the light blue line is the residuals. The contour and residuals are displaced lower and scaled down for better display. The zero velocity is at v_{LSR}.

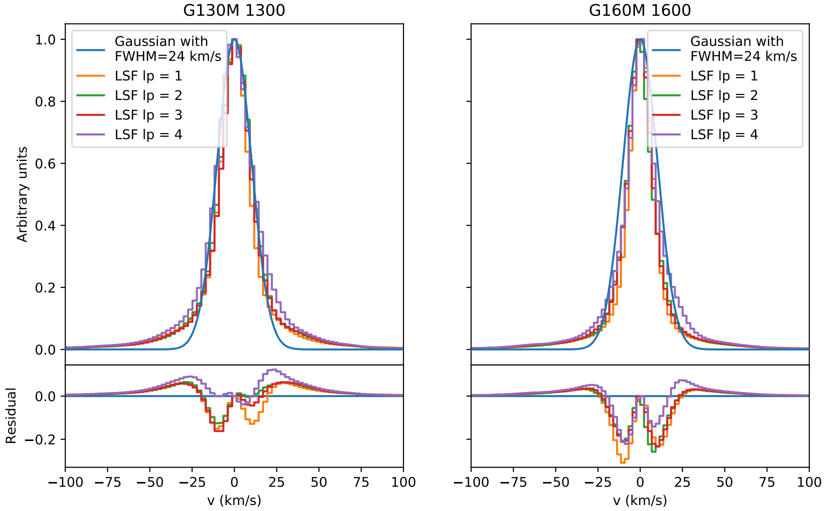

Figure 3.7: COS LSF comparison to Gaussian LSF with similar $FWHM$. In Blue is a Gaussian profile with $\sigma = 24\,\mathrm{km/s}$, and the rest are the COS LSF for different gratings and lifetime positions. The left panel shows the LSF in the bluer grating of the spectra and the right panel is the LSF in the reddest grating. The lower panels show the residual difference between the approximated Gaussian profile with the different COS LSF.

with COS LSF to find the minimum flux of these lines. To do this I used a large grid of Doppler parameters and N to model Voigt profiles, and for each b value I find the minimum N for which the minimum flux of the Voigt profile is < 0.001. This Voigt profile was then convolved with the corresponding COS LSF for that line and the minimum flux is then recorded in Table 3.2.

It is important to note that at a given b-value the simulated Voigt profile of just saturated lines are always similar to each other, because of the way N is selected. This means that the shape - and minimum flux - of the convolved profile depends mostly on the LSF used, this makes it so the minimum flux is mostly consistent between every line in the same grating regardless of the ion used.

Figure 3.8 shows the minimum flux of the convolved profile of different lines of different ions using the same colors to signify the lines in the same grating. In this figure, it is possible to see that the minimum flux of lines in the G160M grating is consistently lower than lines on the G130M grating.

A line is considered *saturated* if the minimum flux of the fit reaches its corresponding flux limit, rather than 0.

In the presence of saturated lines, a reliable determination of b is impossible and the degeneracy between b and N becomes important thus the column density measured from ALIS is unreliable. For this reason, column densities from saturated lines are reported as lower limits, and not used in this analysis. Users of the column density tables reported in this thesis are advised to operate with caution when considering to use column densities of saturated lines. The lower limits are calculated using the COG method (Draine 2011)

Ion	Line	Minimum flux	Grating
H I	1215	0.32	G130M
Ni II	1317	0.29	G130M
Ni II	1370	0.27	G130M
Ni II	1703	0.24	G160M
Ni II	1709	0.24	G160M
Ni II	1741	0.23	G160M
Ni II	1751	0.23	G160M
S II	1250	0.31	G130M
S II	1253	0.31	G130M
S II	1259	0.3	G130M
C II	1334	0.28	G130M
C II*	1335	0.28	G130M
C II*	1336	0.28	G130M
Fe II	1142	0.34	G130M
Fe II	1143	0.34	G130M
Fe II	1144	0.34	G130M
Fe II	1608	0.26	G160M
Si II	1190	0.33	G130M
Si II	1193	0.33	G130M
Si II	1260	0.3	G130M
Si II	1304	0.29	G130M
Si II	1526	0.28	G160M
Al II	1670	0.25	G160M
C IV	1548	0.28	G160M
C IV	1550	0.28	G160M
Si IV	1393	0.26	G130M
Si IV	1402	0.26	G130M

Table 3.2: Table showing transition and minimum flux recorded for a just saturated line at $b = 10\,\mathrm{km/s}$. The values here show that the trend of lower minimum flux values correlates to transitions in the higher-order grating.

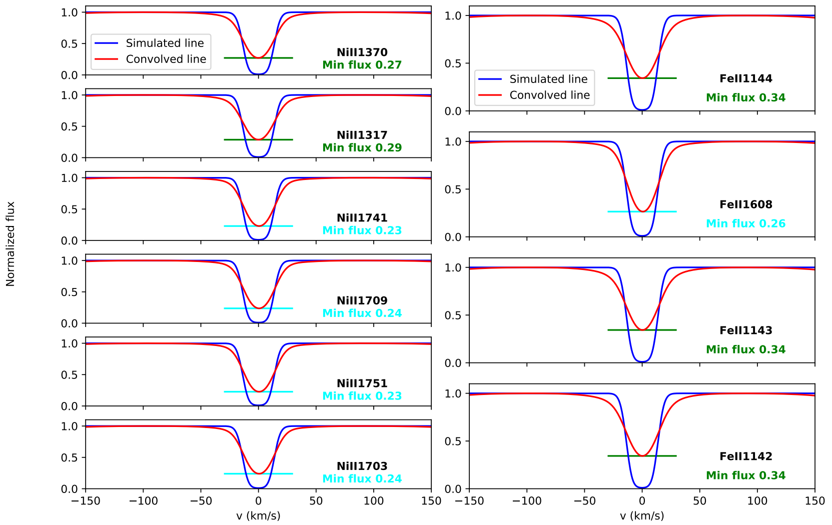

Figure 3.8: Example of hidden saturation and how it looks in different lines and gratings. Each panel shows a simulated absorption line before (in blue) and after (in red) being convoluted with COS LSF. Lines were modeled using $b = 10\,\mathrm{km/s}$. Numbers at the bottom right of each panel show the measured minimum flux, cyan font means the line falls in the G160M grating and green means the line falls in the G130M grating.

expecting to have better results than ALIS, following Equation 3.3

$$N_{sat} = 46.29 \left(\frac{b}{f\lambda}\right) \exp\left[\left(\frac{cEW}{2b}\right)^2\right] \mathrm{cm}^2\mathrm{s} \tag{3.10}$$

where b is the velocity dispersion, f, λ are the oscillator strength and rest-frame wavelength of the line with the lowest oscillator strength available for that ion, c is the speed of light in the vacuum and EW is the Equivalent width of the whole profile calculated with Eq. 3.1. The b measured by ALIS of the velocity component with the largest column density was used. Even with these precautions the COG method is still unreliable when b is not reliably determined. A detailed number of saturated lines is provided in Table 3.3.

3.4.3 Possible issues with Voigt profile fitting

Some of the issues encountered while fitting were:

1. Blends on top of the lines, or artifacts from the data reduction. In cases where blends were on top of the line, the line was either not used to model, or the blended line was modeled as a second independent system and the column density of the blend is not considered for the latter analysis. When a given fitting region had too many blends or an unreliable continuum, it was discarded, especially if other lines for the same ion were available.

2. Near Si II λ1304 there was usually a broad emission, possibly the airglow of O II λ1302 in the atmosphere, if it blended with Si II then it was discarded.
3. Si II λ1190 was in many cases blended with S III λ1190 and when the blending was strong, then S III λ1190 was fitted as a blend or Si II λ1190 was discarded. N(S III) is not reported in the final table of results.

For C II only one transition was considered, for C II* onlyλ1335 andλ1336 are considered but they are mostly blended, and for Al II there is only one transition available, meaning that if there was an unresolved blend unaccounted for then N for that ion is overestimated. There are very few ways of knowing if this is the case, so these column densities are measured and have a different flag for the user to be careful when using these values.

3.5 Results

The parameters obtained from the ALIS fit need to be interpreted to handle saturation and non-detections because ALIS always delivers a value for the parameters fitted and does not care if the results are physical as long as the model fits the data.

A velocity component is considered saturated if the minimum flux measured for that line is lower than the threshold for hidden saturation. If at least one transition of an ion fitted is not saturated, then the line is considered a detection.

On the other hand, to classify an absorption as a non-detection, near the wavelength range where the fit was performed the minimum N that could be measured with 3σ confidence with the signal-noise ratio present was calculated using Equation 3.11 from (Berg et al. 2016; Pettini et al. 1994)

$$N = \frac{3 m_e c FWHM}{\pi e^2 f \lambda^2 (1 + z_{abs}) S/N}, \tag{3.11}$$

where m_e and e are the mass and charge of the electron, c is the speed of light in vacuum, $FWHM$ is the full width at half maximum of the instrument, f, λ are the oscillator strength, and rest-frame wavelength of the line, S/N is the signal-noise ratio measured within the fitting region. The $FWHM$ of the instrument is used because these weak line profiles are probably limited by the instrument resolution rather than the gas kinematics.

If the column density measured by ALIS was lower than this $3-\sigma$ limit then it is flagged as a non-detection and the value reported is as calculated with Equation 3.11.

The total column density of a species is calculated by summing the column density of all *detected* velocity components fitted. When there are saturated components, the lower limit measured by the COG method is reported rather than the sum of all components. Again, users of the column density tables reported in this thesis are advised to operate with caution when considering to use column densities of saturated lines. When there are non-detections and detections, the total column density is just the sum of the detections, and if there are

Ion	$\#_{\text{detected}}$	$\%_{\text{detected}}$	$\#_{\text{non detected}}$	$\%_{\text{non detected}}$	$\#_{\text{saturated}}$	$\%_{\text{saturated}}$	Total
H I[a]	209	100	0	0.0	0	0.0	209
Ni II	69	33.0	139	66.5	1	0.5	209
S II	166	79.8	2	1.0	40	19.2	208
C II	1	0.5	1	0.5	201	99.0	203
C II*	121	60.8	13	6.5	65	32.7	199
Fe II	182	88.8	0	0.0	23	11.2	205
Si II	1	0.5	0	0.0	208	99.5	209
Al II	3	1.4	0	0.0	205	98.6	208
C IV	172	82.7	6	2.9	30	14.4	208
Si IV	191	92.7	3	1.5	12	5.8	206

Table 3.3: Percentage of detection, non-detection, and saturation per sightline per ion. The last column *Total* is the total number of sightlines in which it was possible to fit that ion.

[a] H I is detected on 209 sightlines and that is a condition of the sample (read Chapter 2 for details), there were 11 sightlines without H I detection, but were left out of the sample and shown on Annex D.

only non-detections then an upper limit calculated using the strongest transition of that ion available is reported. A change in this manner of interpreting the results of the model results in a change in the total column density reported and thus a change in the relative abundances and the following analysis.

Moreover, in cases where there was only one transition for one species, there could be an unexpected blend and I marked them with an asterisk on the flag and should be taken with caution.

Table 3.3 shows a detailed account of the number of detections, non-detections, and saturated lines per ion fitted.

An excerpt of the table can be seen in Table 3.4 and the full table is available in Annex B.

QSO	Glon °	Glat °	H I log(cm^{-2})	H I$_{err}$ log(cm^{-2})	H I$_{flag}$	Ni II log(cm^{-2})	Ni II$_{err}$ log(cm^{-2})	Ni II$_{flag}$	S II log(cm^{-2})	S II$_{err}$ log(cm^{-2})	S II$_{flag}$	C II log(cm^{-2})	C II$_{err}$ log(cm^{-2})	C II$_{flag}$	C II* log(cm^{-2})	C II*$_{err}$ log(cm^{-2})	C II*$_{flag}$	Fe II log(cm^{-2})	Fe II$_{err}$ log(cm^{-2})	Fe II$_{flag}$	Si II log(cm^{-2})	Si II$_{err}$ log(cm^{-2})	Si II$_{flag}$	Al II log(cm^{-2})	Al II$_{err}$ log(cm^{-2})	Al II$_{flag}$	C IV log(cm^{-2})	C IV$_{err}$ log(cm^{-2})	C IV$_{flag}$	Si IV log(cm^{-2})	Si IV$_{err}$ log(cm^{-2})	Si IV$_{flag}$
1es1028+511	161.4385	54.4393	19.89	0.01	damped	13.61	0.0	nondet	15.09	0.04	detect	14.41	0.05	satura*	13.81	0.07	detect*	14.66	0.09	detect	13.28	0.04	satura	12.51	0.13	satura*	14.12	0.04	detect	13.34	0.06	detect
1es1553+113	21.9089	43.9642	20.54	0.0	damped	13.9	0.02	detect	14.67	1.35	satura	14.02	0.98	satura*	13.88	0.02	satura*	15.09	0.04	detect	25.87	0.04	satura	12.4	0.07	satura*	13.88	0.04	satura	14.03	0.08	detect
1h-2129-624	331.1426	-42.523	20.39	0.0	damped	13.26	0.04	detect	15.39	0.01	detect	15.09	0.14	satura*	14.06	0.02	detect*	13.83	0.23	detect*	13.54	0.06	satura	12.02	0.07	satura*	14.36	0.01	detect	13.68	0.01	detect
1h1613-097	3.5308	28.4585	21.2	0.03	damped	13.72	0.0	nondet	54.48	0.55	satura	14.73	0.05	satura*	14.0	0.1	satura*	14.79	0.07	detect	13.3	0.06	satura	12.54	0.11	satura*	14.43	0.03	detect	13.86	0.04	detect
1saxj1032.3+5051	161.3704	54.5903	20.04	0.01	damped	13.8	0.0	nondet	15.16	0.05	detect	13.96	0.3	satura*	13.68	0.0	nondet	14.72	0.16	detect	13.18	0.06	satura	12.84	0.38	satura*	14.1	0.1	detect	13.52	0.09	detect
2mass-j10155924-2748289	265.6586	23.5932	20.62	0.02	damped	13.99	0.0	nondet	15.68	0.07	detect	14.56	0.25	satura*	14.16	0.15	satura*	15.36	0.34	detect	13.29	0.06	satura	13.73	0.64	satura*	14.28	0.12	detect	13.9	0.12	detect
2masx-j01013113+4229356	124.9137	-20.3398	20.98	0.02	damped	13.97	0.0	nondet	15.85	0.1	satura	...	...	...	...	...	...	15.1	0.15	detect	13.93	0.46	satura	13.26	0.5	satura*	14.18	0.05	detect	13.7	0.05	detect
2masx-j10053271-2417161	261.2302	24.8511	20.65	0.02	damped	13.82	0.0	nondet	15.35	0.07	satura	17.48	0.22	satura*	194.83	0.51	satura*	15.74	0.18	satura	13.28	0.08	satura	13.3	0.27	satura*	13.98	0.09	detect	13.58	0.05	detect
2masx-j16194054+2543233	43.5891	43.7	20.54	0.01	damped	13.79	0.0	nondet	15.5	0.05	detect	13.86	0.36	satura*	13.55	0.14	satura*	15.05	0.12	detect	13.48	0.17	satura	21.36	0.71	satura*	13.61	0.12	satura	13.37	0.04	satura
2xmm-j100420.0+051300	234.161	44.6222	20.04	0.01	damped	13.65	0.0	nondet	14.94	0.03	detect	14.2	0.16	satura*	13.75	0.1	detect*	14.4	0.11	detect	13.13	0.08	satura	12.76	0.11	satura*	14.0	0.09	detect	13.46	0.1	detect
3c-66a	140.143	-16.7669	20.92	0.0	damped	13.82	0.04	detect	15.58	0.02	satura	14.17	0.02	satura*	14.01	0.04	satura*	15.31	0.07	detect	12.66	0.05	satura	12.81	0.04	satura*	13.83	0.16	detect	13.27	0.06	detect
3c263	134.1592	49.744	19.89	0.0	damped	13.45	0.04	detect	15.25	0.02	detect	13.99	0.06	satura*	13.88	0.03	detect*	14.74	0.02	detect	13.17	0.05	satura	12.18	0.07	satura*	14.28	0.02	detect	13.75	0.01	detect
3c48	133.9626	-28.7194	20.54	0.01	damped	13.72	0.06	detect	15.43	0.03	detect	13.84	0.06	satura*	13.9	0.04	satura*	14.89	0.07	detect	13.62	0.05	satura	12.36	0.34	satura*	13.85	0.05	detect	13.38	0.04	detect
3c57	173.0773	-67.2617	20.21	0.01	damped	13.64	0.0	nondet	15.3	0.03	detect	14.1	0.31	satura*	13.93	0.05	detect*	14.83	0.09	detect	13.48	6.98	satura	12.64	0.1	satura*	13.98	0.36	detect	13.29	0.11	detect
4c25.01	114.0722	-36.2766	20.45	0.01	damped	13.66	0.11	detect	15.32	0.05	detect	14.33	0.04	satura*	14.03	0.07	detect*	14.83	0.12	detect	13.26	0.04	satura	12.39	0.17	satura*	14.12	0.06	detect*	13.74	0.06	detect
akn-564	92.1385	-25.3368	20.65	0.03	damped	13.74	0.0	nondet	15.47	0.02	detect	16.46	0.1	satura*	16.15	0.06	satura*	15.07	0.22	detect	13.59	0.05	satura	14.89	0.24	satura*	14.45	0.04	detect	13.97	0.04	detect
b0117-2837	225.7307	-83.6507	20.12	0.01	damped	13.4	0.0	nondet	15.26	0.02	detect	14.23	0.02	satura*	...	...	...	14.53	0.04	detect	13.08	0.03	satura	12.37	0.05	satura*	13.38	0.11	satura	13.76	0.03	detect
b0120-28	227.7754	-82.9332	20.2	0.01	damped	13.56	0.0	nondet	14.7	0.23	satura	13.33	0.0	nondet	13.84	0.08	detect*	14.76	0.68	satura*	13.24	0.04	satura	30.38	0.06	satura*	14.31	0.05	detect	13.61	0.05	detect
cal-f-copy	277.1769	-35.4212	20.97	0.02	damped	13.6	0.0	nondet	14.61	0.12	satura	14.44	0.14	satura*	15.28	0.28	satura*	15.25	0.1	detect	13.62	0.05	satura	12.73	0.12	satura*	14.47	0.04	detect	13.73	0.04	detect
cts487	5.5445	-69.4435	20.11	0.01	damped	13.53	0.0	nondet	15.18	0.04	detect	13.43	0.24	satura*	13.92	0.06	detect*	14.69	0.08	detect	12.58	0.07	satura	13.5	0.27	satura*	14.05	0.09	detect	13.12	0.1	detect
eso-031–g-008	290.3276	-40.7937	20.75	0.03	damped	13.83	0.0	nondet	15.43	0.02	detect	14.33	0.1	satura*	15.2	0.21	satura*	15.04	0.05	detect	13.15	0.08	satura	12.33	0.44	satura*	14.41	0.04	detect	13.69	0.05	detect
eso-141-55	338.1834	-26.7112	20.68	0.0	damped	13.66	0.03	detect	15.27	0.01	detect	14.1	0.05	satura*	13.69	0.04	satura*	14.82	0.01	detect*	13.92	0.03	satura	12.72	0.05	satura*	14.47	0.01	detect	13.8	0.01	detect
eso462-g09	11.3254	-31.9488	20.68	0.02	damped	13.8	0.0	nondet	15.45	0.14	detect	35.13	0.07	satura*	14.11	0.17	detect*	14.08	0.24	detect	13.79	0.28	satura	12.57	0.39	satura*	14.37	0.76	satura	13.58	0.07	detect
fairall9	295.0729	-57.8266	20.44	0.01	damped	13.31	0.03	detect	15.64	0.04	detect	14.63	0.02	satura*	13.7	0.05	detect*	17.95	0.03	detect	13.4	0.09	satura	12.64	0.05	satura*	14.31	0.02	detect	13.68	0.02	detect
fbqsj1010+3003	198.4271	54.6252	20.37	0.01	damped	13.62	0.0	nondet	15.37	0.28	satura	113.27	0.27	satura*	13.96	0.04	satura*	15.14	0.1	detect	138.03	0.18	satura	12.96	0.22	satura*	14.05	0.1	detect	13.54	0.04	detect
galex-j022614.4+001530	166.5701	-54.3763	20.37	0.01	damped	13.64	0.0	nondet	15.6	0.05	detect	14.26	0.3	satura*	22.22	0.07	satura*	14.0	0.39	satura*	13.42	0.13	satura	12.43	0.71	satura*	14.03	0.06	detect	13.65	0.05	detect
hb89-0107-025-ned05	134.0292	-64.7794	20.38	0.01	damped	13.6	0.0	nondet	15.25	0.04	detect	17.03	0.18	satura*	14.06	0.05	detect*	14.59	0.13	detect	13.69	0.22	satura	13.82	0.74	satura*	14.11	0.03	detect	13.23	0.07	detect
hb89-0202-765	297.5486	-40.0452	20.7	0.02	damped	13.72	0.0	nondet	15.34	0.05	detect	13.74	0.33	satura*	13.8	0.32	satura*	17.5	0.22	detect	15.98	0.2	satura	13.21	0.06	satura*	13.53	0.09	satura	13.16	0.58	satura
hb89-0232-042	174.4627	-56.1555	20.21	0.01	damped	13.8	0.0	nondet	15.21	0.03	detect	14.34	0.05	satura*	13.84	0.05	detect*	14.58	0.11	detect*	13.25	0.05	satura	12.33	0.17	satura*	13.85	0.05	detect	13.27	0.05	detect
he0056-3622	293.7191	-80.898	20.17	0.0	damped	13.38	0.0	nondet	15.12	0.06	detect	13.83	0.06	satura*	13.67	0.04	detect*	14.43	0.02	detect	12.84	0.09	satura	12.66	0.06	satura*	14.4	0.06	detect	13.7	0.05	detect
he0153-4520	271.7958	-67.975	20.04	0.01	damped	13.33	0.0	nondet	15.38	0.04	detect	13.68	0.09	satura*	13.78	0.04	detect*	14.67	0.12	detect	12.89	0.06	satura	45.93	0.21	satura*	14.13	0.04	detect	13.47	0.04	detect
he0226-4110	253.9407	-65.7748	20.1	0.0	damped	13.53	0.04	detect	15.34	0.02	detect	13.53	0.08	satura*	13.87	0.03	detect*	14.75	0.05	detect	12.82	0.02	satura	16.0	0.12	satura*	13.99	0.06	detect*	13.48	0.04	detect
he0238-1904	200.4801	-63.6337	20.4	0.0	damped	13.33	0.0	nondet	14.54	0.19	satura	13.57	0.09	satura*	26.48	0.13	satura*	14.62	0.15	detect	12.79	0.05	satura	17.78	0.21	satura*	14.06	0.06	detect	13.51	0.06	detect
he0435-5304	261.0247	-41.3746	19.69	0.02	damped	13.63	0.0	nondet	14.97	0.03	detect	14.28	0.09	satura*	13.49	0.0	nondet	14.69	0.1	detect	13.09	0.07	satura	12.47	0.16	satura*	14.27	0.04	detect	13.32	0.05	detect
he0439-5254	260.6931	-40.9014	19.63	0.02	damped	13.5	0.0	nondet	14.98	0.02	detect	14.3	0.11	satura*	14.43	0.03	satura*	14.61	0.05	detect	13.21	0.05	satura	12.32	0.14	satura*	14.18	0.08	detect	13.36	0.07	detect
hs-0033+4300	120.0257	-19.5089	20.74	0.04	damped	13.71	0.09	detect	15.52	0.07	detect	17.43	0.14	satura*	14.45	0.1	detect*	14.83	0.08	detect	13.76	0.1	satura	13.7	0.17	satura*	14.33	0.05	detect	13.35	0.19	detect*
hs1102+3441	188.5633	66.2186	20.12	0.01	damped	13.8	0.07	detect	15.45	0.03	detect	13.85	0.52	satura*	14.02	0.04	detect*	14.93	0.1	detect	13.65	0.04	satura	12.45	0.13	satura*	14.04	0.01	detect	13.64	0.02	detect
icrf-j122011.8+020342	284.9919	63.84	20.19	0.01	damped	13.64	0.0	nondet	15.29	0.05	detect	15.31	0.62	satura*	14.02	0.1	detect*	14.99	0.07	detect	13.98	0.23	satura	13.15	0.95	satura*	14.39	0.02	detect	13.77	0.03	detect
io-and	122.2786	-23.1812	20.61	0.0	damped	13.8	0.02	detect	15.73	0.01	detect	13.85	0.03	satura*	13.96	0.03	satura*	15.23	0.04	detect	12.65	0.06	satura	12.41	0.06	satura*	14.33	0.02	detect	13.62	0.02	detect
iras-f04250-5718	266.9868	-41.9963	19.95	0.0	damped	13.33	0.01	detect	15.47	0.01	detect	...	...	...	...	...	...	14.71	0.01	detect	12.97	0.05	satura	11.98	0.07	satura*	14.31	0.01	detect	13.73	0.01	detect
iras-f22456-5125	338.5115	-56.6295	19.79	0.0	damped	13.06	0.0	nondet	15.28	0.06	detect	...	...	...	...	...	...	14.47	0.13	detect	13.25	0.23	satura	12.32	0.42	satura*	13.97	0.04	detect	13.33	0.01	detect
iras-l06229-6434	274.3115	-27.3195	20.53	0.0	damped	13.63	0.09	detect	14.59	0.04	satura	14.37	0.08	satura*	...	...	...	14.98	0.04	detect	12.97	0.14	satura	12.19	0.21	satura*	14.21	0.03	detect	13.63	0.02	detect
irasf00040+4325	114.4161	-18.4214	20.91	0.01	damped	13.48	0.08	detect	15.45	0.04	satura	13.67	0.06	satura*	36.43	0.13	satura*	15.13	0.07	detect	12.63	0.06	satura	27.27	0.1	satura*	13.44	0.0	nondet	13.3	0.04	detect
izw1	123.7485	-50.175	20.67	0.02	damped	13.41	0.0	nondet	15.61	0.02	detect	13.73	0.05	satura*	14.09	0.05	detect*	15.01	0.16	detect	25.12	0.03	satura	24.09	0.05	satura*	14.08	0.04	detect	13.35	0.04	detect
j141949.39+060654.0	351.9189	60.2851	20.25	0.02	damped	13.85	0.0	nondet	15.04	0.05	detect	17.95	0.15	satura*	13.91	0.11	detect*	14.51	0.09	detect	15.05	0.36	satura	13.45	0.54	satura*	14.44	0.08	detect	13.76	0.06	detect
kaz238	110.9649	-28.3522	20.76	0.02	damped	13.78	0.0	nondet	15.44	0.06	detect	14.08	0.26	satura*	14.27	0.06	detect*	14.8	0.14	detect	14.22	0.14	satura	12.95	0.41	satura*	13.95	0.07	detect	13.5	0.06	detect
lbqs-0107-0235	134.0062	-64.7985	20.36	0.02	damped	13.59	0.0	nondet	15.17	0.05	detect	14.2	0.04	satura*	13.92	0.08	detect*	14.68	0.08	detect	16.07	0.03	satura	14.32	0.05	satura*	14.07	0.05	detect	13.39	0.07	detect
lbqs-1435-0134	348.7184	51.3746	20.41	0.01	damped	13.58	0.03	detect	15.42	0.02	detect	15.65	0.04	satura*	14.13	0.02	detect*	14.39	0.03	satura*	15.12	0.02	satura	15.93	0.02	satura*	14.07	0.01	satura	13.78	0.02	detect
mark509	35.9711	-29.8554	20.53	0.0	damped	13.57	0.01	detect	14.73	0.0	satura	14.11	0.05	satura*	13.83	0.01	satura*	14.47	0.0	satura*	16.39	0.01	satura	11.84	0.05	satura*	13.55	0.02	satura	13.96	0.0	detect
mr2251-178	46.1974	-61.3256	20.38	0.0	damped	13.51	0.06	detect	15.39	0.01	detect	27.45	0.05	satura*	14.0	0.02	detect*	14.68	0.04	detect	13.47	0.03	satura	12.09	0.06	satura*	14.39	0.06	detect	13.8	0.06	detect
mrk-1044	179.6945	-60.4774	20.41	0.01	damped	13.49	0.05	detect	15.29	0.01	detect	13.93	0.05	satura*	13.93	0.04	detect*	14.55	0.06	detect	14.21	0.03	satura	12.92	0.13	satura*	13.8	0.04	detect	13.36	0.04	detect
mrk-1253	246.6971	42.3646	20.57	0.02	damped	13.83	0.0	nondet	14.82	0.05	satura	20.55	0.91	satura*	13.57	0.15	satura*	15.28	0.18	detect	13.23	0.03	satura	12.73	0.15	satura*	13.9	0.05	satura	13.67	0.05	detect
mrk-279	115.0415	46.8647	20.16	0.02	damped	13.81	0.0	nondet	15.24	0.03	detect	14.87	0.12	satura*	14.13	0.08	detect*	14.94	0.06	detect	13.94	0.04	satura	15.67	0.12	satura*	14.27	0.05	detect	13.7	0.06	detect
mrk-335	108.7632	-41.4245	20.48	0.0	damped	13.37	0.24	detect	13.97	0.68	satura	13.94	0.04	satura*	14.13	0.08	detect*	14.62	0.08	detect	13.04	0.03	satura	12.1	0.08	satura*	14.24	0.05	detect	13.58	0.09	detect
mrk106	161.1387	42.8795	20.43	0.01	damped	13.63	0.03	detect	15.21	0.02	detect	14.14	0.03	satura*	23.69	0.02	satura*	14.89	0.05	detect	13.1	0.03	satura	12.21	0.1	satura*	13.67	0.05	detect	13.25	0.04	detect
mrk1148	123.0933	-45.4387	20.6	0.02	damped	13.55	0.0	nondet	15.21	0.03	detect	25.93	0.08	satura*	13.97	0.03	detect*	14.92	0.17	detect	12.5	0.09	satura	12.58	0.09	satura*	13.72	0.07	satura	13.2	0.07	satura
mrk1179	148.8953	-29.7454	20.82	0.02	damped	13.82	0.0	nondet	15.32	0.02	detect	24.41	0.4	satura*	14.08	0.09	detect*	14.54	0.07	detect	13.3	0.11	satura	14.05	0.34	satura*	13.71	0.14	detect	13.43	0.14	detect
mrk1392	2.754	50.264	20.52	0.0	damped	13.71	0.04	detect	15.31	0.07	detect	14.13	0.16	satura*	14.25	0.05	detect*	15.06	0.05	detect	13.66	0.07	satura	14.61	0.23	satura*	13.35	0.2	satura	12.62	0.26	satura
mrk1513	63.6699	-29.07	20.52	0.0	damped	13.56	0.03	detect	15.81	0.01	detect	13.8	0.1	satura*	14.49	0.02	satura*	14.94	0.05	detect	12.84	0.07	satura	12.02	0.16	satura*	14.6	0.02	detect	13.81	0.01	detect
mrk290	91.4892	47.9536	20.34	0.01	damped	13.47	0.05	detect	15.2	0.01	detect	282.55	0.32	satura*	14.01	0.03	detect*	15.28	0.11	detect	15.99	0.03	satura	12.98	0.04	satura*	14.26	0.06	detect	13.67	0.07	detect
mrk352	125.0262	-31.0104	20.7	0.01	damped	13.85	0.11	detect	15.57	0.02	detect	13.91	0.12	satura*	14.16	0.09	detect*	15.16	0.13	detect	12.52	0.12	satura	13.74	0.25	satura*	14.44	0.03	detect	13.66	0.06	detect
mrk817	100.2997	53.4783	20.03	0.01	damped	13.18	0.05	detect	15.42	0.01	detect*	13.75	0.39	satura*	13.59	0.02	detect*	15.04	0.2	detect	12.37	0.02	satura	12.45	0.06	satura*	14.11	0.05	detect	13.55	0.04	detect
mrk841	11.2091	54.6321	20.25	0.02	damped	13.57	0.07	detect	15.34	0.01	detect	15.07	0.08	satura*	14.31	0.08	detect*	15.11	0.05	detect	18.63	0.04	satura	13.52	0.09	satura*	13.72	0.03	satura	14.07	0.02	detect
mrk876	98.2694	40.3757	20.35	0.0	damped	13.83	0.01	detect	15.55	0.01	detect	...	...	...	...	...	...	15.16	0.01	detect	13.75	0.01	satura	12.54	0.02	satura*	14.31	0.01	detect	13.78	0.01	detect
newqz008	165.7166	-66.3445	20.31	0.01	damped	13.83	0.0	nondet	15.43	0.08	detect	13.85	0.15	satura*	14.02	0.12	detect*	14.93	0.21	detect	13.02	0.08	satura	15.88	0.5	satura*	13.9	0.08	detect	13.37	0.08	detect
newqz026	92.3171	-70.888	20.45	0.04	damped	13.89	0.0	nondet	15.38	0.05	detect	14.06	0.26	satura*	13.95	0.13	detect*	14.5	0.18	detect	13.64	0.07	satura	12.82	0.21	satura*	13.88	0.25	satura	13.9	0.15	detect
ngc-3516	133.2357	42.4028	20.33	0.02	damped	13.55	0.0	nondet	15.53	0.02	detect	14.17	0.06	satura*	14.23	0.04	detect*	15.02	0.08	detect	13.02	0.04	satura	21.87	0.17	satura*	13.77	0.03	detect	13.38	0.03	detect
ngc-3783	287.456	22.9475	20.98	0.0	damped	13.74	0.03	detect	16.23	0.12	satura	13.56	18.83	satura*	13.45	0.19	satura*	15.54	0.1	detect	13.25	0.02	satura	12.65	0.07	satura*	14.31	0.02	detect	13.79	0.02	detect
ngc-5548	31.9606	70.4958	20.13	0.0	damped	13.64	0.01	detect	15.3	0.05	detect	13.68	0.01	satura*	13.71	0.13	detect*	14.82	0.02	detect	13.27	0.05	satura	11.85	0.02	satura*	14.44	0.0	detect	13.82	0.0	detect
ngc-7469	83.0986	-45.4667	20.62	0.0	damped	13.32	0.04	detect	15.18	0.01	detect	14.9	0.21	satura*	13.92	0.0	nondet	14.74	0.02	detect	29.61	0.02	satura	25.32	0.11	satura*	14.39	0.01	detect	13.81	0.01	detect

Table 3.4: Extract of the measured Column densities by ALIS. QSO name as reported in the HSLA first data release (Peeples et al. 2017), galactic positions are in degrees, column densities are reported in log-scale, and an asterisk next to the flag means that only one line was available.

Chapter 4

Milky Way metals and alpha elements abundances

In this chapter, I study the distribution of $N(\text{H I})$ across galactic latitude and compare it to $N(\text{H I})$ from 21-cm maps of the MW. I also study the relation between metallicity in these absorption systems and galactic latitude and compare it to other ISM metallicity measurements. Finally, I compare the $[\alpha/\text{Fe}]$ ratio from this work to the same ratio measured in the atmosphere of stars, and separately, with $[\alpha/\text{Fe}]$ measured in the ISM of the solar neighborhood, to confirm whether it is feasible to compare the $[\alpha/\text{Fe}]$ ratio measured with different methods.

4.1 N(HI) spatial distribution.

The 209 QSO sightlines from which there are H I column density measurements are plotted against Galactic latitude (b) in Figure 4.1. There is a trend of increasing N with decreasing b, which is expected from $N(\text{H I})$ studies in 21-cm emission (HI4PI Collaboration et al. 2016) and the disk morphology of the MW that presents higher densities of gas near the disk, at low galactic latitudes.

To confirm the robustness of the column density measurements, they were compared to the H I column density calculated from 21-cm emission from (HI4PI Collaboration et al. 2016) integrated over the full velocity range covered by their observations ($-600 < v_{LSR} < 600$km/s). To compare both measurements I use the relative difference between these measurements and the column density in the same direction measured by (HI4PI Collaboration et al. 2016) calculated following:

$$\Delta_{rel}\% = 100 \times \frac{|N(\text{H I})_{HI4PI} - N(\text{H I})|}{N(\text{H I})_{HI4PI}} \tag{4.1}$$

Figure 4.2 shows this relative difference as a function of column density. From this Figure it is possible to see that the 75th percentile of the differences is $\lesssim 20\%$, meaning that overall $N(\text{H I})$ from this work is in agreement with what can be measured in emission. This is as

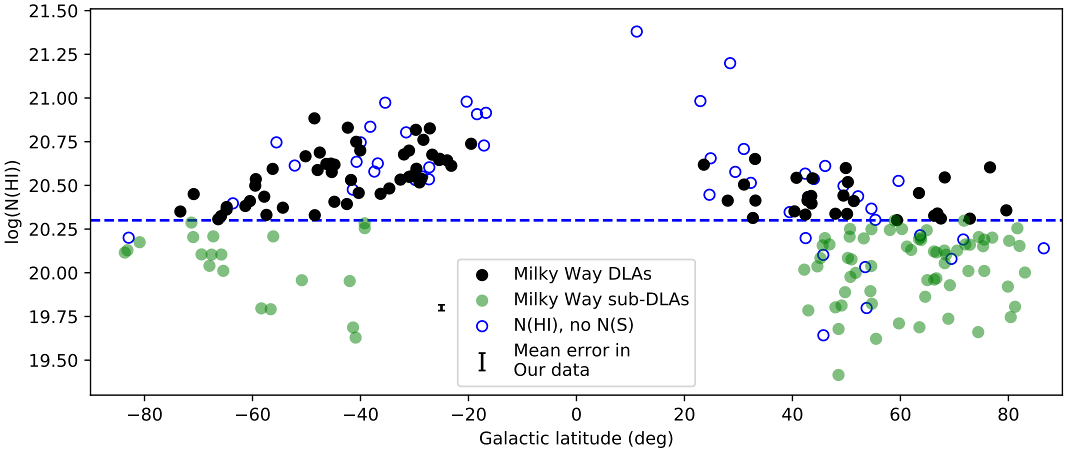

Figure 4.1: H I column density as a function of galactic latitude. Black points are the MW DLAs, green circles are the sub-DLA sample, and blue open circles are sightlines for which one is able to measure $N(\text{H I})$, but no $N(\text{S II})$, and the blue dashed line marks $log(N(HI)) = 20.3$.

expected because the velocity range measured in this thesis includes the full range of velocities probed by (HI4PI Collaboration et al. 2016).

Moreover, the larger differences, except for one sightline, tend to be at lower column densities, which is to be expected as gas clouds with N lower than 20.3 are affected by ionization and the column density could be underestimated. These larger differences can also happen because the absolute differences decrease slower than the column density, increasing the relative difference.

There is one particular system that has a large $\Delta_{rel} = 89\%$ despite having $N(\text{H I})> 10^{20.3}\text{cm}^{-2}$, system *SDSSJ122035.10+385316.4*, the model for this system was done again with a larger spectral region for the continuum, and a higher order polynomial to account for a previously missed shallow emission line. With this new model, the column density did not change significantly, confirming the robustness of the model.

To stress the similarities between these measurements of column density and the 21-cm emission column density Figure 4.3 shows both samples in galactic coordinates in Hammer-Aitoff projection using the same color scale. Here it is possible to see that the points from this work blend in very well with the background, which is a sign that both measurements are well in agreement.

4.2 Metallicity distribution.

Now that the column density for H I is reliably measured, the next step is to measure the abundance of metals to derive the metallicity of the gas phase. Systems with $log(N(HI)) > 20.3$ are self-shielded from ionization and H is mostly neutral (N(H I)≃N(H)). Abundance of element X is measured relative to solar abundances as $[X/H] = \log\left(N(X)/N(H)\right) -$

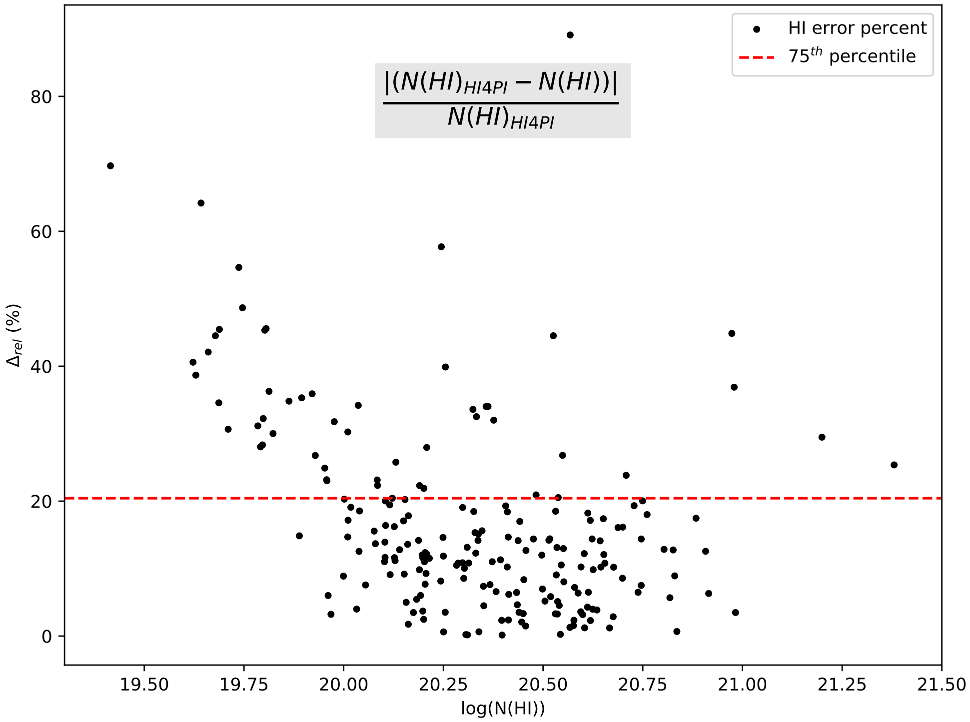

Figure 4.2: Relative error of $N(\mathrm{H\,I})$ measured here relative to the $N(\mathrm{H\,I})$ 21cm emission map from (HI4PI Collaboration et al. 2016). The red dashed line shows the position of the 75th percentile, demonstrating that 75% of the relative errors in the sample are below 20%.

$\log\left(N(X)_{\odot}/N(H)_{\odot}\right)$, where the solar abundances are from (Asplund et al. 2009).

Metallicity is measured following the scheme by Rafelski et al. (2014) that uses the abundance of either O, or N, Si, S, or Fe, in that order of priority depending on the availability of reliable measurements. This scheme uses mostly α-elements and is the most common scheme when studying DLAs. In this work, column densities for O or N were not measured, and Si was saturated in 99% of the sample, so the abundance of S is taken as the metallicity proxy ([S/H] = [M/H]; [M/H] is metallicty).

After excluding sightlines that do not have both S II and H I column densities the remaining sample comprises 163 sightlines. Out of these, 79 have $log(N(HI)) > 20.3$. Absorption systems that have $log(N(HI)) > 20.3$ are thought to be shielded by ionization, at high redshift they are called Damped Lyman-α systems (Wolfe et al. 2005). For this reason, column densities in these systems are not corrected by ionization. This sub-sample will be referred to as *MW DLAs*.

The other 84 sightlines have sub-DLA H I column density and will be referred to as MW sub-DLAs. At $z < 3$ sub-DLAs appear more metal-rich than DLAs at the same redshift (Khare et al. 2007), particularly for $z < 1.5$ sub-DLAs are selected for the presence of strong Mg II lines, which can bias selection to metal-rich systems. However, in the redshift range $3 < z < 4.3$ metal enhancement comes from ionization effects, and correcting for this effect leads to sub-DLAs being up to ~ 1 dex lower metallicity than DLAs (Berg et al. 2021).

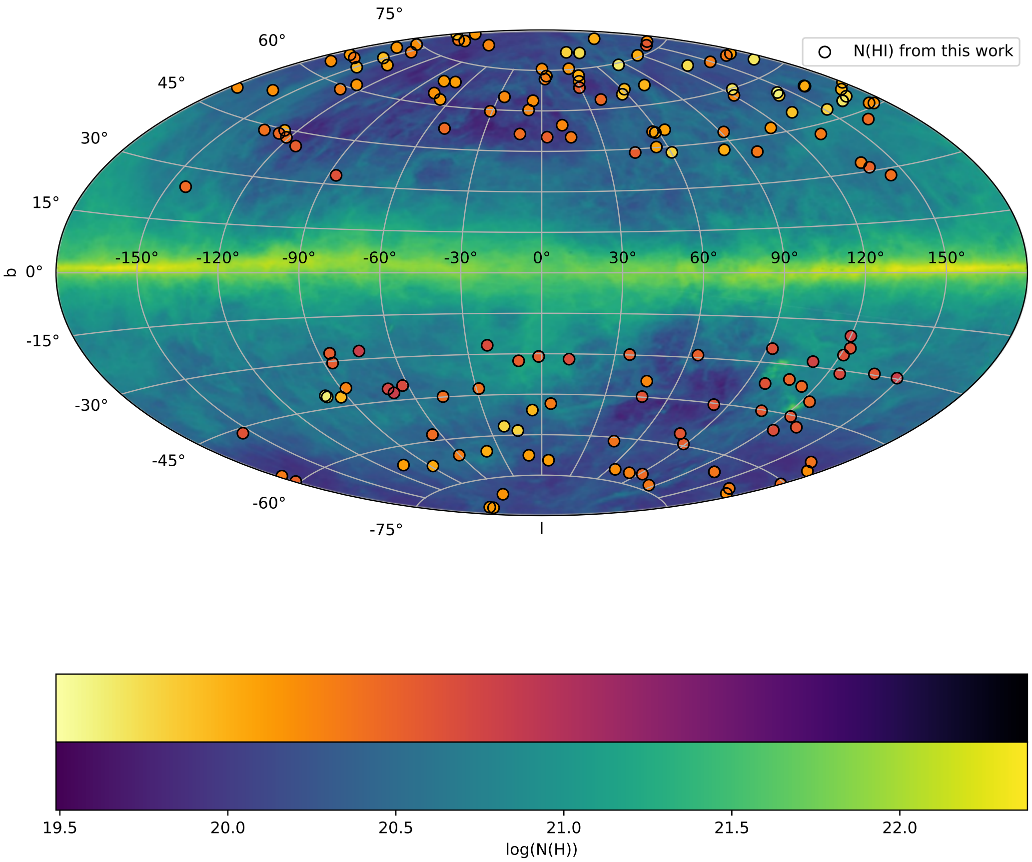

Figure 4.3: Comparison of $N(\text{H I})$ column density map in galactic coordinates in Hammer-Aitoff projection. Circles are $N(\text{H I})$ measured here, and the background is a column density map from (HI4PI Collaboration et al. 2016) 21-cm emission of the Milky Way.

Exploring the possibility of ionization corrections to the MW sub-DLAs is beyond the scope of this thesis, instead, I focus only on the MW DLAs for which metal abundances are accurately measured.

The total H I weighted metallicity of MW DLAs calculated as

$$[M/H]_{total} = \sum_i \left(\frac{\sum_i [M/H]_i \times 10^{N(HI)_i}}{\sum_i 10^{N(HI)_i}} \right) \tag{4.2}$$

is $[M/H]_{total} = 0.39$ and is overall constant with b, and has a scatter larger than expected from the uncertainties. Figure 4.4 shows [M/H] as a function of galactic latitude with the addition of metallicity measurements from (de Cia et al. 2021), who used solar neighborhood stars as background sources to do spectroscopy of the gas in the solar neighborhood.

To better see any possible trend of metallicity with galactic latitude the MW DLAs were binned into groups of $11 - 13$ systems and calculated the H I weighted mean in each bin. The binned metallicities in Figure 4.4 do not show any trend with galactic latitude, but at $b \sim -40°$ there is a group of the most metal-poor sightlines that coincide with the galactic latitude Magellanic Stream (MS). The MS is the most massive ($3 \times 10^9 M_\odot$) high-velocity structure in the MW, and over the next 0.5− 1.0 Gyr it is expected to feed the MW with large amounts of mostly metal-poor gas (Richter et al. 2017), which makes this dip in metallicity expected.

Figure 4.5 shows a galactic projection map of metallicity. In both Figure 4.4 and 4.5 it is possible to see the same trend that metallicity changes non-systematically with galactic latitude, this is in agreement with (de Cia et al. 2021) where they found that metallicity in the solar neighborhood ISM changes drastically with position in the sky even when the sightlines were close in angular separation.

The ISM metallicity is mostly sub-solar in the solar neighborhood (de Cia et al. 2021), this agrees with the metallicities of the MW DLAs that probe the CGM and ISM as seen on 4.4. To confirm this, I decided to use a Monte Carlo approach for a two-sided Kolmogorov-Smirnov test by resampling the data 10,000 times within their Gaussian uncertainties and running one KS test each time. This approach provides one with a p-value distribution. This process will be referred to as an MC KS test. The mean of the distribution is 0.38 and the middle 50% of the distribution is within +0.228 and -0.168. This result cannot confidently reject the hypothesis of both samples coming from the same parent distribution $\lesssim 70\%$ of the time.

Moreover, this confirms that the hypothesis of the MW having solar metallicity is biased by regions in the MW affected by ionization (sub-DLAs sightlines) and that the true metallicity of the MW's neutral gas is sub-solar.

4.3 Alpha-element abundances

SNe are the main source of metals in the ISM. Depending on the type of SN they yield different elements to the ISM and occur on different timescales. SN type II occurs in the

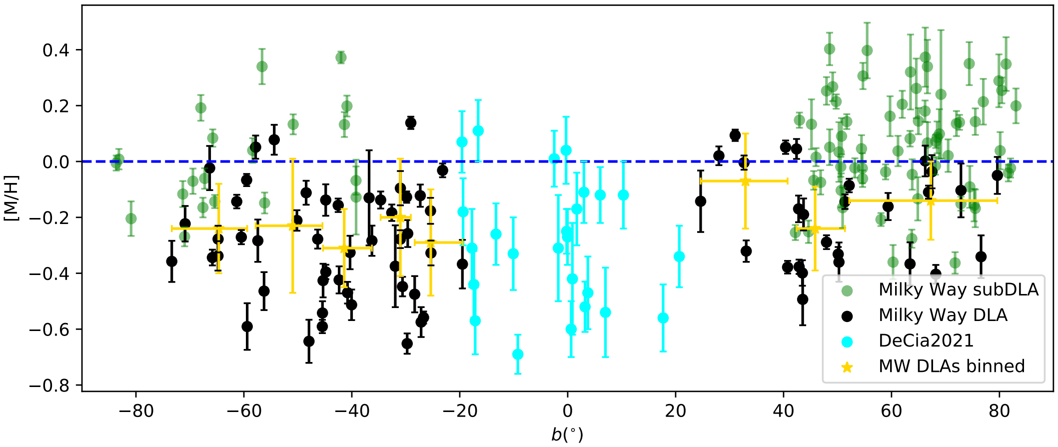

Figure 4.4: [M/H] as a function of galactic latitude. Black circles are MW DLAs, green circles are MW sub-DLAs, cyan circles are from (de Cia et al. 2021), and yellow stars are H I weighted binned metallicities of MW DLAs. The blue dashed line marks solar metallicity.

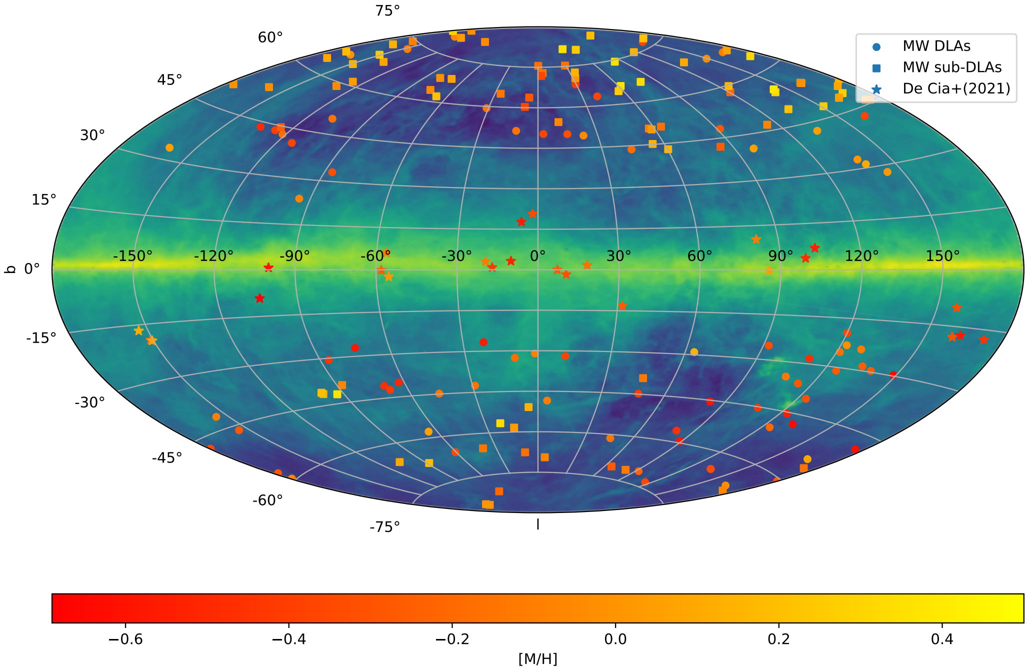

Figure 4.5: [M/H] in galactic coordinates in Hammer-Aitoff projection. Circles are measured from this work, and stars are from (de Cia et al. 2021). Background is a column density map from (HI4PI Collaboration et al. 2016) 21-cm emission of the Milky Way.

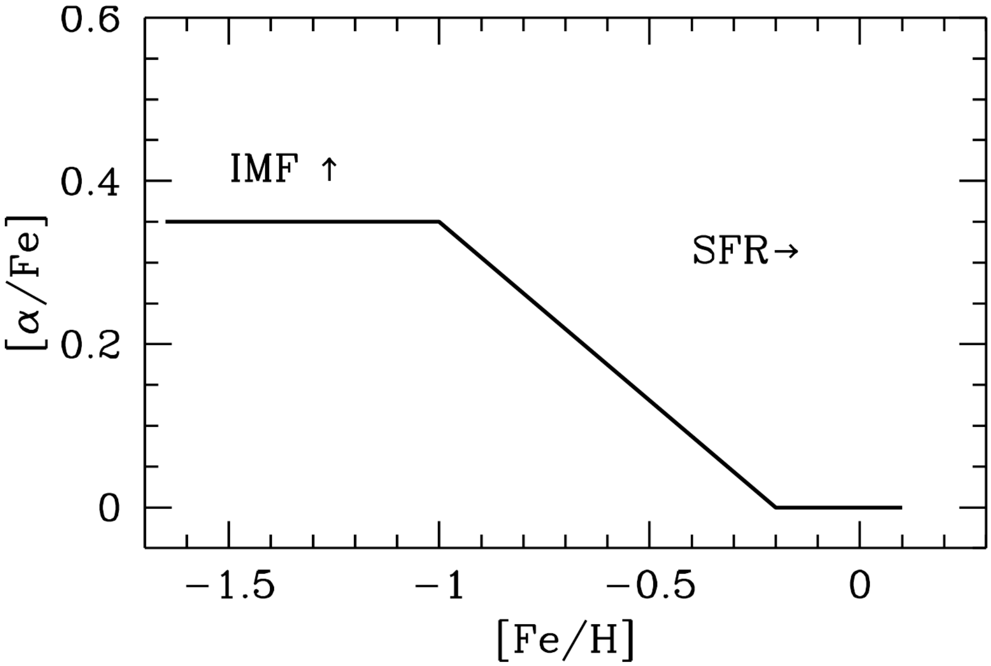

Figure 4.6: Schematic representation of [α/Fe] as a function of [Fe/H] from McWilliam (1997).

most massive and short-lived stars. In contrast, SN type Ia takes longer to start occurring because they need a binary system where one star has to evolve into a white dwarf and the other star has to develop into a giant red star and accrete mass into the first. Both types of SN yield different metals into the ISM and the ratio of α-elements and Fe-peak elements ([α/Fe]) is sensitive to the number of SN of each type that has occurred in the history of a galaxy. This effect is illustrated in Figure 4.6 from McWilliam (1997), where the plateau at [Fe/H]< -1 represents times where only SN II occur, and at [Fe/H]> -1 SN Ia starts happening and the [α/Fe] ratio decreases.

As a galaxy is enriched only by SN II, then [α/Fe] stays constant at the yield of SNII, which is ~ 0.3 in the MW, this regime is called the *plateau* and when SN Ia starts to happen they dominate Fe production and [α/Fe] lowers, the metallicity at which this change occurs is referred to as the *knee*. The metallicity of the knee constrains the level of enrichment and the mass of the system (Tolstoy et al. 2009).

[α/Fe] has been studied extensively in the MW (Reddy et al. 2003; Reddy et al. 2006; Frebel 2010) measuring abundances on the atmosphere of stars, that reflect the metal enrichment of the ISM at the moment of birth, and therefore track the star-forming history of the ISM of the MW.

On the other hand, chemical abundances measured in the *gas phase* of a galaxy are a consequence of the integrated enrichment history until the present day, moreover, in this work the method used probes the ISM and the CGM of the Milky Way. Regardless both methods may be comparable and later this hypothesis will be tested.

Alpha elements include Ne, Mg, Si, S, Ar, Ca, Ti, and Fe-peak elements are Cr, Mn, Fe, Co, and Ni. At higher redshift for alpha enrichment in DLAs [α/Fe] Si or S are used as

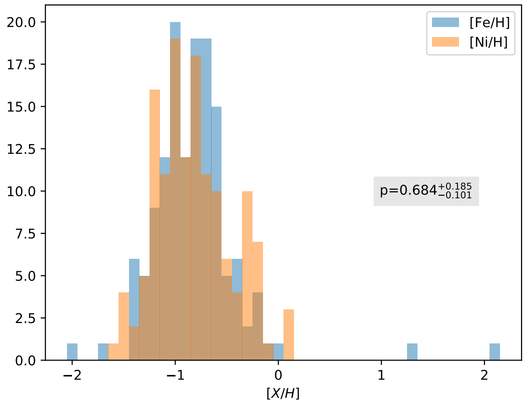

Figure 4.7: [Ni/H] and [Fe/H] abundances histogram in the sample, the box on the right shows the median p-value from the MC KS test, with the 75th and 25th percentile.

the tracer for the $\alpha-$elements and Fe as the tracer for the iron peak elements, to study this abundance ratio S is used to trace the $\alpha-$elements, and Ni to trace the Fe-peak elements because it is less susceptible to saturation compared to Fe.

In this work, to confirm that the relative abundances of Ni and Fe trace the same abundances a MC KS test yielded a mean $\sim 31\%$ confidence.

Figure 4.7 shows a histogram of both abundances. This suggests that [Ni/H] and [Fe/H] are likely drawn from the same parent distribution.

Finally, Figure 4.8 shows *gas-phase* [α/Fe] measurements from this thesis compared to the same relative abundances in the atmosphere of stars from the Halo, the thin and thick disk. It is clear to see from this figure that the mean [α/Fe] measured in this work is 0.5 dex higher than the plateau, and it does not align with any population of stars.

To test this a MC KS test rejects the null hypothesis of [α/Fe] in MW DLAs at 99.9% confidence when compared to any of the star populations. This confirms that both methods of measuring [α/Fe] are not comparable, a reason for this is that the abundances measured here could be affected by condensation to dust. Refractory elements like Fe and Ni easily condense into dust grains and lower the column density measured in the gas, which makes [α/Fe] to be overestimated.

The effects of dust depletion make it so that a comparable sample to the one presented here also has to use the same method. For this, the abundances measured in (de Cia et al. 2021) are used to compare to the [α/Fe] measured in the MW DLAs, Figure 4.9 shows this comparison. Dust depletion patterns in the MW vary around 1 dex (Konstantopoulou et al. 2022), and both (de Cia et al. 2021) abundances and the MW DLAs are affected by similar depletion patterns, thus both ratios are comparable.

From Figure 4.9 it is possible to see the decline of the [α/Fe] ratio with metallicity characteristic at higher metallicity than the *knee*. [Ni/H]~ -1.3 is the lowest metallicity probed by the MWDLAs, and the lower limits provided from de Cia et al. (2021) are not

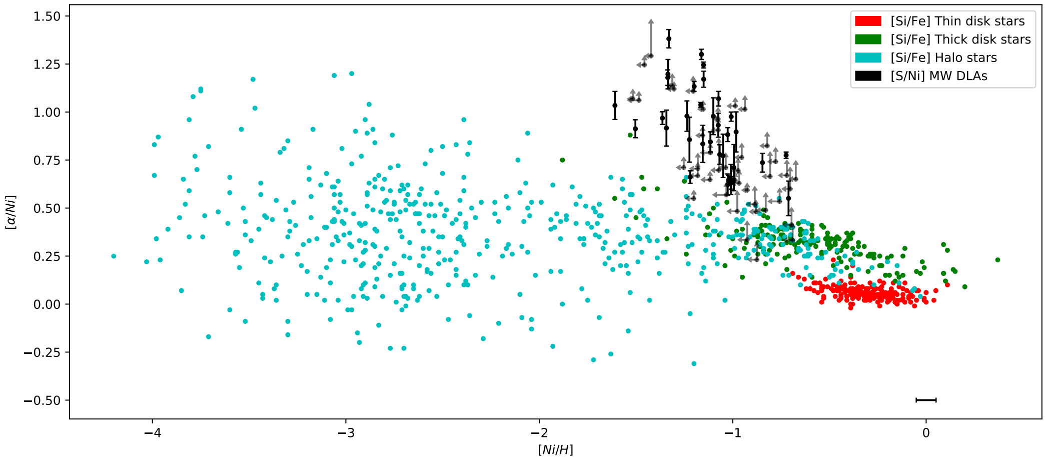

Figure 4.8: Relative abundance of [α/Fe]. Black dots circles are [α/Ni] measured from this work, colored circles were obtained from literature, and they show the metallicity of stars: in cyan are stars in the Halo from Frebel (2010); in green are stars found in the thick disk from Reddy et al. (2006), and in red stars found in the Thin disk from Reddy et al. (2003). In the lower right corner is the mean error in the [Ni/H] for the MW DLA sample.

sufficient to find a plateau. With this is possible to set an upper limit for the [α/Fe] *knee* at [Ni/Fe] ~ -1.6.

This upper limit on the metallicity of the *knee* is in agreement of the metallicity of the knee in the MW and the Sagitarius arm measured by de Boer et al. (2014), that measured the *knee* at [Fe/H]$= -1.27 \pm 0.05$

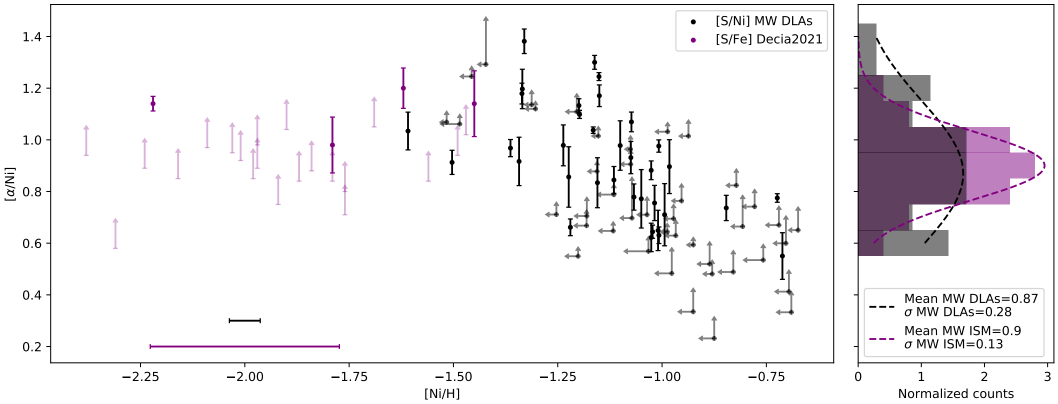

Figure 4.9: Relative abundance of [S/Ni]. Black dots are measured from the MW DLAs, purple points are measured by de Cia et al. (2021) on the ISM of the solar neighborhood. In the lower-left corner is the mean error in the [Ni/H] for the MW DLA sample and [Fe/H] for the (de Cia et al. 2021) sample.

Chapter 5

The Milky Way as a consequence of the DLA cosmic evolution history

In this section, I look into the metallicity scatter found in the MW and compare it to the scatter found in the cosmic metallicity history of DLAs. Secondly, I look into the [α/Fe] vs [Fe/H] relation in the MW compared to DLAs at high redshift to discuss what is the dominant type of galaxy in the high redshift selection of DLAs.

5.1 Metallicity evolution in cosmic time

The spatial distribution of metals in the MW studied in Chapter 4, uses multiple sightlines intercepting the MW's ISM and CGM through different directions. In this section, the abundances in the MW DLAs are compared with the same abundances measured using a compilation of DLAs from Berg et al. (2017) and Berg et al. (2017), consisting of DLAs in the redshift range $0 \lesssim z \lesssim 5$ to find a relation between the variation of metallicity seen in the MW and the cosmic metallicity variations seen at any redshift in DLAs.

The DLA sample from Berg et al. (2017) consists of the DLAs found on the spectra from the XQ-100 survey López et al. (2016) that observed 100 quasars at $3.5 \lesssim z_{qso} \lesssim 4.5$ with VLT/X-Shooter, while Berg et al. (2015) is a compilation of all publicly available DLAs published from 1994 to 2014 plus the observations presented there. The DLA sample from Rafelski et al. (2012) is included in Berg et al. (2015) sample and consists of a literature compilation of DLAs observed in spectra with $R > 5000$ and S/N > 15 pixel^{-1} that in general avoided samples with biases for metal-poor or metal-rich systems, except for the DLAs with $z < 1.5$ where DLAs are generally found by their strong metal lines, for more details on these see Rafelski et al. (2012). Berg et al. (2015) includes the DLAs that Rafelski et al. (2012) avoided and in this work, the larger sample was preferred because DLAs at $z < 1.5$ are relevant to this work. It is important to note that including DLAs at $z < 1.5$ introduces a possible bias in favor of metal-rich systems because DLAs in this range are identified by their strong metal lines.

z	z_{range}	[M/H]	$\sigma_{\mathrm{[M/H]}}$	Mean $\mathrm{error}_{\mathrm{[M/H]}}$
1.43	[0.01,2.16]	-0.81	0.48	0.13
2.52	[2.18,2.79]	-1.24	0.52	0.11
3.18	[2.8,3.61]	-1.26	0.47	0.13
4.11	[3.65,5.18]	-1.43	0.52	0.15

Table 5.1: Binned metallicity for high redshift DLAs.

Both Rafelski et al. (2012) and Berg et al. (2015) have significant overlap, and to account for this the combined sample was sorted with z and DLAs with a $\Delta z < 0.0001 \sim 30\,\mathrm{km/s}$ and Δ[M/H]< 0.0001 were considered to be the same DLA and taken out of the sample.

Proximate DLAs have a relative velocity separation from the background quasar $\Delta v < 3000\,\mathrm{km/s}$ and are in interaction with the QSO. Proximity to a QSO could invalidate the assumption of neutral gas in the DLA and lead to erroneous abundance determinations unless photoionization modeling is used (Ellison et al. 2010). Regardless, they were not removed from the sample, because their low numbers (5) would not affect the statistics of the sample. The combined DLA sample consists of 314 unique DLAs.

To measure the metallicity and scatter evolution in DLAs at high redshift the combined sample was binned into groups of similar redshift. I binned the combined sample into 3 bins of 79 and 1 bin of 77 systems for these groups to contain a similar number of systems as MW DLAs are found (79), to avoid any bias for any particularly metal-poor or metal-rich systems in the bins that could change the mean metallicity or increase the scatter significantly in a particular bin.

The H I weighted mean metallicity of the binned DLAs are calculated with Eq. 4.2

$$[M/H]_{total} = \sum_i \left(\frac{\sum_i [M/H]_i \times 10^{N(HI)_i}}{\sum_i 10^{N(HI)_i}} \right)$$

and reported in Table 5.1. In the same fashion, the HI weighted mean metallicity of MW DLAs, at $z = 0$, was calculated to be $[M/H]_{MW} = -0.4 \pm 0.2$ using S as the metalliciy tracer.

The top panel of Figure 5.1 shows the metallicity enrichment history of DLAs and the MW DLAs. A linear fit to these metallicity finds $[M/H](z) = (-0.22 \pm 0.06)z - (0.5 \pm 0.1)$. This linear fit is in agreement with similar models reported by Rafelski et al. (2014) ($[M/H](z) = (-0.20 \pm 0.03)z - (0.68 \pm 0.09)$). Extrapolating the linear fit to $z = 0$; we find a metallicity of -0.5 ± 0.1 which is consistent with the measured value of -0.4 ± 0.2 measured using the MW sightlines. This substantiates that the overall metallicity of the MW gas coincides with the expectation from DLA metallicity enrichment history, and not necessarily solar metallicity.

The binned metallicities (yellow stars) in Figure 5.1 show large error bars which in the x-axis represent the redshift range of the bin, and in the y-axis represent the standard deviation from the mean metallicity of the bin, not the overall uncertainty in the metallicities in the redshift bin. The typical standard deviation in the literature DLA is $\sigma_{DLA} \approx 0.5$, while for the MW: $\sigma_{MW} = 0.2$, this represents 40% of the standard deviation at any redshift bin. The standard deviation (0.5; which measures the scatter of DLAs within a redshift bin) is much larger than the uncertainties in each measurement of metallicity (0.1) and thus dominates the error in the metallicity evolution. Thus there must be an underlying reason for this large scatter at all redshifts and also in the MW. The scatter in metallicity can have different origins:

- **Variations in a galaxy stellar mass lead to variations in metallicity.** The metallicity of a galaxy is characterized by its mass, following the mass-metallicity relation (MZR), which physical origin is often attributed to the higher capability of massive galaxies to retain metals against the action of galactic outflows, in comparison to less massive galaxies. Although Baker and Maiolino (2023) argues that the stellar mass of the galaxy is more important than dynamical mass or halo mass because ultimately it is the stars that enrich the gas of a galaxy.
- **CGM and ISM metallicities are not homogeneously distributed.** The CGM plays a pivotal role in star formation regulation, because there flows pristine gas from the IGM into the ISM, and enriched gas flows out from stellar or Quasar feedback processes. These enriched gas outflows are concentrated near the minor axis of galaxies Péroux et al. (2020), thus metallicity in the CGM is expected to be higher at high-azimuthal angle. This is relevant to DLAs, because their relative orientation from their galaxy host is randomly probed by QSOs.
- **Different components of the galaxy ISM or CGM have different metallicities.** The different gas structures present in the CGM of the MW like satellite galaxies or High Velocity Clouds (HVCs) add to the in-homogeneity of metallicity. This is most likely what is probed by QSOs in galaxies at high redshift, and the metal abundances measured with spectroscopy include the metals from these structures.

Esteban et al. (2022) discusses in detail the possible origin for the variation in the metallicity measured in neutral gas in the local ISM by de Cia et al. (2021) - metallicities that this works agrees with - and metallicity measured in H II regions and in the atmosphere of young stars. In Esteban's paper, the main conclusion is that the gas in the ISM of the MW is well mixed, and metallicity variations cannot be explained as pockets of low metallicity that were accreted and survived the accretion without mixing with the rest of the gas. According to Esteban et al. (2022), this means that either the metallicities from de Cia et al. (2021) are wrong, or they do not account correctly for dust depletion.

The metallicities measured in this work could be lightly affected by dust depletion, but that would affect all metallicities in a similar magnitude and move the mean metallicity up, and does not explain the variations from one sightline to another. I argue that the main driving factor for the large scatter in metallicity in the MW DLAs here is due to the QSO sightlines probing the CGM and ISM simultaneously and that in this case, contrary to de Cia et al. (2021), the low metallicity pockets of gas present in the CGM from pristine infalling gas is affecting the total metallicity towards that sightline.

Going back to DLAs, if all DLAs were MW-like with the same stellar mass, same feedback processes, and QSO probed only one impact parameter, then the scatter in Figure 5.1 would be the same as found in the MW, 40% of its present value, and that the rest of parameters affect the variations with the other 60%.

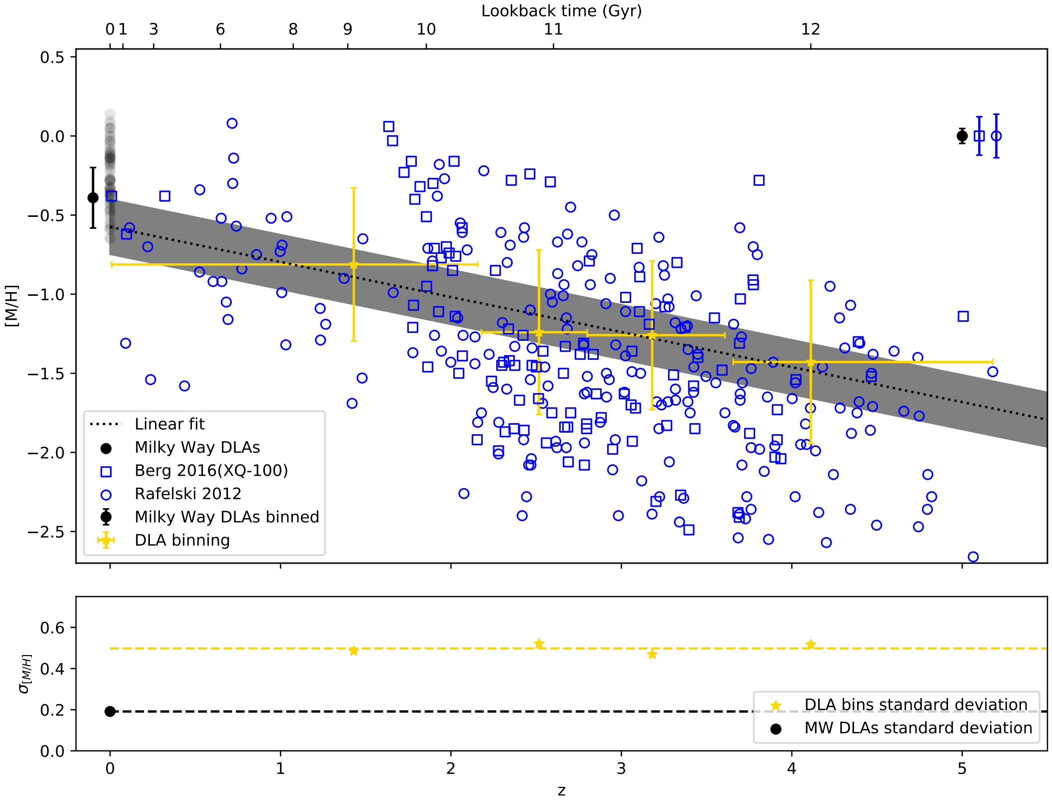

Figure 5.1: *Top.* $[M/H]$ as a function of redshift. Black circles at $z = 0$ show the metallicity in the MW DLAs, Blue points are from the literature DLA compilation, squares are from Berg et al. (2016), and circles are from Rafelski et al. (2012). The black point next to the MW DLAs is the binned metallicity with a $1 - \sigma$ standard deviation. The yellow stars show the H I weighted mean metallicity of DLA bins described in Table 5.1. The dotted black line is a fit to the binned metallicities, and the black region around it shows a $1 - \sigma$ uncertainty for this linear fit. In the lower right corner is the mean uncertainty in [M/H] for the samples plotted using the same marker and color as before.
Bottom. $\sigma_{[M/H]}$ as a function of redshift. The standard deviation of the MW DLAs at $z = 0$ is shown in a black point, and the standard deviation in metallicity measured in each redshift bin is shown in yellow stars. The yellow dashed line represents the mean standard deviation across DLA bins. The black dashed line represents the standard deviation in the MW DLAs.

5.2 Alpha elements in the MW and DLAs

We now turn our attention to [α/Fe] in DLAs compared to the MW DLAs to explore the eventual differences between them.

The identification of the host responsible for a DLA is difficult, due to the often small angular separation and their low surface brightness relative to the background QSO. Today only 115 galaxies at redshifts 0¡z¡4.4 are believed to be associated with DLA/sub-DLA absorbers (either as the primary absorbing galaxies or as members of the same group of galaxies) (Kulkarni et al. 2022).

At $z < 1$ where it is more likely to resolve the galaxy host imaging studies as well as IFU observations have studied the galaxies associated with DLAs (Rao et al. 2003). These studies suggest that dwarf galaxies are the dominant population among DLA hosts (Kulkarni et al. 2022).

Cooke et al. (2015) studies the chemical evolution and kinematic properties of the most metal-poor DLAs at $2 \lesssim z \lesssim 3$, where they find that DLAs [α/Fe] vs [Fe/H] is statistically different than what can be seen in MW halo stars, but is broadly similar to what can be seen on dwarf galaxies in the Local Group (Tolstoy et al. 2009).

Figure 5.2 shows a comparison of [α/Fe] in the MW DLAs to DLAs from the combined sample, with a histogram of [α/Fe] for both populations.

It is clear to see that [α/Fe] in the MW DLA sample is different from the literature sample as confirmed by an MCMC KS-test which says that the samples are not drawn from the same parent distribution beyond a $< 1\%$ confidence level. An important feature to be seen here is that the mean [α/Fe] in the literature DLAs is ~ 0.5 dex lower than the mean for the MW DLAs and that both samples have similar standard deviations. This is to be expected following the results of Cooke et al. (2015), while here the comparison is more direct because both column densities are measured in the neutral gas rather than using the abundances from Halo stars.

It is important to note that since Fe and Ni are not volatile, both elements –and thus [α/Fe] as well– are affected by dust depletion. For DLAs in the literature, it is difficult to make dust corrections, because most studies do not cover the elements necessary to do so. This is also true for the [α/Fe] measured in this work. To correct for dust depletion the ratio of the iron-peak elements [Zn/Fe] is very useful (De Cia et al. 2016; Konstantopoulou et al. 2024), also Guber and Richter (2016) suggests that the [Ti/Ca] ratio represents a useful measure for the gas-to-dust ratio and overall metallicity in intervening absorption-line systems.

These differences in the mean [α/Fe] between the MW DLAs and DLAs are either explained by: (i) both the MW DLAs and DLAs populations are being affected by dust depletion in different magnitudes, which does not explain why both samples have similar standard deviation in [α/Fe] and cannot be demonstrated without more observations and a careful study of each DLA in the sample and the MWDLAs (Berg et al. 2015); or (ii) assuming that both the DLA sample and MWDLAs are affected by dust depletion in the same order of

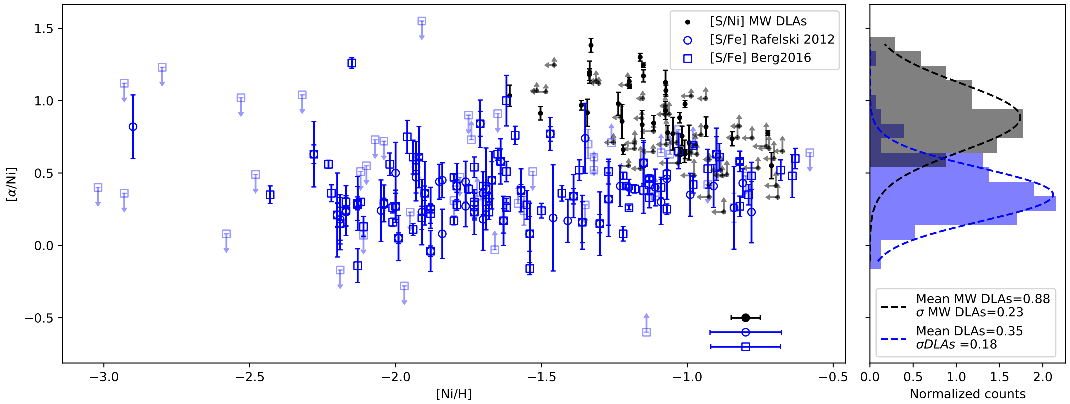

Figure 5.2: *Left* Relative abundance of [S/Ni] in DLAs and the MW (present work). Black dots are measured from MW DLAs, blue empty circles are measured by Berg et al. (2016) on DLA halos, and blue empty squares are from Rafelski et al. (2012). In the upper right corner is the mean error in the [Ni/H] or [Fe/H] for samples plotted in using the same marker and color as before.
Right Histogram of the frequencies for [α/Fe], with a corresponding Gaussian profile characterizing the histogram.

magnitude, which supports that this difference of ~ 0.5 dex in mean [α/Fe] is statistically relevant and differentiate both samples.

Moreover Cooke et al. (2015) studying the most metal-poor DLAs, at $z \sim 2-3$ and Berg et al. (2015) studying the most metal-rich DLAs, at $z \sim 2$, both find evidence that [α/Fe] of DLAs are not representative of galaxies similar to those that merged to form the bulk of the MW. Berg et al. (2015) finds that [α/Fe] of DLAs is consistent at ≈ 0.5 at the metallicity of the MW's α *knee*, but they use [Zn/H] as their metallicty tracer –instead of [Ni/H] used here– element which doesn't necessarily follow the same nucleosynthetic origin as Fe, and is not clear they can be used for this at metallicities higher than -1.0, thus they cannot conclude about a drop of [α/Fe] below the knee.

The MWDLAs bring a more direct point of comparison when studying [α/Fe] in MW-like galaxies because the ratios measured are affected by the same assumptions on dust depletion and both measure chemical abundances in the neutral gas of a galaxy, contrary to previous studies that used abundances from MW's halo stars. This more direct comparison allows us to also conclude that the population of DLAs is more likely dominated by dwarf galaxies.

Chapter 6

Summary

The goal of this section is to summarize the conclusions from the discussion on Chapter 4 and 5, and relate them to the goals of this thesis:

1. **What is the metal content of the Milky Way's gas?**
2. **Is it possible to find the distribution of metals with this method?**
3. **What can the metallicity variations in the MW tell us about the cosmic metallicity evolution of DLAs?**

6.1 Metallicity of the MW and possible gradients

The method of measuring column densities used here is robust and probes the neutral gas reservoirs of the MW. Column densities for volatile elements like Ni or Fe are, however, possibly affected by dust depletion, and given that at $z = 0$ there is no coverage of the elements necessary to do dust correction, (Ti II as suggested by Guber and Richter (2016) and Berg et al. (2016), or Zn II as suggested by Konstantopoulou et al. (2022) and De Cia et al. (2016)) then it is not possible to correct for dust depletion. To ensure that the metallicities measured here are robust, the refractory element S was used as a metallicity tracer. With this, it is possible to conclude that:

- The measured metallicities in the MW DLAs are mostly sub-solar (Figure 4.4), with a mean metallicity $[M/H]=-0.4+\pm0.2$, which is a larger than the average uncertainty (0.7 dex) of the measurements.
- There is no trend of metallicity with galactic latitude, but there is a region at $\sim -40°$ with lower average metallicity (Figure 4.4), and this is most likely due to the presence of the Magellanic Stream, the largest known inflow of low metallicity gas of the MW (Richter et al. 2017).
- There is, however, a trend of increasing column density of H I with decreasing galactic latitude as expected from 21-cm radio emission maps (Figure 4.1 and 4.3). To compare

the robustness of the column density measurements of H I I compare them to column density from the 21-cm radio emission map from (HI4PI Collaboration et al. 2016). From this comparison, it is possible to see that both methods and results agree within 20% of each other 75% of the time (Figure 4.2).

- [α/Fe] in the MW DLAs shows a large difference compared to the same relative abundances measured in the atmosphere of stars in the MW as seen in Figure 4.8, but agrees with [α/Fe] measured in the local ISM by (de Cia et al. 2021) as seen in Figure 4.9. This is most likely due to the abundances in the ISM(+CGM) being affected by dust depletion while abundances measured from the atmosphere of stars are not. There are, however, not enough points at low [Fe/H] to estimate the position of the [α/Fe] knee, and it is only possible to say that the knee is at [Fe/H] < -1.3.

In the context of the enrichment history of the neutral gas in the universe, DLAs play a major role, because they are the main neutral gas reservoirs in the Universe, more than 70% of the total density cosmic H I density (Noterdaeme et al. 2007). In this thesis 79 sightlines have $\log N(\text{H I}) > 2 \times 10^{20}$, and so these systems are treated as DLAs at $z = 0$. The metallicities measured in these MW DLAs were compared to a compilation of DLAs from (Berg et al. 2016) and (Rafelski et al. 2012) to see how the MW fits into this history and confirm if it is possible to consider the MW as a DLA.

From this thesis, I conclude:

- A linear fit to the cosmic metallicity history of DLAs reports $[\text{M/H}](z) = (-0.22 \pm 0.06) \times z - (0.5 \pm 0.1)$ and extrapolating the linear fit to $z = 0$; we find a metallicity of -0.5 ± 0.1 which is consistent with the measured value of -0.4 ± 0.2 measured using the MW DLA sightlines. (Figure 5.1 upper panel).
- The standard deviation in the DLAs bins is constant with redshift at 0.5 dex, while the standard deviation in the MW DLAs is 0.2 dex, corresponding to 40% of the standard deviation in DLAs (Figure 5.1, lower panel). This discrepancy likely originates from the larger range of galaxy host masses, stellar masses in the galaxy host, impact parameter, and azimuthal angle probed by DLAs in a singular redshift bin, while in the MW most of these quantities are fixed.

  From these discrepancies, it is possible to say that if all DLAs' hosts at high redshift were MW-like, then the standard deviation would be 40% of the present value.
- $[\alpha/Fe]$ of the MW DLAs is 0.5 dex higher than what is seen in DLAs (Figure 5.2), and assuming both samples are affected by dust depletion with the same order of magnitude, then this difference is significant enough to say that DLAs show $[\alpha/Fe]$ patterns closer related to dwarf galaxies, rather than MW-like, as supported by the work of Cooke et al. (2015) and Berg et al. (2015).

Chapter 7

Future work

To advance this work further it would be useful to:

- Use the chemical abundances measured here to model the ionization correction of the MW sub-DLAs, in order to use all chemical abundances measured in this work. Possibly using an approach like Berg et al. (2021).
- Find complementary datasets for the same QSO in order to get column densities of key elements to study the effects of dust depletion. We could benefit of works that studied the dust depletion patterns in the MW such as Konstantopoulou et al. (2022), Konstantopoulou et al. (2024), and De Cia et al. (2016).
- The 4MOST–Gaia Purely Astrometric Quasar Survey (4G-PAQS) will carry out the first large-scale, colour-independent quasar survey selected solely on the basis of astrometry from Gaia (Krogager et al. 2023). This survey will provide us with a larger dataset of spectra that can be used to perform this same study on a larger sample of QSO spectra, unbiased by color selection.

Bibliography

Arellano-Córdova, K. Z. et al. (Aug. 2020). “The Galactic radial abundance gradients of C, N, O, Ne, S, Cl, and Ar from deep spectra of H II regions”. In: 496.2, pp. 1051–1076. DOI: 10.1093/mnras/staa1523. arXiv: 2005.11372 [astro-ph.GA].

— (Mar. 2021). “On the radial abundance gradients of nitrogen and oxygen in the inner Galactic disc”. In: 502.1, pp. 225–241. DOI: 10.1093/mnras/staa3903. arXiv: 2012.06643 [astro-ph.GA].

Asplund, Martin et al. (Sept. 2009). “The Chemical Composition of the Sun”. In: 47.1, pp. 481–522. DOI: 10.1146/annurev.astro.46.060407.145222. arXiv: 0909.0948 [astro-ph.SR].

Baker, William M. and Roberto Maiolino (May 2023). “Stellar mass, not dynamical mass nor gravitational potential, drives the mass-metallicity relationship”. In: 521.3, pp. 4173–4179. DOI: 10.1093/mnras/stad802. arXiv: 2303.08145 [astro-ph.GA].

Berg, T. A. M. et al. (Dec. 2016). “Chemical abundances of the damped Lyman α systems in the XQ-100 survey”. In: 463.3, pp. 3021–3037. DOI: 10.1093/mnras/stw2232. arXiv: 1609.05968 [astro-ph.GA].

Berg, T. A. M. et al. (Jan. 2017). “On the selection of damped Lyman α systems using Mg II absorption at 2 ¡ z_{abs} ¡ 4”. In: 464.1, pp. L56–L60. DOI: 10.1093/mnrasl/slw185. arXiv: 1609.09081 [astro-ph.GA].

Berg, Trystyn A. M. et al. (Oct. 2015). “The chemistry of the most metal-rich damped Lyman α systems at z $\sim$ 2 - II. Context with the Local Group”. In: 452.4, pp. 4326–4346. DOI: 10.1093/mnras/stv1577. arXiv: 1507.08311 [astro-ph.GA].

Berg, Trystyn A. M. et al. (Apr. 2021). “Sub-damped Lyman α systems in the XQ-100 survey - II. Chemical evolution at 2.4 $\leq$ z $\leq$ 4.3”. In: 502.3, pp. 4009–4025. DOI: 10.1093/mnras/stab184. arXiv: 2101.07821 [astro-ph.GA].

Bethe, H. A. (Mar. 1939). “Energy Production in Stars”. In: *Phys. Rev.* 55 (5), pp. 434–456. DOI: 10.1103/PhysRev.55.434. URL: https://link.aps.org/doi/10.1103/PhysRev.55.434.

Binney, James and Scott Tremaine (2008). *Galactic Dynamics: Second Edition*.

Bland-Hawthorn, Joss and Ortwin Gerhard (Sept. 2016). “The Galaxy in Context: Structural, Kinematic, and Integrated Properties”. In: 54, pp. 529–596. DOI: 10.1146/annurev-astro-081915-023441. arXiv: 1602.07702 [astro-ph.GA].

Carswell, R. F. and J. K. Webb (Aug. 2014). *VPFIT: Voigt profile fitting program*. Astrophysics Source Code Library, record ascl:1408.015. ascl: 1408.015.

Chen, Hsiao-Wen and Kenneth M. Lanzetta (Nov. 2003). “The Nature of Damped Lyα Absorbing Galaxies at z ¡= 1: A Photometric Redshift Survey of Damped Lyα Absorbers”. In: 597.2, pp. 706–729. DOI: 10.1086/378635. arXiv: astro-ph/0308190 [astro-ph].

Chromey, Frederick R. (2010). *To measure the sky : an introduction to observational astronomy*. First. Cambridge University Press, p. 446. ISBN: 9780521747684.

Cooke, R. (July 2013). “A New Software Package for Measuring Fundamental Constant VariationÂ”. In: *Varying Fundamental Constants and Dynamical Dark Energy*, 11, p. 11.

Cooke, Ryan J. et al. (Feb. 2015). “The Most Metal-poor Damped Lyα Systems: An Insight into Dwarf Galaxies at High-redshift”. In: 800.1, 12, p. 12. DOI: `10.1088/0004-637X/800/1/12`. arXiv: `1406.7003 [astro-ph.GA]`.

de Boer, T. J. L. et al. (Sept. 2014). “The α-element knee of the Sagittarius stream”. In: 443.1, pp. 658–663. DOI: `10.1093/mnras/stu1176`. arXiv: `1406.3352 [astro-ph.GA]`.

De Cia, A. et al. (Dec. 2016). “Dust-depletion sequences in damped Lyman-α absorbers. A unified picture from low-metallicity systems to the Galaxy”. In: 596, A97, A97. DOI: `10.1051/0004-6361/201527895`. arXiv: `1608.08621 [astro-ph.GA]`.

de Cia, A. et al. (Sept. 2021). “Large metallicity variations in the Galactic interstellar medium”. In: *Nature* 597, pp. 206–208. ISSN: 14764687. DOI: `10.1038/s41586-021-03780-0`. URL: `https://ui.adsabs.harvard.edu/abs/2021Natur.597..206D/abstract`.

Delhaye, J. (1965). “Solar Motion and Velocity Distribution of Common Stars”. In: *Galactic structure. Edited by Adriaan Blaauw and Maarten Schmidt. Published by the University of Chicago Press*. Ed. by Adriaan Blaauw and Maarten Schmidt, p. 61.

Draine, Bruce T. (2011). *Physics of the Interstellar and Intergalactic Medium*.

Ellison, Sara L. et al. (Aug. 2010). “The nature of proximate damped Lyman α systems”. In: 406.3, pp. 1435–1459. DOI: `10.1111/j.1365-2966.2010.16780.x`. arXiv: `1004.2715 [astro-ph.CO]`.

Esteban, C. et al. (June 2022). “About Metallicity Variations in the Local Galactic Interstellar Medium”. In: 931.2, 92, p. 92. DOI: `10.3847/1538-4357/ac6b38`. arXiv: `2204.12258 [astro-ph.GA]`.

Faucher-Giguère, Claude-André and S. Peng Oh (2023). “Key Physical Processes in the Circumgalactic Medium”. In: *Annual Review of Astronomy and Astrophysics* 61.1, pp. 131–195. DOI: `10.1146/annurev-astro-052920-125203`. eprint: `https://doi.org/10.1146/annurev-astro-052920-125203`. URL: `https://doi.org/10.1146/annurev-astro-052920-125203`.

Fox, Andrew and Romeel Davé (2017). *Gas Accretion onto Galaxies*. ISBN: 978-3-319-52511-2. DOI: `10.1007/978-3-319-52512-9`. URL: `http://www.springer.com/series/5664`.

Frebel, A. (May 2010). “Stellar archaeology: Exploring the Universe with metal-poor stars”. In: *Astronomische Nachrichten* 331.5, pp. 474–488. DOI: `10.1002/asna.201011362`. arXiv: `1006.2419 [astro-ph.GA]`.

Gamow, G. (1952). *The Birth and Death of the Sun*. Mentor. ISBN: 9780451600776. URL: `https://books.google.cl/books?id=KYEgAQAAIAAJ`.

Guber, C. R. and P. Richter (June 2016). “Dust depletion of Ca and Ti in QSO absorption-line systems”. In: *Astronomy amp; Astrophysics* 591, A137. ISSN: 1432-0746. DOI: `10.1051/0004-6361/201628466`. URL: `http://dx.doi.org/10.1051/0004-6361/201628466`.

Hansen, Carl J. et al. (2004). *Stellar interiors : physical principles, structure, and evolution*.

HI4PI Collaboration et al. (Oct. 2016). “HI4PI: A full-sky H I survey based on EBHIS and GASS”. In: 594, A116, A116. DOI: `10.1051/0004-6361/201629178`. arXiv: `1610.06175 [astro-ph.GA]`.

Khare, P. et al. (Mar. 2007). “The nature of damped Lyman α and sub-damped Lyman α absorbers”. In: 464.2, pp. 487–493. DOI: 10.1051/0004-6361:20066186. arXiv: astro-ph/0608127 [astro-ph].

Konstantopoulou, Christina et al. (Oct. 2022). “Dust depletion of metals from local to distant galaxies. I. Peculiar nucleosynthesis effects and grain growth in the ISM”. In: 666, A12, A12. DOI: 10.1051/0004-6361/202243994. arXiv: 2207.08804 [astro-ph.GA].

Konstantopoulou, Christina et al. (Jan. 2024). “Dust depletion of metals from local to distant galaxies. II. Cosmic dust-to-metal ratio and dust composition”. In: 681, A64, A64. DOI: 10.1051/0004-6361/202347171. arXiv: 2310.07709 [astro-ph.GA].

Krogager, J. -K. et al. (Mar. 2015). “The High A_V Quasar Survey: Reddened Quasi-Stellar Objects Selected from Optical/Near-Infrared Photometry—II”. In: 217.1, 5, p. 5. DOI: 10.1088/0067-0049/217/1/5. arXiv: 1410.7783 [astro-ph.GA].

Krogager, J. -K. et al. (Mar. 2023). “The 4MOST–Gaia Purely Astrometric Quasar Survey (4G-PAQS)”. In: *The Messenger* 190, pp. 38–41. DOI: 10.18727/0722-6691/5310.

Kulkarni, Varsha P. et al. (Apr. 2022). “Damped Lyα Absorbers in Star-forming Galaxies at z ¡ 0.15 Detected with the Hubble Space Telescope and Implications for Galactic Evolution”. In: 929.2, 150, p. 150. DOI: 10.3847/1538-4357/ac5fab. arXiv: 2112.00870 [astro-ph.GA].

Lehner, Nicolas et al. (Sept. 2020). “Project AMIGA: The Circumgalactic Medium of Andromeda”. In: 900.1, 9, p. 9. DOI: 10.3847/1538-4357/aba49c. arXiv: 2002.07818 [astro-ph.GA].

Lide, David R. (2008). *CRC Handbook of chemistry and physics: a ready-reference book of chemical and physical data.*

López, S. et al. (Oct. 2016). “XQ-100: A legacy survey of one hundred $3.5 \lesssim z \lesssim 4.5$ quasars observed with VLT/X-shooter”. In: 594, A91, A91. DOI: 10.1051/0004-6361/201628161. arXiv: 1607.08776 [astro-ph.GA].

Maeda, Keiichi (Nov. 2022). “Stellar Evolution, SN Explosion, and Nucleosynthesis”. In: *Handbook of X-ray and Gamma-ray Astrophysics*. Springer Nature Singapore, pp. 1–41. ISBN: 9789811645440. DOI: 10.1007/978-981-16-4544-0_85-1. URL: http://dx.doi.org/10.1007/978-981-16-4544-0_85-1.

McWilliam, Andrew (Jan. 1997). “Abundance Ratios and Galactic Chemical Evolution”. In: 35, pp. 503–556. DOI: 10.1146/annurev.astro.35.1.503.

Morton, Donald C. (Oct. 2000). “Atomic Data for Resonance Absorption Lines. II. Wavelengths Longward of the Lyman Limit for Heavy Elements”. In: 130.2, pp. 403–436. DOI: 10.1086/317349.

— (Nov. 2003). “Atomic Data for Resonance Absorption Lines. III. Wavelengths Longward of the Lyman Limit for the Elements Hydrogen to Gallium”. In: 149.1, pp. 205–238. DOI: 10.1086/377639.

Mowlavï, N. (1999). “Dredge-up in asymptotic giant branch stars”. In: *Symposium - International Astronomical Union* 191, pp. 47–52. DOI: 10.1017/s0074180900202878.

Noterdaeme, P. et al. (Nov. 2007). “Excitation mechanisms in newly discovered H_2-bearing damped Lyman-α clouds: systems with low molecular fractions”. In: 474.2, pp. 393–407. DOI: 10.1051/0004-6361:20078021. arXiv: 0707.4479 [astro-ph].

Noterdaeme, P. et al. (Oct. 2009). “Evolution of the cosmological mass density of neutral gas from Sloan Digital Sky Survey II - Data Release 7”. In: 505.3, pp. 1087–1098. DOI: 10.1051/0004-6361/200912768. arXiv: 0908.1574 [astro-ph.CO].

Padovani, P. et al. (Aug. 2017). "Active galactic nuclei: what's in a name?" In: *The Astronomy and Astrophysics Review* 25.1. ISSN: 1432-0754. DOI: `10.1007/s00159-017-0102-9`. URL: `http://dx.doi.org/10.1007/s00159-017-0102-9`.

Peeples, M. et al. (Apr. 2017). *The Hubble Spectroscopic Legacy Archive*. Instrument Science Report COS 2017-4, 8 pages.

Péroux, Céline et al. (Dec. 2020). "Predictions for the angular dependence of gas mass flow rate and metallicity in the circumgalactic medium". In: 499.2, pp. 2462–2473. DOI: `10.1093/mnras/staa2888`. arXiv: `2009.07809 [astro-ph.GA]`.

Pettini, Max et al. (May 1994). "Metal Enrichment, Dust, and Star Formation in Galaxies at High Redshifts. III. Zn and CR Abundances for 17 Damped Lyman-Alpha Systems". In: 426, p. 79. DOI: `10.1086/174041`.

Pontzen, Andrew and Max Pettini (Feb. 2009). "Dust biasing of damped Lyman alpha systems: a Bayesian analysis". In: 393.2, pp. 557–568. DOI: `10.1111/j.1365-2966.2008.14193.x`. arXiv: `0810.3236 [astro-ph]`.

Prochaska, J. Xavier and Arthur M. Wolfe (May 2009a). "On the (Non)Evolution of H I Gas in Galaxies Over Cosmic Time". In: 696.2, pp. 1543–1547. DOI: `10.1088/0004-637X/696/2/1543`. arXiv: `0811.2003 [astro-ph]`.

— (May 2009b). "On the (Non)Evolution of H I Gas in Galaxies Over Cosmic Time". In: 696.2, pp. 1543–1547. DOI: `10.1088/0004-637X/696/2/1543`. arXiv: `0811.2003 [astro-ph]`.

Prochaska, J. Xavier et al. (Nov. 2016). *linetools/linetools: Second major release*. Version v0.2. DOI: `10.5281/zenodo.168270`. URL: `https://doi.org/10.5281/zenodo.168270`.

Quiret, S. et al. (June 2016). "The ESO UVES advanced data products quasar sample - VI. Sub-damped Lyman α metallicity measurements and the circumgalactic medium". In: 458.4, pp. 4074–4121. DOI: `10.1093/mnras/stw524`. arXiv: `1602.02564 [astro-ph.GA]`.

Rafelski, Marc et al. (Aug. 2012). "Metallicity Evolution of Damped Lyα Systems Out to z ~5". In: 755.2, 89, p. 89. DOI: `10.1088/0004-637X/755/2/89`. arXiv: `1205.5047 [astro-ph.CO]`.

Rafelski, Marc et al. (Feb. 2014). "The Rapid Decline in Metallicity of Damped Lyα Systems at z ~5". In: 782.2, L29, p. L29. DOI: `10.1088/2041-8205/782/2/L29`. arXiv: `1310.6042 [astro-ph.CO]`.

Rao, Sandhya M. et al. (Sept. 2003). "Low-Redshift Damped Lyα Galaxies toward the Quasars B2 0827+243, PKS 0952+179, PKS 1127-145, and PKS 1629+120". In: 595.1, pp. 94–108. DOI: `10.1086/377331`. arXiv: `astro-ph/0211297 [astro-ph]`.

Reddy, Bacham E. et al. (Mar. 2003). "The chemical compositions of Galactic disc F and G dwarfs". In: 340.1, pp. 304–340. DOI: `10.1046/j.1365-8711.2003.06305.x`. arXiv: `astro-ph/0211551 [astro-ph]`.

Reddy, Bacham E. et al. (Apr. 2006). "Elemental abundance survey of the Galactic thick disc". In: 367.4, pp. 1329–1366. DOI: `10.1111/j.1365-2966.2006.10148.x`. arXiv: `astro-ph/0512505 [astro-ph]`.

Richter, P. et al. (Nov. 2017). "An HST/COS legacy survey of high-velocity ultraviolet absorption in the Milky Way's circumgalactic medium and the Local Group". In: 607, A48, A48. DOI: `10.1051/0004-6361/201630081`. arXiv: `1611.07024 [astro-ph.GA]`.

Savage, Blair D and Kenneth R Sembach (1991). "THE ANALYSIS OF APPARENT OPTICAL DEPTH PROFILES FOR INTERSTELLAR ABSORPTION LINES". In: *The Astrophysical Journal* 379, pp. 245–259.

Soderblom, D. R. (2023). “COS Instrument Handbook v. 15.0”. In: *COS Instrument Handbook v. 15.0*. Vol. 15, p. 15.

Tinsley, B. M. (May 1979). “Stellar lifetimes and abundance ratios in chemical evolution.” In: 229, pp. 1046–1056. DOI: 10.1086/157039.

Tolstoy, Eline et al. (Sept. 2009). “Star-Formation Histories, Abundances, and Kinematics of Dwarf Galaxies in the Local Group”. In: 47.1, pp. 371–425. DOI: 10.1146/annurev-astro-082708-101650. arXiv: 0904.4505 [astro-ph.CO].

Tumlinson, Jason et al. (Aug. 2017). “The Circumgalactic Medium”. In: *Annual Review of Astronomy and Astrophysics* 55, pp. 389–432. ISSN: 00664146. DOI: 10.1146/annurev-astro-091916-055240.

Verner, D. A. et al. (Dec. 1994). “Atomic data for absorption lines from the ground level at wavelengths greater than 228A.” In: 108, pp. 287–340.

Verner, D. A. et al. (Jan. 1996). “Atomic Data for Permitted Resonance Lines of Atoms and Ions from H to Si, and S, Ar, Ca, and Fe”. In: *Atomic Data and Nuclear Data Tables* 64, p. 1. DOI: 10.1006/adnd.1996.0018. arXiv: atom-ph/9604003 [physics.atom-ph].

Wolfe, A. M. et al. (June 1986). “Damped Lyman-Alpha Absorption by Disk Galaxies with Large Redshifts. I. The Lick Survey”. In: 61, p. 249. DOI: 10.1086/191114.

Wolfe, Arthur M. et al. (Sept. 2005). “Damped Ly α Systems”. In: 43.1, pp. 861–918. DOI: 10.1146/annurev.astro.42.053102.133950. arXiv: astro-ph/0509481 [astro-ph].

Woosley, S. E. and Thomas A. Weaver (Nov. 1995). “The Evolution and Explosion of Massive Stars. II. Explosive Hydrodynamics and Nucleosynthesis”. In: 101, p. 181. DOI: 10.1086/192237.

Zheng, Y. et al. (Jan. 2019). “Revealing the Milky Way’s Hidden Circumgalactic Medium with the Cosmic Origins Spectrograph Quasar Database for Galactic Absorption Lines”. In: 871.1, 35, p. 35. DOI: 10.3847/1538-4357/aaf6eb. arXiv: 1710.10703 [astro-ph.GA].

Zwaan, M. A. et al. (Dec. 2005). “Reconciling the local galaxy population with damped Lyman α cross-sections and metal abundances”. In: 364.4, pp. 1467–1487. DOI: 10.1111/j.1365-2966.2005.09698.x. arXiv: astro-ph/0510127 [astro-ph].

Annex A

ALIS fits

Here are the ALIS fits for 5 systems, and just as Figure 3.6 the black line is the normalized spectra used to run the fit, the grey line is the normalized flux masked out, the dashed blue line is the continuum fitted by ALIS, the red line is the fit by ALIS, red vertical lines denote the velocity centroid of Milky Way lines, red crosses mark the velocity centroid of HVCs, blue vertical lines denote velocity centroid of blend lines, a blue star above a vertical line means a line from the MW from another species, the grey area shows 2σ contours, finally, the light blue line is the residuals. The contour and residuals are displaced lower and scaled down for better display. The zero velocity is at v_{LSR}.

The rest of the ALIS fits is in here. The files are named *XX_metal.pdf*, where *XX* is the HSLA ID of the Quasar.

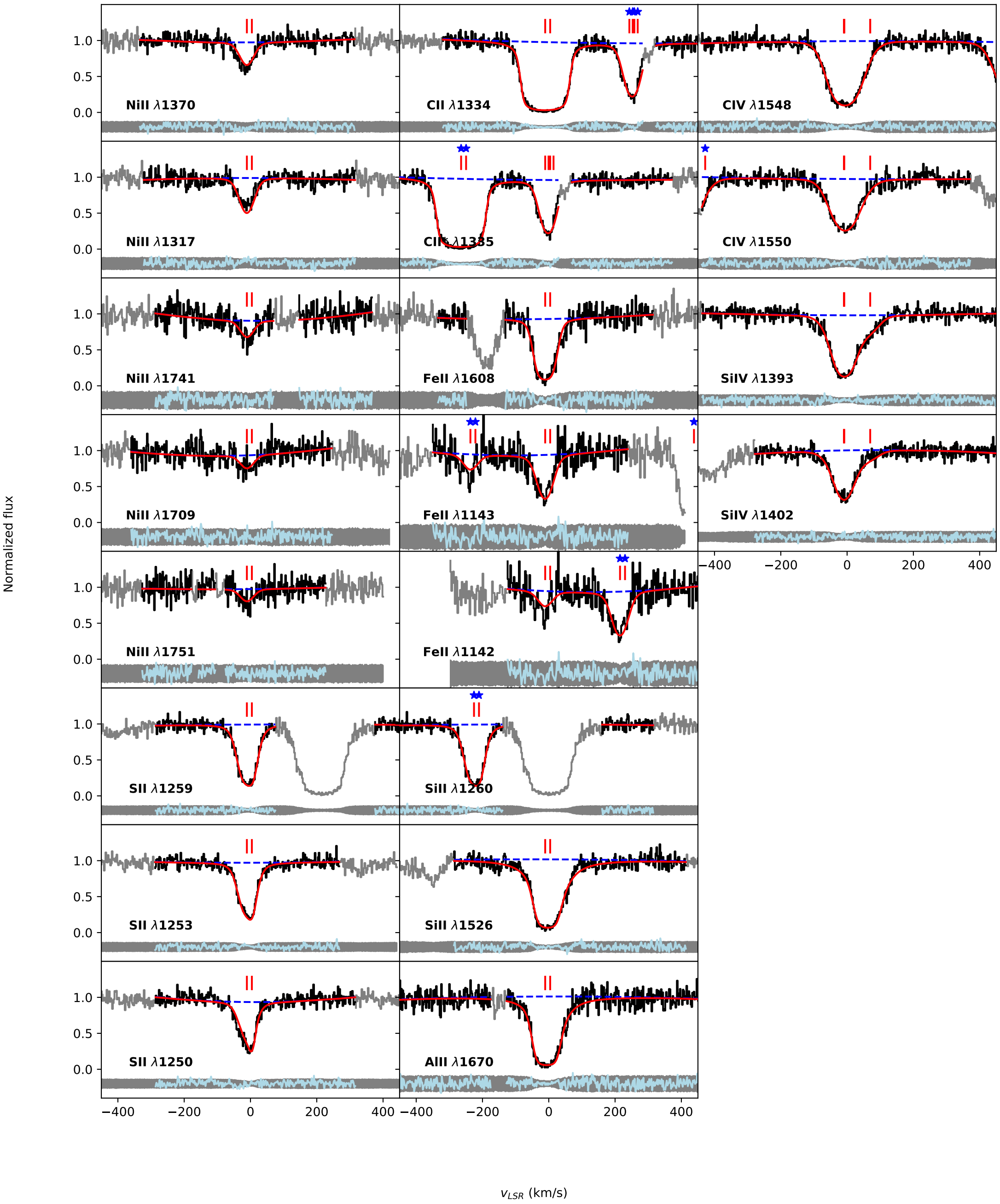

Figure A.1: ALIS fit of the MW absorption in sightline *1ES1553+113*.

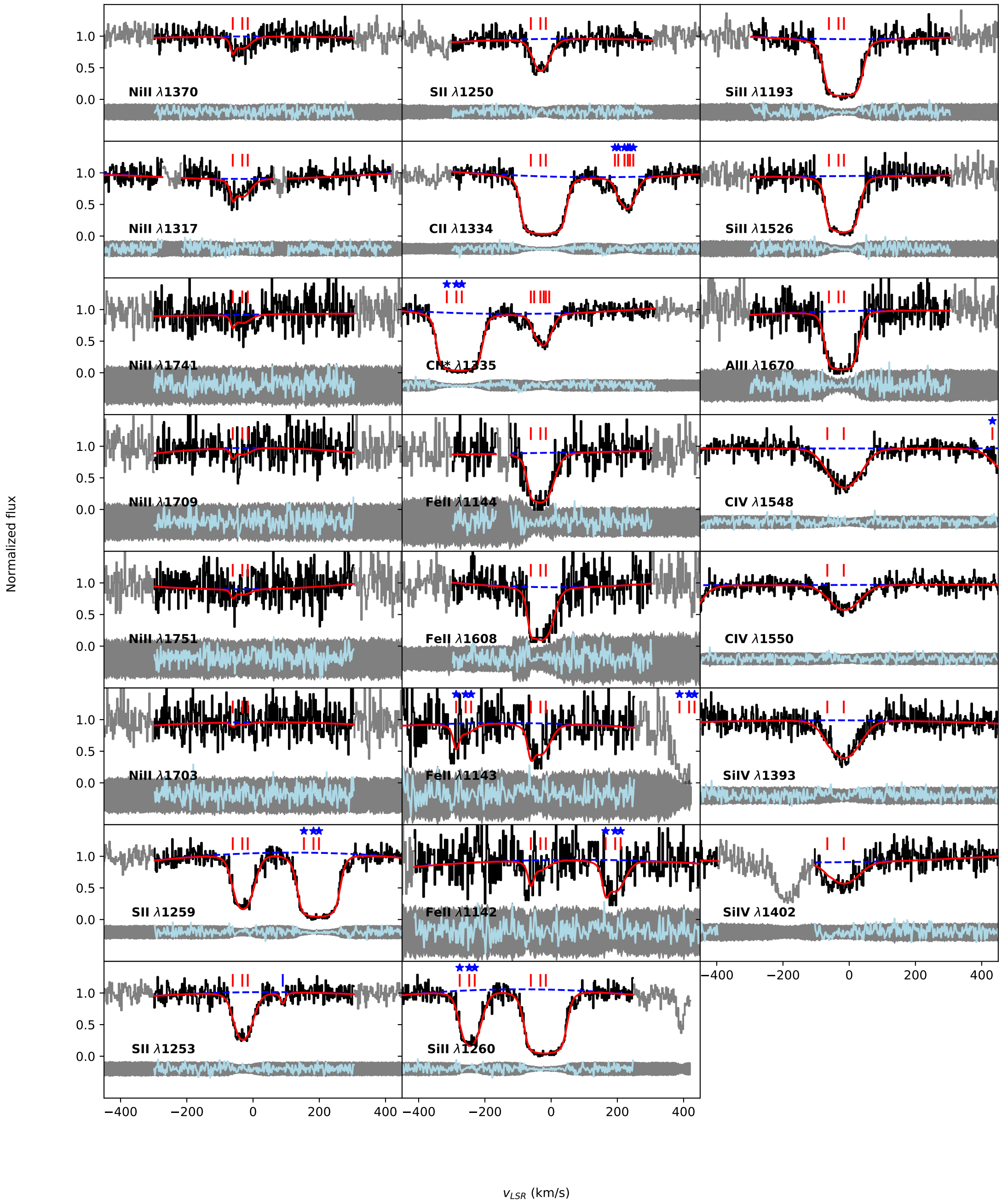

Figure A.2: ALIS fit of the MW absorption in sightline *TON580*.

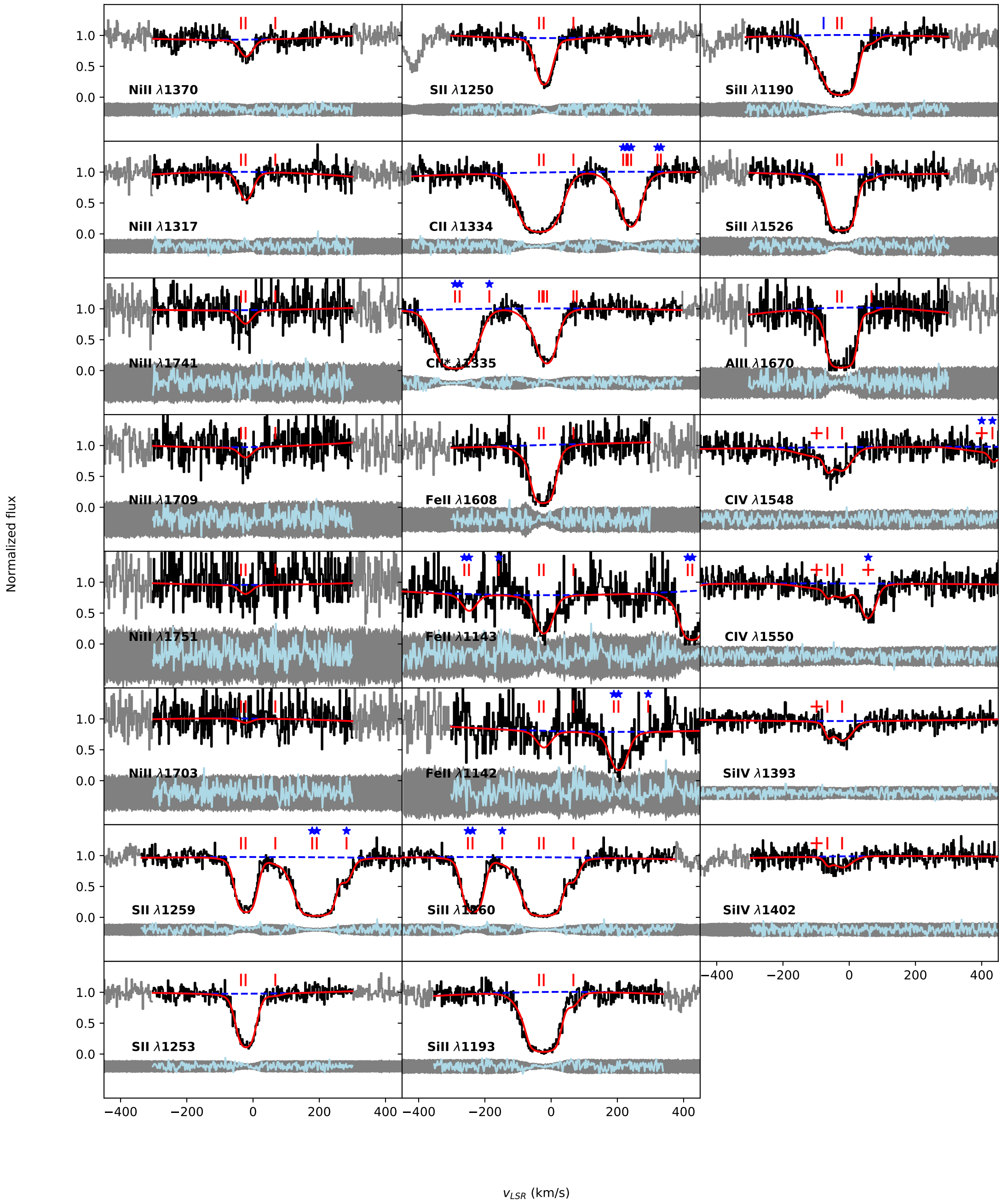

Figure A.3: ALIS fit of the MW absorption in sightline *3C-66A*.

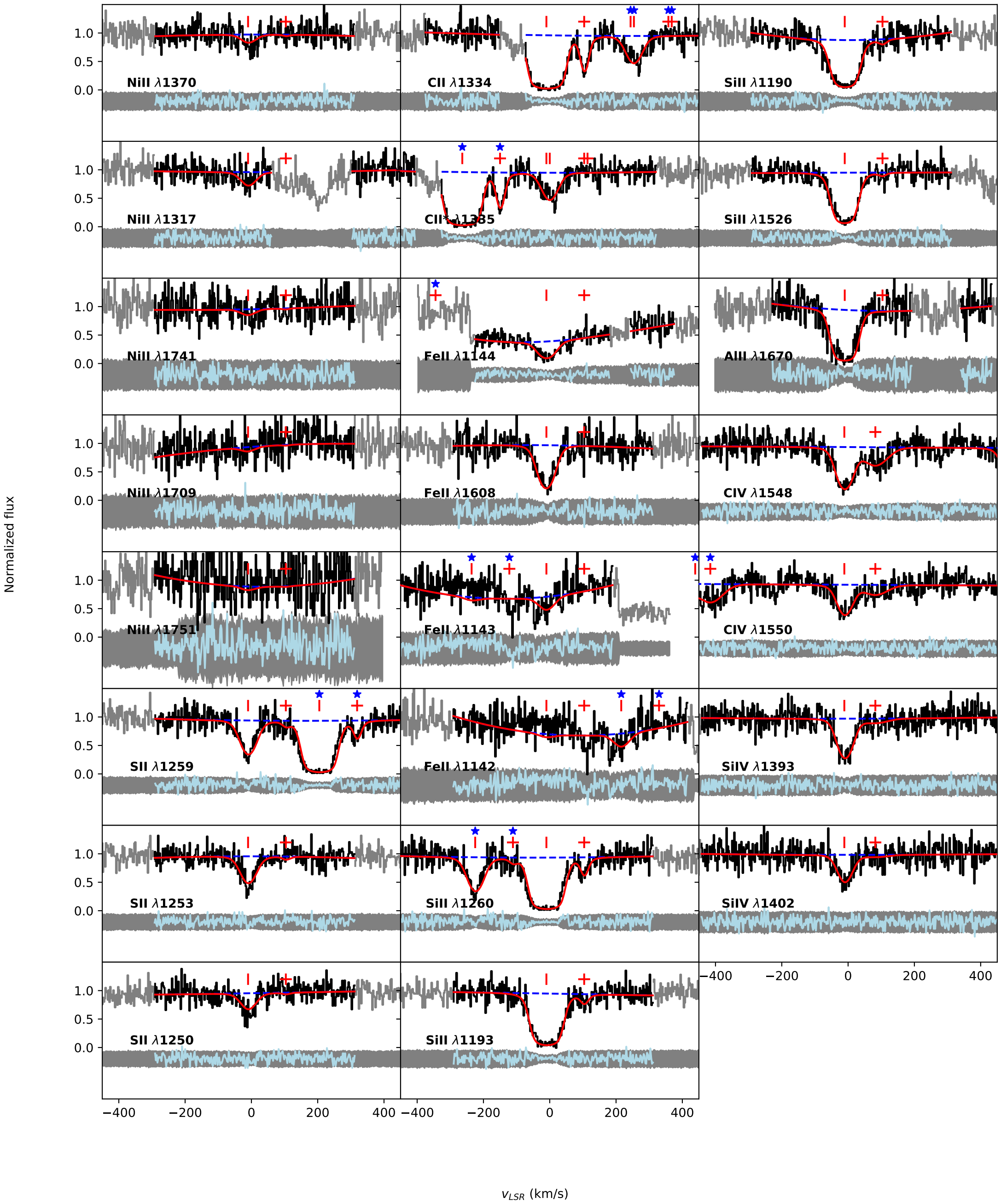

Figure A.4: ALIS fit of the MW absorption in sightline *SDSS-J141309.14+092011.2*.

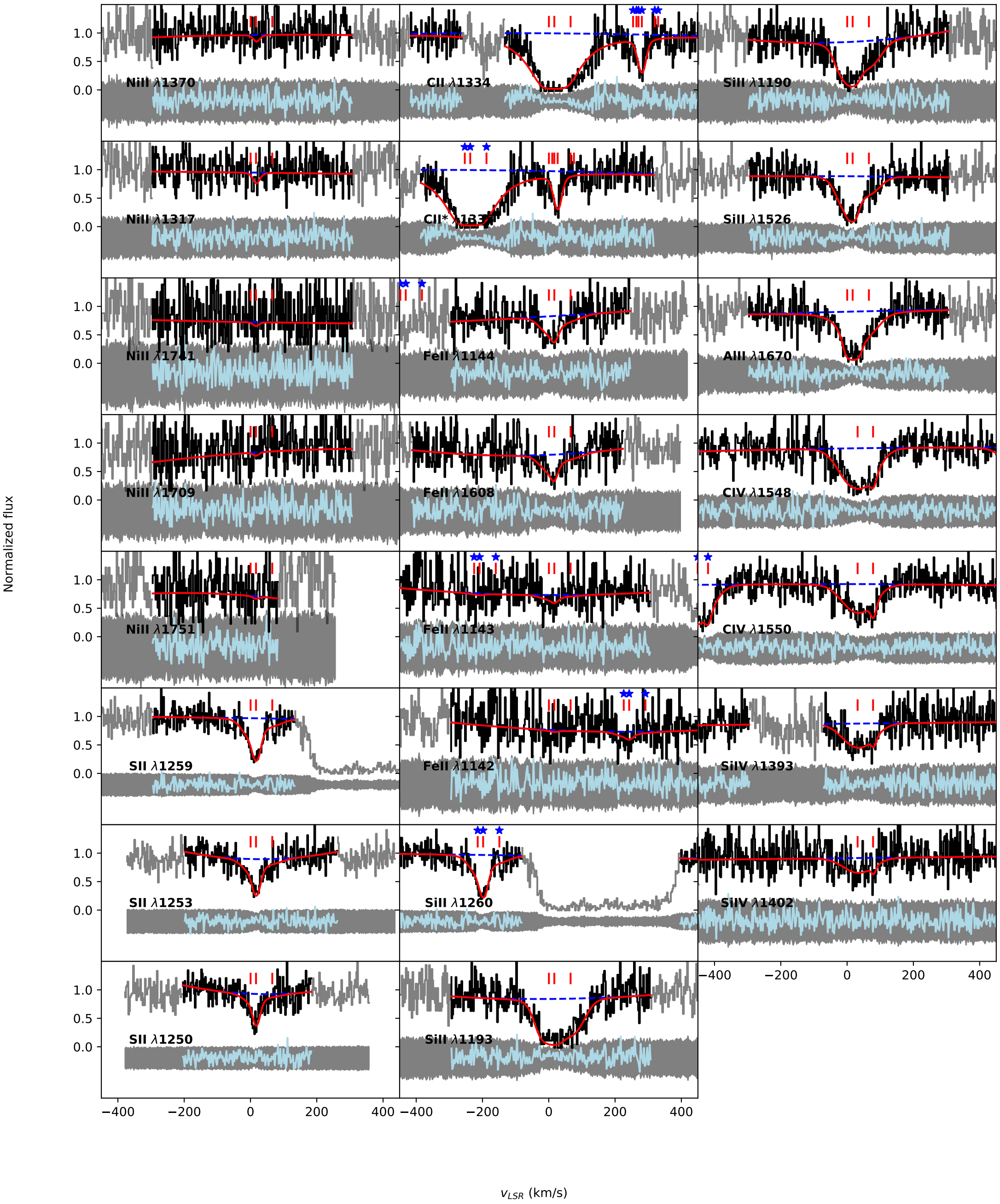

Figure A.5: ALIS fit of the MW absorption in sightline *ESO462-G09*.

Annex B

Column densities

QSO	Glon °	Glat °	H I log(cm^{-2})	H I$_{err}$ log(cm^{-2})	H I$_{flag}$	Ni II log(cm^{-2})	Ni II$_{err}$ log(cm^{-2})	Ni II$_{flag}$	S II log(cm^{-2})	S II$_{err}$ log(cm^{-2})	S II$_{flag}$	C II log(cm^{-2})	C II$_{err}$ log(cm^{-2})	C II$_{flag}$	C II* log(cm^{-2})	C II*$_{err}$ log(cm^{-2})	C II*$_{flag}$	Fe II log(cm^{-2})	Fe II$_{err}$ log(cm^{-2})	Fe II$_{flag}$	Si II log(cm^{-2})	Si II$_{err}$ log(cm^{-2})	Si II$_{flag}$	Al II log(cm^{-2})	Al II$_{err}$ log(cm^{-2})	Al II$_{flag}$	C IV log(cm^{-2})	C IV$_{err}$ log(cm^{-2})	C IV$_{flag}$	Si IV log(cm^{-2})	Si IV$_{err}$ log(cm^{-2})	Si IV$_{flag}$
ngc-985	180.8371	-59.4902	20.5	0.0	damped	13.5	0.03	detect	15.58	0.01	detect	13.78	0.04	satura*	13.89	0.02	detect*	14.97	0.04	detect	13.26	0.08	satura	12.62	0.08	satura*	14.03	0.03	detect	13.4	0.03	detect
ngc7714	88.2156	-55.5642	20.75	0.01	damped	13.45	0.0	nondet	...	...	...	14.93	0.07	detect*	...	...	...	14.14	0.36	satura*	13.0	0.72	satura	12.43	0.29	satura*	...	...	...	...	...	...
pds456	10.3922	11.1635	21.38	0.03	damped	14.16	0.03	detect	15.36	0.03	satura	14.03	0.2	satura*	14.08	0.05	satura*	14.83	0.04	detect	13.78	0.09	satura	12.76	0.1	satura*	13.72	0.04	satura	12.87	0.09	satura
pg-1407+265	34.6687	72.5886	20.01	0.0	damped	13.7	0.03	detect	15.3	0.02	detect	13.58	0.13	satura*	14.03	0.02	detect*	13.79	0.13	satura*	16.05	0.07	satura	12.52	0.12	satura*	13.83	0.05	satura	13.85	0.02	detect
pg-1522+101	14.8922	50.1217	20.34	0.01	damped	13.61	0.0	nondet	15.16	0.01	detect	14.06	0.04	satura*	14.09	0.02	detect*	...	...	...	14.12	0.02	detect	12.77	0.07	detect*	14.29	0.05	detect	...	...	...
pg-1630+377	60.3421	42.9393	19.78	0.0	damped	13.19	0.0	nondet	15.08	0.02	detect	13.75	0.07	satura*	13.81	0.04	detect*	13.78	0.13	satura*	12.77	0.06	satura	12.74	0.26	satura*	13.54	0.19	satura	14.0	0.04	detect
pg0003+158	107.3184	-45.3258	20.58	0.01	damped	13.43	0.08	detect	15.3	0.05	detect	20.86	0.07	satura*	14.14	0.05	detect*	14.79	0.31	detect	12.97	0.05	satura	13.65	1.82	satura*	14.29	0.02	detect	13.63	0.02	detect*
pg0052+251	123.9075	-37.4378	20.58	0.01	damped	13.64	0.05	detect	14.63	0.09	satura	14.25	0.03	satura*	13.63	0.08	satura*	14.96	0.1	detect	13.31	0.02	satura	12.31	0.13	satura*	13.92	0.03	detect	13.49	0.02	detect
pg0804+761	138.2789	31.0327	20.5	0.0	damped	13.55	0.01	detect	15.75	0.0	detect	13.77	0.03	satura*	14.19	0.0	detect*	14.84	0.01	detect	19.15	0.02	satura	15.91	0.02	satura*	14.26	0.02	detect	13.65	0.02	detect
pg0832+251	199.4907	33.1462	20.41	0.01	damped	13.54	0.07	detect	15.61	0.05	detect	13.6	0.21	satura*	13.64	0.1	satura*	15.49	0.12	detect	13.36	0.09	satura	12.44	0.24	satura*	13.84	0.08	detect	13.25	0.06	detect
pg0953+414	179.7861	51.7091	20.0	0.0	damped	13.27	0.0	nondet	15.29	0.02	detect	13.36	0.13	satura*	14.12	0.02	detect*	14.78	0.03	detect	12.24	0.05	satura	12.14	0.14	satura*	13.92	0.07	detect	13.43	0.06	detect
pg1001+291	200.0835	53.2069	20.2	0.02	damped	13.54	0.06	detect	15.32	0.02	detect	13.69	0.26	satura*	14.08	0.03	detect*	14.93	0.03	detect	13.1	0.07	satura	18.96	0.09	satura*	14.23	0.09	detect*	13.67	0.08	detect
pg1011-040	246.5011	40.7487	20.54	0.0	damped	13.72	0.02	detect	15.32	0.01	detect	14.48	0.09	satura*	14.03	0.02	detect*	15.32	0.04	detect	13.6	0.06	satura	12.65	0.11	satura*	13.91	0.17	detect	13.31	0.18	detect
pg1048+342	190.6024	63.4374	20.19	0.0	damped	13.51	0.0	nondet	15.42	0.02	detect	14.11	0.08	satura*	14.16	0.03	detect*	14.58	0.06	satura	13.14	0.04	satura	12.18	0.14	satura*	14.14	0.02	detect	13.69	0.01	detect
pg1049-005	252.2763	49.8783	20.6	0.01	damped	13.74	0.0	nondet	15.59	0.06	detect	14.23	0.14	satura*	16.02	0.07	satura*	15.27	0.13	detect	13.06	0.15	satura	12.57	0.08	satura*	13.5	0.0	nondet	12.83	0.0	nondet
pg1115+407	172.2337	66.6686	20.12	0.01	damped	13.49	0.0	nondet	15.33	0.07	detect	13.81	0.1	satura*	13.81	0.1	detect*	14.99	0.05	detect	13.54	0.1	satura	12.76	0.15	satura*	14.12	0.06	detect	13.68	0.45	detect
pg1116+215	223.3597	68.2091	20.05	0.0	damped	13.63	0.03	detect	15.28	0.01	detect	13.77	0.16	satura*	13.8	0.06	detect*	14.84	0.03	detect	13.09	0.05	satura	12.09	0.11	satura*	14.34	0.03	detect	13.79	0.02	detect
pg1121+422	167.2577	66.8587	20.34	0.01	damped	13.69	0.05	detect	15.38	0.01	detect	15.02	0.08	satura*	14.03	0.03	detect*	15.05	0.05	detect	14.23	0.05	satura	13.24	0.08	satura*	14.15	0.03	detect	13.62	0.03	detect
pg1202+281	205.9628	79.6131	20.36	0.02	damped	13.84	0.0	nondet	15.46	0.06	detect	13.87	0.38	satura*	13.87	0.17	detect*	14.13	0.17	satura*	13.56	0.2	satura	12.68	0.29	satura*	13.85	0.17	detect	13.47	0.12	detect
pg1216+069	281.0714	68.1433	20.13	0.01	damped	13.33	0.0	nondet	15.26	0.02	detect	13.63	0.07	satura*	13.99	0.08	satura*	14.87	0.1	detect	13.31	0.18	satura	12.39	0.22	satura*	14.07	0.04	detect*	13.52	0.02	detect
pg1222+216	255.0733	81.6598	20.25	0.01	damped	13.69	0.04	detect	15.36	0.02	detect	14.22	0.03	satura*	...	...	...	14.68	0.04	detect	13.31	0.02	satura	12.51	0.07	satura*	14.23	0.01	detect	13.59	0.02	detect
pg1259+593	120.5556	58.0478	20.24	0.0	damped	13.3	0.05	detect	15.19	0.01	detect	13.76	0.04	satura*	13.86	0.03	detect*	14.88	0.02	detect	12.75	0.03	satura	13.0	0.05	satura*	13.84	0.03	detect	13.45	0.04	detect
pg1352+183	4.3748	72.8738	20.16	0.01	damped	13.46	0.05	detect	15.16	0.01	detect	13.84	0.08	satura*	13.8	0.04	detect*	14.65	0.02	detect	13.08	0.05	satura	12.57	0.06	satura*	14.42	0.04	detect	13.7	0.01	detect
pg1424+240	29.4874	68.2076	20.55	0.02	damped	13.72	0.05	detect	15.29	0.02	detect	13.65	0.19	satura*	14.18	0.03	detect*	14.83	0.04	detect	13.43	0.15	satura	12.37	0.18	satura*	14.43	0.01	detect	13.74	0.02	detect
pg1626+554	84.5149	42.1886	20.02	0.0	damped	13.46	0.04	detect	14.91	0.02	detect	14.19	0.28	satura*	13.83	0.03	detect*	14.61	0.04	detect	13.07	0.1	satura	12.22	0.18	satura*	13.5	0.03	satura	13.62	0.04	detect
phl1811	47.4732	-44.8152	20.62	0.0	damped	13.46	0.03	detect	15.37	0.02	detect	13.97	0.05	satura*	13.56	0.02	satura*	14.63	0.05	detect	13.17	0.06	satura	12.24	0.13	satura*	14.74	0.09	detect	13.93	0.12	detect
phl2525	80.6834	-71.3172	20.29	0.01	damped	13.54	0.0	nondet	15.32	0.04	detect	18.87	0.05	satura*	14.03	0.0	nondet	14.7	0.06	detect	14.14	0.16	satura	12.56	0.24	satura*	14.4	0.09	detect	13.79	0.07	detect
pks0405-123	204.9271	-41.7563	20.53	0.0	damped	13.53	0.01	detect	15.58	0.01	detect	...	...	...	...	...	...	14.68	0.02	detect	13.32	0.02	satura	12.39	0.04	satura*	13.93	0.02	detect	13.24	0.01	detect
pks0552-640	273.4656	-30.6114	20.55	0.01	damped	13.24	0.0	nondet	15.25	0.03	detect	94.98	0.48	satura*	112.41	0.07	satura*	15.04	0.1	detect	13.89	0.02	satura	12.93	0.03	satura*	14.35	0.1	detect	13.4	0.05	detect
pks0558-504	257.9622	-28.5693	20.55	0.01	damped	13.5	0.0	nondet	14.83	0.17	satura	13.48	0.08	satura*	13.52	0.12	satura*	15.22	0.11	detect	13.25	0.11	satura	12.76	0.67	satura*	14.38	0.05	detect	13.72	0.04	detect
pks0637-752	286.3684	-27.1584	20.83	0.01	damped	13.42	0.05	detect	15.4	0.05	detect	inf	0.36	satura*	15.12	0.14	satura*	15.31	0.1	detect	13.05	0.18	satura	12.76	0.12	satura*	14.13	0.03	detect	13.49	0.04	detect
pks1302-102	308.5914	52.1613	20.44	0.0	damped	13.66	0.1	detect	15.16	0.01	satura	13.57	0.04	satura*	13.37	0.43	satura*	15.11	0.08	detect	12.63	0.04	satura	12.51	0.14	satura*	14.11	0.04	detect	13.77	0.03	detect
pks2005-489	350.3731	-32.6008	20.53	0.02	damped	13.43	0.0	nondet	15.5	0.01	detect	13.84	0.47	satura*	14.29	0.02	detect*	15.22	0.08	detect	13.59	0.32	satura	12.82	0.63	satura*	13.53	0.07	satura	13.48	0.08	satura
pmnj1103-2329	273.1895	33.0796	20.65	0.01	damped	13.7	0.09	detect	15.48	0.03	detect	14.12	0.07	satura*	14.19	0.05	satura*	14.81	0.11	detect	13.66	0.11	satura	12.86	0.14	satura*	14.02	0.04	detect	13.41	0.05	detect
pmnj2345-1555	65.6728	-70.9852	20.2	0.01	damped	13.54	0.0	nondet	15.09	0.03	detect	13.92	0.1	satura*	13.67	0.07	detect*	14.24	0.06	detect	12.66	0.21	satura	12.63	0.05	satura*	14.14	0.04	satura	14.06	0.03	detect
q0349-146	205.4845	-46.3249	20.62	0.01	damped	13.67	0.0	nondet	15.5	0.02	detect	13.8	0.18	satura*	13.93	0.06	satura*	14.52	0.07	detect*	13.47	0.1	satura	12.56	0.1	satura*	14.0	0.03	detect	13.41	0.04	detect
q1545+210	33.8982	49.4575	20.5	0.02	damped	13.8	0.08	detect	15.12	0.03	satura	116.93	0.82	satura*	14.16	0.08	detect*	14.83	0.09	satura*	31.42	0.06	satura	31.2	0.09	satura*	13.99	0.04	satura	13.92	0.05	detect
q2251+155	86.111	-38.1839	20.84	0.04	damped	13.86	0.0	nondet	15.2	0.08	satura	14.67	0.53	satura*	14.75	0.13	satura*	14.4	0.65	detect	14.02	0.24	satura	12.56	0.25	satura*	14.34	0.02	detect	13.39	0.07	satura*
qso-b0952+457	173.1141	50.7408	19.98	0.03	damped	13.94	0.0	nondet	15.22	0.06	detect	17.0	0.18	satura*	14.32	0.08	detect*	14.64	0.08	detect	14.24	0.09	satura	12.8	0.24	satura*	13.85	0.07	detect	13.17	0.16	detect
qso-b1139+305	197.1451	74.513	20.2	0.03	damped	13.91	0.0	nondet	15.26	0.07	detect	22.04	0.34	satura*	13.9	0.0	nondet	14.58	0.05	detect	13.7	0.23	satura	12.44	0.08	satura*	14.0	0.03	detect	13.52	0.07	satura
qso-b1215+303	188.8749	82.0529	20.15	0.01	damped	13.38	0.0	nondet	15.28	0.03	detect	14.0	0.04	satura*	14.1	0.04	detect*	14.88	0.05	detect	15.45	0.23	satura	12.79	0.13	satura*	13.93	0.09	detect	13.33	0.08	detect
rbs144	299.4835	-65.836	20.32	0.01	damped	13.54	0.0	nondet	15.13	0.02	detect	13.95	0.03	satura*	13.72	0.04	detect*	14.81	0.03	detect	12.85	0.03	satura	12.4	0.2	satura*	13.95	0.55	detect	13.37	0.43	detect
rbs1666	358.7327	-31.0031	20.55	0.02	damped	13.54	0.0	nondet	15.6	0.06	detect	13.65	0.15	satura*	13.25	0.56	satura*	14.97	0.13	detect	13.79	0.07	satura	12.8	0.28	satura*	14.55	0.02	detect	13.88	0.02	detect
rbs1892	345.8979	-58.3672	19.8	0.01	damped	13.74	0.05	detect	14.99	0.04	detect	13.56	0.17	satura*	13.72	0.06	detect*	14.55	0.05	detect	12.7	0.08	satura	12.47	0.34	satura*	14.15	0.04	detect	13.5	0.05	detect
rbs2000	350.1952	-67.5845	20.1	0.01	damped	13.64	0.0	nondet	15.09	0.03	detect	13.82	0.08	satura*	14.1	0.05	detect*	14.82	0.05	detect	12.7	0.06	satura	12.03	0.26	satura*	14.39	0.03	detect	13.75	0.03	detect
rbs2005	97.9384	-36.7987	20.63	0.01	damped	13.4	0.0	nondet	14.64	0.15	satura	16.12	0.17	satura*	14.16	0.07	satura*	14.84	0.12	detect	13.5	0.15	satura	12.68	0.18	satura*	13.65	0.03	satura	13.82	0.02	detect
rbs2055	106.6723	-34.6585	20.48	0.01	damped	13.53	0.0	nondet	15.49	0.02	detect	14.1	0.36	satura*	14.15	0.05	detect*	14.75	0.05	detect	13.94	0.16	satura	12.54	0.56	satura*	14.36	0.03	detect	12.74	0.1	satura
rbs563	272.2534	-39.2259	20.28	0.01	damped	13.72	0.0	nondet	15.36	0.04	detect	14.31	0.04	satura*	13.43	0.0	nondet	15.0	0.08	detect	13.29	0.04	satura	12.38	0.13	satura*	14.65	0.05	detect	13.91	0.03	detect
rxj0028.1+3103	117.0873	-31.5443	20.8	0.01	damped	13.79	0.15	detect	15.15	0.12	satura	13.99	0.07	satura*	14.33	0.06	detect*	15.02	0.1	detect	12.87	0.06	satura	14.64	0.2	satura*	14.08	0.07	detect	13.64	0.09	detect
rxj1230.8+0115	291.2603	63.6598	20.21	0.0	damped	13.29	0.07	detect	15.49	0.01	detect*	13.7	0.02	satura*	13.88	0.04	detect*	14.74	0.06	detect*	12.48	0.02	satura	...	...	...	14.23	0.11	detect	13.55	0.12	detect
rxj2154.1-4414	355.1792	-50.8646	19.96	0.01	damped	13.39	0.0	nondet	15.24	0.03	detect	13.9	0.09	satura*	13.9	0.03	detect*	14.65	0.08	detect	13.12	0.09	satura	12.25	0.17	satura*	14.13	0.04	detect	13.62	0.05	detect
rxs-j00057-5007	320.7101	-65.4054	20.01	0.0	damped	13.33	0.06	detect	15.02	0.01	detect	13.44	0.43	satura*	13.66	0.05	detect*	14.55	0.05	detect*	13.0	0.06	satura	12.27	0.25	satura*	14.31	0.04	detect	13.75	0.03	detect
rxs-j21388-3828	4.5093	-48.4647	20.33	0.0	damped	13.45	0.0	nondet	15.37	0.04	detect	13.48	0.37	satura*	13.53	0.04	satura*	13.75	0.25	satura*	13.06	0.03	satura	12.4	0.16	satura*	13.3	1.12	satura	13.81	0.03	detect
rxs-j23218-7026	313.2924	-44.8373	20.41	0.0	damped	13.27	0.06	detect	15.42	0.05	detect	13.47	0.22	satura*	13.71	0.04	satura*	14.53	0.05	detect*	13.17	0.03	satura	12.35	0.12	satura*	13.2	0.07	satura	13.73	0.01	detect
rxsj00437+3725	121.2326	-25.4243	20.65	0.01	damped	13.53	0.0	nondet	15.62	0.04	detect	13.78	0.09	satura*	13.77	0.12	satura*	15.1	0.09	detect	13.34	0.05	satura	12.59	0.13	satura*	14.31	0.05	detect	13.53	0.04	detect
rxsj00508+3536	122.7965	-27.2596	20.6	0.02	damped	13.51	0.0	nondet	14.72	0.56	satura	13.63	0.49	satura*	13.53	0.1	satura*	15.08	0.11	detect	13.28	0.02	satura	12.32	0.15	satura*	13.92	0.07	detect	13.39	0.07	detect
rxsj00537+2232	123.638	-40.3291	20.46	0.01	damped	13.62	0.0	nondet	15.28	0.05	detect	14.49	0.09	satura*	14.38	0.21	satura*	14.71	0.11	detect	13.03	0.07	satura	12.33	0.59	satura*	13.62	0.0	nondet	13.34	0.02	detect
rxsj01188+3836	128.7826	-23.9549	20.64	0.01	damped	13.91	0.07	detect	15.68	0.02	detect	13.87	0.08	satura*	14.35	0.05	detect*	15.11	0.09	detect	12.75	0.06	satura	13.75	0.21	satura*	13.7	0.07	detect	13.29	0.07	detect
rxsj0155.6+3115	138.7027	-29.6442	20.6	0.01	damped	13.56	0.07	detect	15.49	0.04	detect	18.04	0.05	satura*	14.26	0.06	detect*	14.95	0.1	detect	13.55	0.05	satura	12.59	0.21	satura*	13.79	0.07	detect	13.37	0.04	detect*
s50716+714	143.981	28.0176	20.41	0.0	damped	13.46	0.03	detect	15.58	0.03	detect	14.4	0.06	satura*	14.21	0.05	detect*	15.01	0.06	detect	13.29	0.02	satura	12.35	0.19	satura*	14.17	0.02	detect	13.52	0.02	detect
sbs1122+594	141.8033	54.7097	19.82	0.02	damped	13.67	0.0	nondet	15.28	0.04	detect	18.66	41.59	satura*	13.94	0.06	detect*	15.22	0.24	detect	16.26	0.39	satura	12.35	0.51	satura*	14.17	0.06	detect	13.7	0.06	detect*
sdss-j100535.24+013445.7	238.5271	42.7859	20.41	0.02	damped	13.54	0.0	nondet	15.39	0.04	detect	14.17	0.44	satura*	13.99	0.06	detect*	14.95	0.06	detect	13.44	0.24	satura	13.31	0.26	satura*	14.22	0.04	detect	13.64	0.05	detect
sdss-j104741.75+151332.2	229.0848	58.908	20.3	0.01	damped	13.85	0.04	detect	15.41	0.02	detect	16.35	0.14	satura*	14.17	0.03	detect*	15.12	0.05	detect	15.34	0.06	satura	14.57	0.12	satura*	14.25	0.02	detect	...	...	...
sdss-j141038.39+230447.1	24.5712	71.6404	20.19	0.02	damped	13.73	0.0	nondet	13.86	0.28	satura	14.33	0.14	satura*	13.95	0.12	detect*	...	...	...	inf	0.06	satura	inf	0.19	satura*	13.6	0.07	satura	13.79	0.07	detect
sdss-j141309.14+092011.2	354.0969	63.759	20.2	0.01	damped	13.57	0.0	nondet	15.08	0.02	detect	13.87	0.14	satura*	13.99	0.04	detect*	14.63	0.04	detect	12.58	0.07	satura	12.66	0.11	satura*	14.26	0.02	detect	13.62	0.03	detect
sdssj004222.29-103743.8	115.129	-73.3631	20.35	0.03	damped	13.86	0.0	nondet	15.14	0.07	detect	13.73	0.5	satura*	13.8	0.12	detect*	14.87	0.16	detect	13.39	0.17	satura	12.51	0.47	satura*	14.01	0.08	detect	13.38	0.1	detect
sdssj011623.04+142940.5	131.9646	-47.9392	20.59	0.03	damped	13.91	0.0	nondet	15.09	0.07	detect	14.23	0.41	satura*	13.95	0.13	detect*	14.17	0.12	satura*	13.82	0.29	satura	12.9	0.22	satura*	13.93	0.07	detect	13.45	0.1	detect
sdssj024250.85-075914.2	182.1522	-57.4171	20.33	0.02	damped	13.84	0.0	nondet	15.2	0.07	detect	14.16	0.24	satura*	13.89	0.13	detect*	14.92	0.3	detect	13.38	0.26	satura	12.46	0.25	satura*	14.11	0.41	detect	13.64	0.42	detect
sdssj025937.46+003736.3	176.1811	-48.5328	20.88	0.02	damped	13.92	0.0	nondet	15.4	0.13	detect	13.68	0.14	satura*	13.89	0.41	satura*	15.33	0.3	detect	13.49	0.16	satura	12.57	0.86	satura*	13.92	0.06	detect	13.68	0.06	detect
sdssj031027.82-004950.7	180.5367	-47.5388	20.69	0.01	damped	13.66	0.0	nondet	15.49	0.07	detect	14.17	0.24	satura*	14.21	0.09	satura*	14.87	0.14	detect	13.23	0.09	satura	12.37	0.47	satura*	13.6	0.0	nondet	13.46	0.08	detect

Table B.1: Continuation of Table 3.4.

QSO	Glon °	Glat °	H I log(cm^{-2})	H I$_{err}$ log(cm^{-2})	H I$_{flag}$	Ni II log(cm^{-2})	Ni II$_{err}$ log(cm^{-2})	Ni II$_{flag}$	S II log(cm^{-2})	S II$_{err}$ log(cm^{-2})	S II$_{flag}$	C II log(cm^{-2})	C II$_{err}$ log(cm^{-2})	C II$_{flag}$	C II* log(cm^{-2})	C II*$_{err}$ log(cm^{-2})	C II*$_{flag}$	Fe II log(cm^{-2})	Fe II$_{err}$ log(cm^{-2})	Fe II$_{flag}$	Si II log(cm^{-2})	Si II$_{err}$ log(cm^{-2})	Si II$_{flag}$	Al II log(cm^{-2})	Al II$_{err}$ log(cm^{-2})	Al II$_{flag}$	C IV log(cm^{-2})	C IV$_{err}$ log(cm^{-2})	C IV$_{flag}$	Si IV log(cm^{-2})	Si IV$_{err}$ log(cm^{-2})	Si IV$_{flag}$
sdssj040148.98-054056.5	196.4159	-39.9697	20.75	0.02	damped	13.72	0.0	nondet	14.44	0.7	satura	13.97	7.54	satura*	13.39	0.65	satura*	14.67	0.34	detect	12.74	0.17	satura	12.11	0.99	satura*	13.94	0.06	detect	13.95	0.04	detect
sdssj080359.23+433258.4	176.3972	30.995	20.71	0.02	damped	13.87	0.0	nondet	15.06	0.67	satura	19.53	0.09	satura*	19.9	0.47	satura*	13.93	0.92	satura*	13.33	0.17	satura	12.97	0.42	satura*	14.03	0.06	detect	13.41	0.1	detect
sdssj080908.13+461925.6	173.3223	32.2889	20.51	0.01	damped	13.57	0.0	nondet	14.72	0.2	satura	13.82	0.34	satura*	13.36	0.11	satura*	15.02	0.07	detect	13.72	0.22	satura	13.2	0.27	satura*	14.13	0.02	detect	13.69	0.03	detect
sdssj082024.21+233450.4	199.8037	29.4163	20.58	0.02	damped	13.73	0.0	nondet	14.71	0.48	satura	55.53	0.56	satura*	52.09	0.11	satura*	15.03	0.23	detect	16.56	0.23	satura	11.96	0.54	satura*	14.05	0.06	detect	13.55	0.06	detect
sdssj082633.51+074248.3	216.8903	24.6341	20.45	0.02	damped	13.84	0.0	nondet	14.78	0.13	satura	14.74	0.05	satura*	13.97	0.12	detect*	13.78	0.54	satura*	13.92	0.7	satura	12.26	1.33	satura*	14.24	0.07	detect	13.86	0.06	detect
sdssj085116.14+424328.8	178.4853	39.4838	20.35	0.03	damped	13.85	0.0	nondet	15.09	0.1	satura	14.37	0.12	satura*	13.86	0.0	nondet	0.0	0.0	borrar	13.21	0.97	satura	12.45	0.49	satura*	14.01	0.06	detect	13.55	0.13	detect*
sdssj091440.38+282330.6	198.1323	42.4466	20.2	0.02	damped	13.75	0.0	nondet	15.08	0.08	satura	14.17	0.23	satura*	inf	0.79	satura*	14.79	0.12	detect	13.17	0.2	satura	201.92	5.86	satura*	13.9	0.15	detect	13.39	0.25	detect
sdssj092554.43+453544.4	174.3152	45.5962	20.16	0.01	damped	13.56	0.06	detect	15.24	0.02	detect	inf	0.25	satura*	14.0	0.05	detect*	14.99	0.16	detect	13.3	0.04	satura	12.84	0.58	satura*	13.89	0.05	detect	13.51	0.06	detect
sdssj092909.79+464424.0	172.5843	46.01	20.2	0.01	damped	13.56	0.0	nondet	15.36	0.02	detect	20.3	0.15	satura*	13.96	0.05	detect*	14.94	0.07	detect	13.65	0.06	satura	12.69	0.11	satura*	13.46	0.08	detect	13.13	0.07	detect
sdssj094733.21+100508.7	225.3726	43.5395	20.4	0.03	damped	13.62	0.0	nondet	15.05	0.08	detect	22.49	0.23	satura*	14.02	0.12	detect*	14.78	0.16	detect	13.56	0.22	satura	16.37	0.26	satura*	14.05	0.19	detect	13.58	0.16	detect
sdssj094840.08+580039.1	155.8267	45.7313	19.64	0.07	damped	74.82	0.94	satura	14.76	0.21	satura	14.19	0.26	satura*	14.01	0.26	detect*	14.85	0.18	detect	13.1	0.13	satura	12.64	0.23	satura*	13.94	0.06	detect	13.19	0.16	detect
sdssj094952.91+390203.9	183.5185	50.5948	20.21	0.02	damped	13.68	0.0	nondet	15.34	0.03	detect	17.64	0.11	satura*	13.85	0.08	detect*	14.98	0.09	detect	13.99	0.07	satura	12.95	0.08	satura*	13.9	0.09	detect	13.29	0.1	detect
sdssj095000.73+483129.3	168.9598	49.0984	19.81	0.03	damped	13.8	0.0	nondet	15.23	0.04	detect	12.15	0.12	satura*	13.84	0.13	detect*	14.59	0.13	detect	12.88	0.1	satura	12.7	0.21	satura*	13.69	0.0	nondet	13.28	0.15	detect*
sdssj095915.65+050355.1	233.37	43.4835	20.44	0.01	damped	13.76	0.0	nondet	15.19	0.04	detect	13.96	0.47	satura*	13.89	0.08	detect*	14.82	0.08	detect*	12.95	0.12	satura	12.56	0.17	satura*	14.18	0.04	detect	13.58	0.04	detect*
sdssj101622.60+470643.3	169.0288	53.7423	19.8	0.04	damped	13.83	0.0	nondet	14.74	0.0	nondet	35.39	0.78	satura*	102.38	0.37	satura*	14.12	3.47	satura*	13.19	0.42	satura	12.63	0.43	satura*	13.65	0.28	detect	13.07	0.31	detect
sdssj102218.99+013218.8	242.16	46.0656	20.61	0.02	damped	13.8	0.0	nondet	15.33	0.08	satura	18.79	0.26	satura*	17.34	0.1	satura*	15.54	0.24	satura	13.72	0.07	satura	12.84	0.15	satura*	13.96	0.08	detect	13.56	0.07	detect
sdssj105945.23+144142.9	232.8312	61.2037	20.15	0.02	damped	13.68	0.0	nondet	15.34	0.05	detect	14.34	0.22	satura*	14.59	0.11	detect*	14.98	0.1	detect	13.95	0.17	satura	13.19	0.28	satura*	14.06	0.06	detect	13.66	0.06	detect
sdssj105958.82+251708.8	210.811	64.9832	19.96	0.03	damped	13.82	0.0	nondet	15.25	0.03	detect	14.44	0.24	satura*	13.68	0.14	detect*	14.64	0.13	detect	13.99	0.09	satura	12.83	0.14	satura*	14.14	0.04	detect	13.52	0.07	detect
sdssj110312.93+414154.9	172.5526	63.5238	19.69	0.12	damped	13.7	0.0	nondet	15.16	0.05	detect	14.64	0.21	satura*	13.57	0.0	nondet	14.79	0.11	detect	13.53	0.07	satura	13.36	0.17	satura*	14.12	0.05	detect	13.55	0.07	detect
sdssj110406.94+314111.4	195.4121	66.2495	20.33	0.02	damped	13.7	0.0	nondet	15.48	0.05	detect	16.26	0.24	satura*	14.15	0.07	detect*	13.98	0.25	satura*	13.17	0.14	satura	12.49	0.36	satura*	14.17	0.04	detect	13.56	0.05	detect
sdssj111754.31+263416.6	209.1002	69.16	19.93	0.02	damped	13.81	0.0	nondet	15.32	0.23	detect	13.84	0.52	satura*	13.76	0.24	detect*	15.02	0.2	detect	13.69	0.5	satura	12.61	0.51	satura*	14.31	0.04	detect	13.65	0.05	detect
sdssj112244.89+575543.0	143.6452	55.4883	19.62	0.05	damped	13.89	0.0	nondet	15.17	0.08	detect	23.98	0.53	satura*	13.65	0.0	nondet	14.86	0.22	detect	15.92	0.84	satura	12.78	0.17	satura*	14.26	0.05	detect	13.69	0.07	detect
sdssj113457.62+255527.9	212.6185	72.8679	20.31	0.02	damped	13.81	0.0	nondet	15.36	0.09	detect	14.1	0.33	satura*	13.86	0.11	detect*	15.19	0.25	detect	13.06	0.21	satura	12.13	0.21	satura*	14.45	0.18	detect	13.56	0.63	satura
sdssj115758.72-002220.8	275.7139	59.6441	20.53	0.02	damped	13.82	0.0	nondet	14.45	0.47	satura	13.55	0.21	satura*	14.0	0.15	detect*	14.25	0.17	satura	14.29	0.06	satura	12.2	3.23	satura*	14.3	0.03	detect	13.71	0.06	detect
sdssj120720.99+262429.1	214.6163	80.1361	20.18	0.02	damped	13.79	0.0	nondet	15.37	0.06	detect	13.74	0.17	satura*	13.72	0.17	satura*	13.78	0.21	satura*	13.33	0.24	satura	12.31	0.45	satura*	13.73	0.0	nondet	13.24	0.15	detect
sdssj121037.56+315706.0	181.9613	79.9045	19.92	0.05	damped	13.87	0.0	nondet	15.36	0.08	detect	13.46	0.42	satura*	13.99	0.12	detect*	14.79	0.34	detect	13.36	0.28	satura	17.52	0.18	satura*	13.98	0.06	detect	13.32	0.22	detect*
sdssj121114.56+365739.5	161.2592	77.0081	20.2	0.02	damped	13.8	0.0	nondet	15.56	0.08	detect	13.87	0.51	satura*	14.11	0.1	detect*	15.06	0.13	detect	13.56	0.19	satura	12.62	0.36	satura*	13.93	0.07	detect	13.49	0.08	detect
sdssj122035.10+385316.4	149.7092	76.592	20.6	0.03	damped	13.94	0.0	nondet	15.38	0.07	detect	14.08	0.51	satura*	13.95	0.09	satura*	15.31	0.23	detect	13.52	0.39	satura	12.59	0.26	satura*	14.19	0.17	detect*	13.48	0.1	detect
sdssj123235.82+060310.0	290.0851	68.4533	20.1	0.01	damped	13.61	0.0	nondet	15.34	0.05	detect	13.93	0.12	satura*	13.93	0.08	detect*	14.8	0.12	detect	13.19	0.03	satura	12.29	0.08	satura*	14.26	1.22	detect	13.61	4.15	detect
sdssj123304.05-003134.1	293.114	61.9949	20.13	0.01	damped	13.69	0.0	nondet	15.49	0.04	detect	13.93	0.35	satura*	13.7	0.09	detect*	15.29	0.18	detect	13.87	0.28	satura	12.41	0.49	satura*	14.43	0.12	detect	13.93	0.09	detect
sdssj123335.07+475800.4	131.2436	68.8723	19.74	0.04	damped	13.68	0.0	nondet	14.99	0.08	detect	14.44	0.08	satura*	13.75	0.11	detect*	14.95	0.15	detect	13.3	0.75	satura	12.38	0.59	satura*	13.91	0.07	detect	13.51	0.05	detect
sdssj123604.02+264135.9	219.2929	86.5458	20.14	0.03	damped	14.37	0.0	nondet	15.41	0.0	nondet	13.95	0.27	satura*	14.02	0.13	satura*	14.6	0.13	detect*	13.6	0.09	satura	14.03	1.64	detect*	14.28	0.08	detect	13.44	0.11	detect
sdssj124154.02+572107.3	125.4838	59.7289	19.71	0.03	damped	13.79	0.0	nondet	15.02	0.06	detect	13.45	0.35	satura*	13.61	0.0	nondet	0.0	0.0	borrar	12.96	0.09	satura	12.9	0.84	satura*	13.88	0.07	detect	13.14	0.21	detect
sdssj124511.25+335610.1	133.7244	83.0607	20.0	0.03	damped	13.91	0.0	nondet	15.35	0.05	detect	13.82	0.35	satura*	13.98	0.11	detect*	14.57	0.28	detect	13.54	0.24	satura	12.63	0.18	satura*	14.2	0.07	detect	13.08	0.0	nondet
sdssj132222.68+464535.2	107.7083	69.4433	20.08	0.02	damped	13.83	0.0	nondet	15.23	0.07	detect*	14.49	0.38	satura*	13.88	0.1	detect*	14.93	0.12	detect	13.72	0.21	satura	12.99	0.13	satura*	14.09	0.2	detect	13.64	0.36	detect
sdssj133045.15+281321.4	42.3677	81.2298	19.81	0.03	damped	13.78	0.0	nondet	15.3	0.09	detect	18.52	0.24	satura*	14.42	0.09	satura*	14.8	0.28	detect	14.9	0.25	satura	12.62	0.23	satura*	13.81	0.35	satura*	13.66	0.06	detect
sdssj133053.27+311930.5	61.2799	80.4299	19.75	0.02	damped	13.76	0.0	nondet	15.15	0.04	detect	13.74	0.28	satura*	13.75	0.09	detect*	14.65	0.08	detect	13.43	0.12	satura	12.5	0.23	satura*	14.24	0.03	detect	13.66	0.08	detect
sdssj134206.56+050523.8	333.8871	64.8712	20.24	0.02	damped	13.83	0.0	nondet	15.26	0.07	detect	13.53	0.31	satura*	13.63	0.22	detect*	14.8	0.2	detect	12.87	0.32	satura	12.32	0.74	satura*	14.16	0.03	detect	13.59	0.06	detect
sdssj134231.22+382903.4	82.8658	74.4054	19.66	0.02	damped	13.73	0.0	nondet	15.16	0.07	detect	13.97	0.72	satura*	13.71	0.13	detect*	14.69	0.11	detect	13.39	0.42	satura	12.67	0.52	satura*	14.1	0.05	detect	13.57	0.04	detect
sdssj134246.89+184443.6	0.2433	75.525	20.19	0.02	damped	13.77	0.0	nondet	15.17	0.06	detect	13.79	0.16	satura*	13.96	0.1	detect*	15.0	0.19	detect	13.35	0.12	satura	12.42	0.2	satura*	14.48	0.05	detect	13.78	0.05	detect
sdssj134251.60-005345.3	328.819	59.3665	20.3	0.02	damped	13.79	0.08	detect	15.29	0.04	detect	18.07	0.07	satura*	14.13	0.06	detect*	15.21	1.4	satura*	15.28	0.14	satura	12.57	0.2	satura*	13.85	0.22	detect	13.52	0.12	detect
sdssj135625.55+251523.7	29.2703	75.3127	20.15	0.01	damped	13.84	0.0	nondet	15.15	0.05	detect	14.51	0.26	satura*	14.02	0.09	detect*	14.71	0.09	detect	13.62	0.12	satura	12.71	0.24	satura*	14.55	0.11	detect	13.91	0.07	detect
sdssj135712.61+170444.1	2.8604	71.7802	20.3	0.01	damped	13.74	0.1	detect	15.09	0.03	detect	17.93	0.06	satura*	13.91	0.07	detect*	14.74	0.05	detect	13.62	0.03	satura	12.69	0.09	satura*	13.76	0.03	satura	13.77	0.01	detect
sdssj141910.20+420746.9	78.5766	66.6566	19.97	0.03	damped	13.89	0.0	nondet	15.46	0.09	detect	14.13	0.23	satura*	13.64	0.0	nondet	14.59	0.17	detect	13.89	0.12	satura	12.74	0.2	satura*	13.25	6.28	satura	13.37	0.11	detect
sdssj143511.53+360437.2	61.523	66.2579	19.96	0.04	damped	13.89	0.0	nondet	15.48	0.1	detect	13.2	0.4	satura*	13.68	0.0	nondet	14.65	0.17	detect	14.48	0.18	satura	13.44	0.24	satura*	13.58	0.07	satura	13.71	0.06	detect
sdssj144511.28+342825.4	56.7398	64.5904	19.86	0.05	damped	14.21	0.12	detect	15.27	0.09	detect	14.5	0.22	satura*	13.74	0.0	nondet	14.96	0.19	detect	13.78	0.13	satura	12.81	0.35	satura*	14.16	0.1	detect	13.65	0.09	detect
sdssj145108.76+270926.9	39.9451	63.4336	20.46	0.02	damped	13.77	0.0	nondet	15.24	0.07	detect	18.39	0.21	satura*	14.1	0.08	detect*	14.97	0.14	detect	13.2	0.07	satura	12.27	0.13	satura*	14.43	0.15	detect	13.64	0.15	detect
sdssj153644.90+141229.7	22.878	49.4473	20.44	0.03	damped	13.91	0.0	nondet	15.55	0.13	detect	13.76	0.81	satura*	13.72	0.22	satura*	15.02	0.23	satura	13.37	0.51	satura	12.45	0.62	satura*	13.56	0.2	satura	14.04	0.12	detect
sdssj155048.29+400144.9	63.9644	50.94	20.08	0.03	damped	13.8	0.0	nondet	15.06	0.06	detect	13.54	12.35	satura*	13.68	0.12	satura*	14.92	0.18	detect	13.78	0.28	satura	12.67	0.67	satura*	13.66	0.04	satura	13.69	0.05	detect
sdssj155304.92+354828.6	57.2591	50.6668	20.25	0.02	damped	13.88	0.0	nondet	15.3	0.05	detect	13.79	0.39	satura*	13.92	0.1	detect*	14.67	0.18	detect*	13.03	0.08	satura	12.74	0.34	satura*	14.31	0.06	detect	13.79	0.08	detect*
sdssj155504.39+362848.0	58.3163	50.2662	20.08	0.04	damped	13.88	0.0	nondet	15.27	0.1	detect	13.89	0.59	satura*	13.72	0.13	satura*	15.33	0.29	detect	14.13	0.34	satura	12.55	0.65	satura*	14.46	0.07	detect	13.41	0.06	satura
sdssj161916.54+334238.4	54.5935	45.1764	20.08	0.01	damped	13.83	0.0	nondet	15.37	0.09	detect	0.0	0.0	borrar	0.0	0.0	borrar	15.03	0.12	detect	13.39	0.18	satura	13.24	0.14	satura*	13.68	0.02	satura	13.29	0.03	satura*
sdssj213357.89-071217.3	46.5909	-39.2102	20.26	0.07	damped	13.79	0.0	nondet	15.28	0.11	detect	13.89	0.25	satura*	13.94	0.21	satura*	13.65	0.8	satura*	13.08	0.06	satura	12.15	0.17	satura*	14.01	0.07	detect	13.48	0.08	detect
sdssj225738.20+134045.4	85.2834	-40.7284	20.64	0.03	damped	13.9	0.0	nondet	15.35	0.1	satura	132.18	0.39	satura*	14.07	0.14	satura*	15.16	0.49	detect	13.53	0.12	satura	70.61	0.59	satura*	13.97	0.19	detect*	13.76	0.16	detect
sdssj232259.98-005359.2	80.2738	-56.2637	20.59	0.05	damped	13.76	0.0	nondet	15.28	0.04	detect	inf	0.23	satura*	14.12	0.07	detect*	14.65	0.05	detect	14.4	0.06	satura	12.65	0.2	satura*	14.32	0.04	detect	13.68	0.02	detect
sdssj234500.43-005936.0	88.7929	-59.3884	20.54	0.03	damped	13.81	0.0	nondet	15.1	0.08	detect	14.75	0.33	satura*	13.93	0.11	detect*	14.32	0.25	detect*	13.53	0.12	satura	13.29	0.19	detect*	14.2	0.06	detect	13.6	0.07	detect
ton236	44.4333	55.3506	20.3	0.01	damped	13.5	0.0	nondet	14.54	0.06	satura	13.9	0.17	satura*	14.06	0.06	detect*	15.05	0.21	detect	14.2	0.05	satura	12.65	0.66	satura*	14.46	0.02	detect	13.77	0.03	detect
ton580	194.9413	72.0306	20.16	0.01	damped	13.55	0.1	detect	15.45	0.04	detect	13.84	0.17	satura*	14.02	0.02	detect*	15.61	0.46	detect	12.61	0.09	satura	12.43	2.98	satura*	14.17	0.01	detect	13.74	0.02	detect
tons210	224.9715	-83.1603	20.13	0.0	damped	13.08	0.0	nondet	15.29	0.03	detect	13.85	0.02	satura*	13.76	0.04	detect*	14.53	0.03	detect	12.68	0.03	satura	12.43	0.22	satura*	14.47	0.02	detect	13.75	0.02	detect
uks-0242-724	291.8094	-42.3515	20.83	0.04	damped	13.55	0.0	nondet	15.56	0.02	detect	13.65	0.22	satura*	13.7	0.05	satura*	15.26	0.03	detect	12.83	0.09	satura	12.63	0.14	satura*	14.13	0.06	detect	13.6	0.05	detect
viizw244	136.6575	32.6778	20.31	0.01	damped	13.44	0.04	detect	15.46	0.01	detect	17.01	0.36	satura*	14.15	0.02	detect*	14.97	0.06	detect	13.07	0.07	satura	12.15	0.19	satura*	14.18	0.16	detect	13.67	0.16	detect
vv2006-j092542.3+344108	189.9464	45.7029	20.1	0.02	damped	13.84	0.0	nondet	15.02	0.08	satura	14.41	0.17	satura*	286.98	0.85	satura*	14.62	0.11	detect	13.66	0.11	satura	12.62	0.7	satura*	14.05	0.1	detect	13.56	0.12	detect
vv2006-j095240.2+515250	163.8954	48.5293	19.42	0.04	damped	13.68	0.0	nondet	14.97	0.04	detect	14.68	0.08	satura*	13.58	0.11	detect*	14.62	0.04	detect	13.27	0.04	satura	12.28	0.08	satura*	13.55	0.09	detect	13.19	0.1	detect
vv2006-j095243.0+515121	163.927	48.5444	19.68	0.03	damped	13.7	0.0	nondet	14.88	0.05	detect	13.74	0.11	satura*	13.77	0.1	detect*	14.68	0.16	detect	12.62	0.11	satura	14.21	0.09	satura*	13.75	0.05	detect	13.06	0.12	detect
vv2006-j101541.1+594445	151.1512	47.9586	19.8	0.03	damped	13.76	0.0	nondet	15.2	0.04	detect	13.92	0.14	satura*	13.78	0.11	detect*	14.64	0.07	detect	13.68	0.03	satura	12.74	0.23	satura*	13.86	0.12	detect	12.99	0.0	nondet
vv2006-j115412.1+463552	149.2708	67.4951	20.31	0.02	damped	13.73	0.0	nondet	15.42	0.05	detect	16.12	0.35	satura*	14.25	0.13	detect*	14.76	0.1	detect	13.58	0.25	satura	12.72	0.21	satura*	14.15	0.17	detect	13.87	0.2	detect
vv2006-j125901.7+413055	117.238	75.5287	20.01	0.02	damped	13.77	0.0	nondet	15.3	0.04	detect	14.99	0.57	satura*	14.19	0.05	detect*	15.04	0.13	detect	13.57	0.23	satura	12.62	0.21	satura*	14.16	0.03	detect	13.63	0.11	detect*
vv2006-j222836.3-095009	53.2369	-52.1801	20.61	0.02	damped	13.72	0.0	nondet	15.03	0.06	satura	17.82	0.07	satura*	13.78	0.13	satura*	15.04	0.11	detect	13.32	0.05	satura	12.47	0.21	satura*	15.3	0.62	detect	13.66	0.05	detect
zw535.012	120.1742	-17.1262	20.73	0.01	damped	13.57	0.12	detect	14.5	0.44	satura	13.67	0.11	satura*	15.45	0.27	satura*	15.05	0.08	detect	12.75	0.07	satura	12.53	0.15	satura*	13.79	0.73	detect	13.33	0.04	detect

Table B.2: Continuation of Table B.1.

Annex C

ALIS Ly-alpha fits

Here are the fits to the Ly-α of the galaxies in the sample, and like Figure 3.4. The black line is the flux used to run the fit, the grey line is the normalized flux masked out, the dashed blue line is the continuum fitted by ALIS, the red line is the fit by ALIS, the red vertical line denote the velocity centroid of the absorption. The zero velocity is at v_{LSR}.

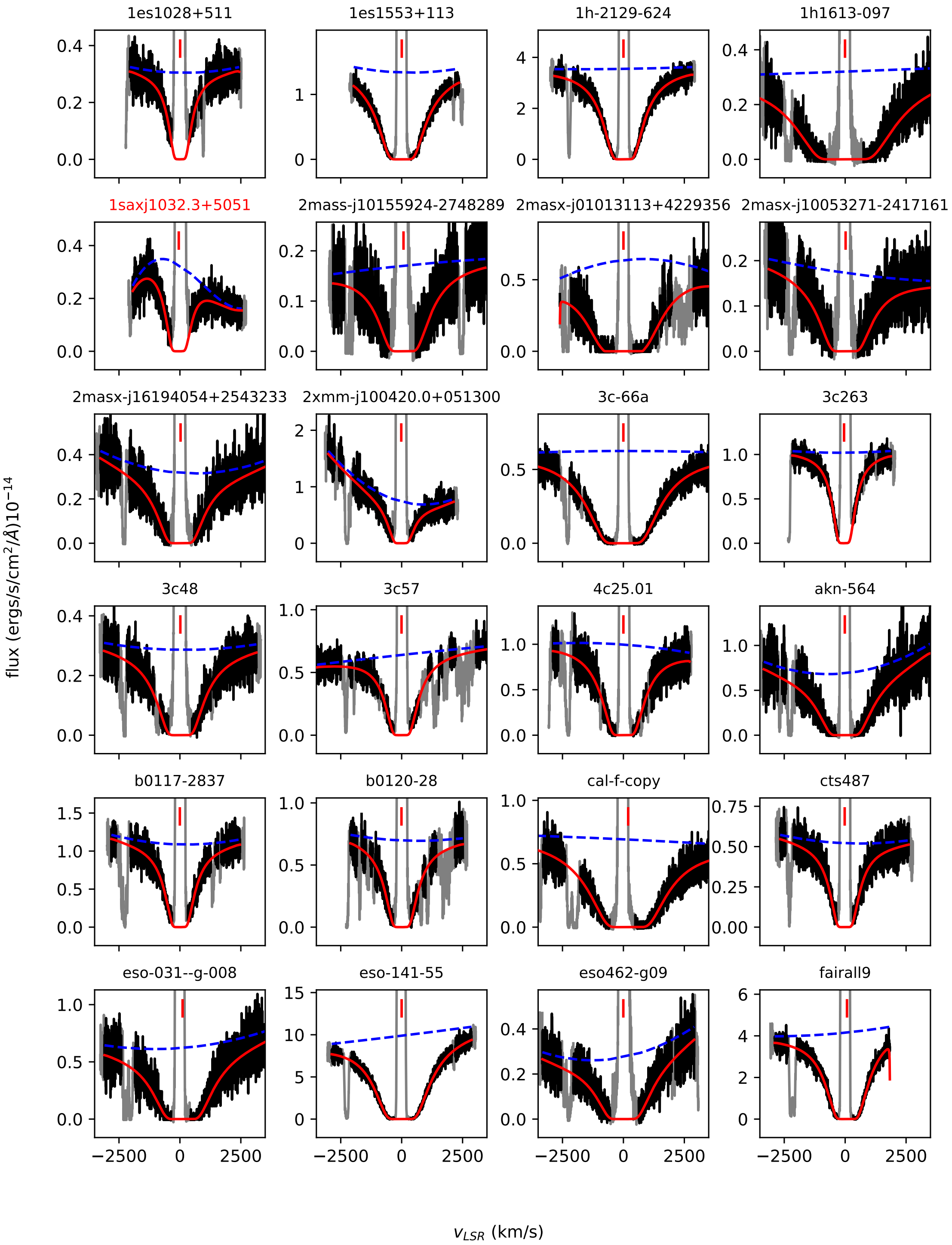

Figure C.1: Ly-α fit with ALIS to systems in the sample.

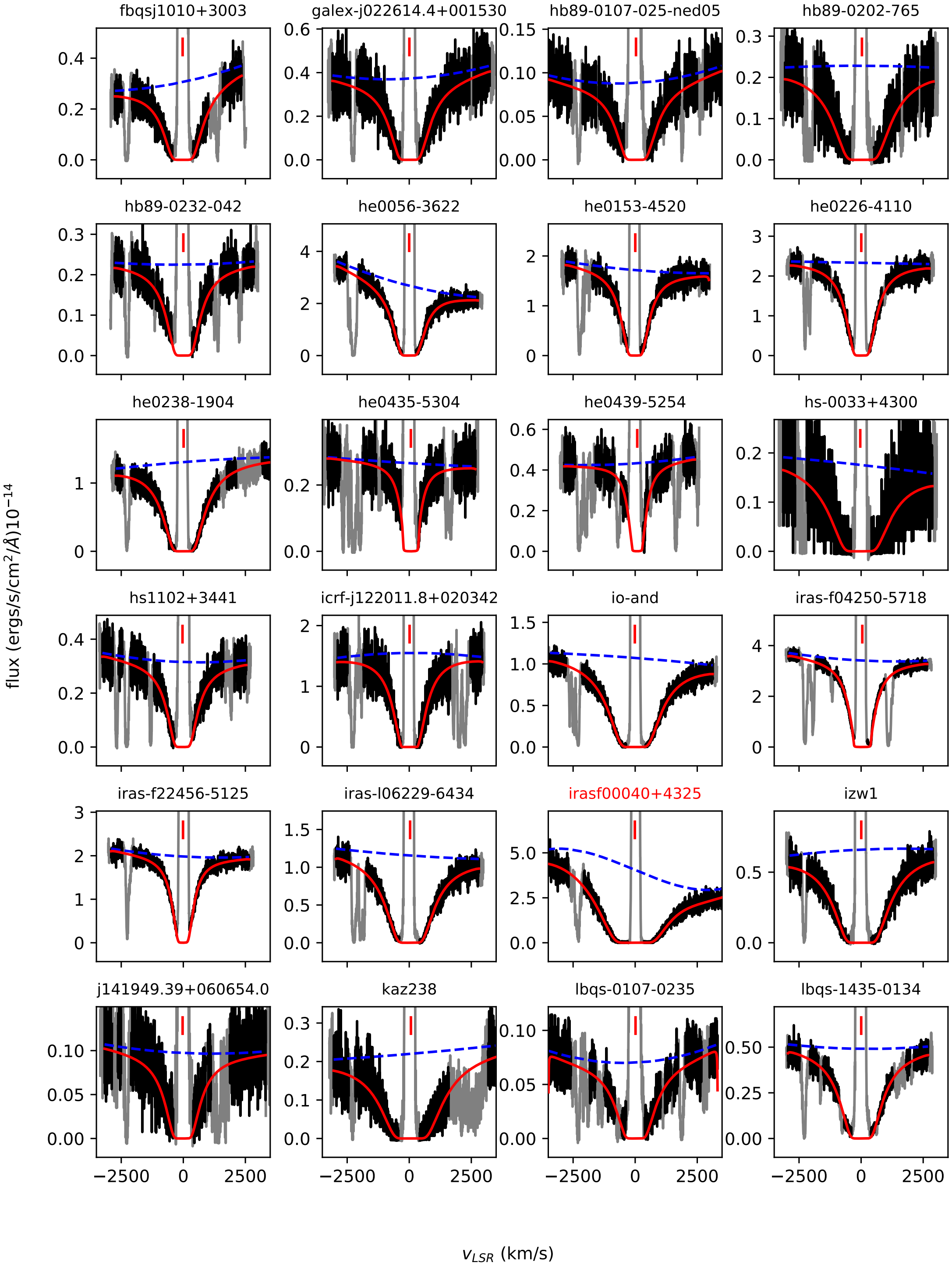

Figure C.2: Ly-α fit with ALIS to systems in the sample.

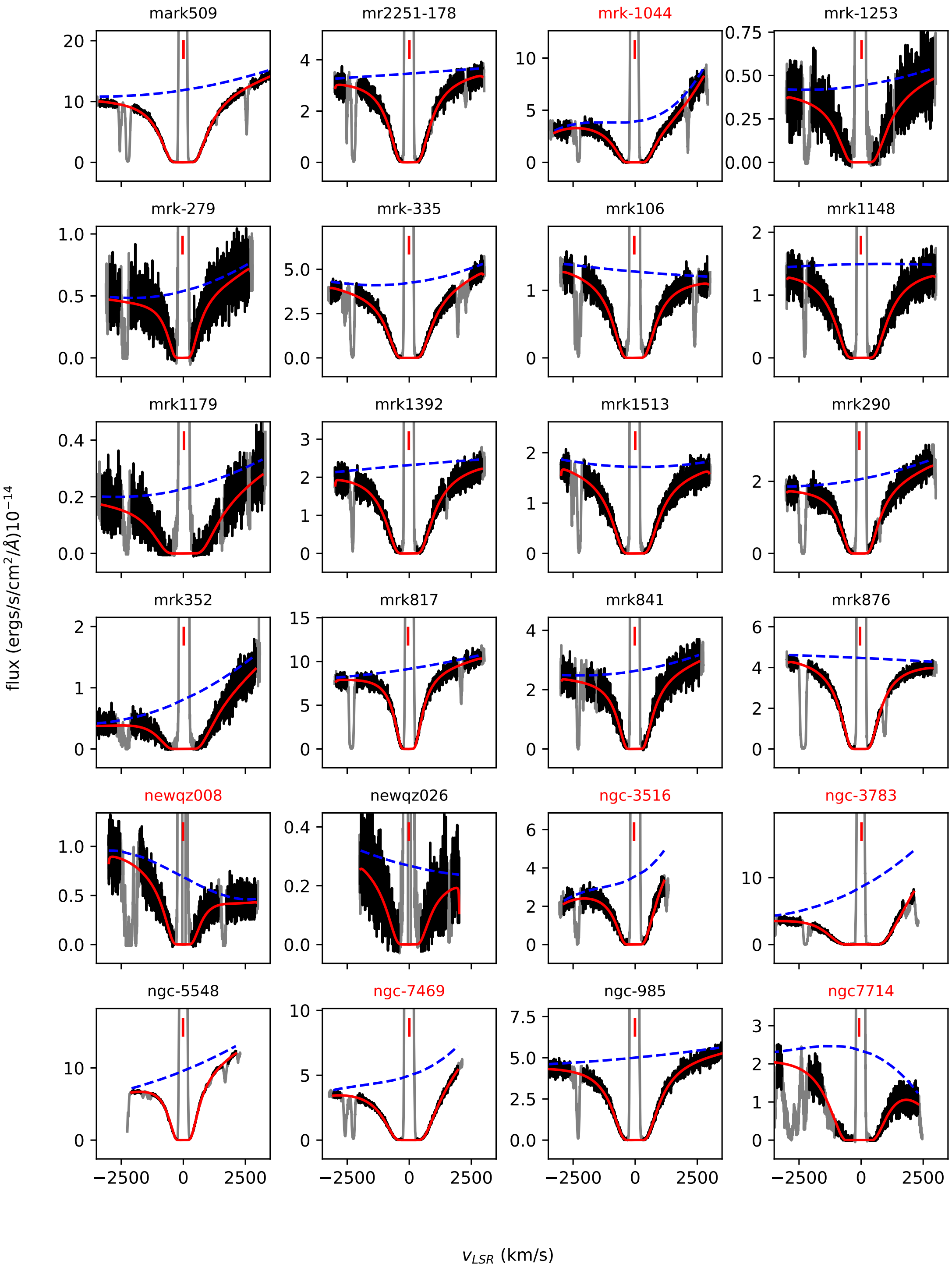

Figure C.3: Ly-α fit with ALIS to systems in the sample.

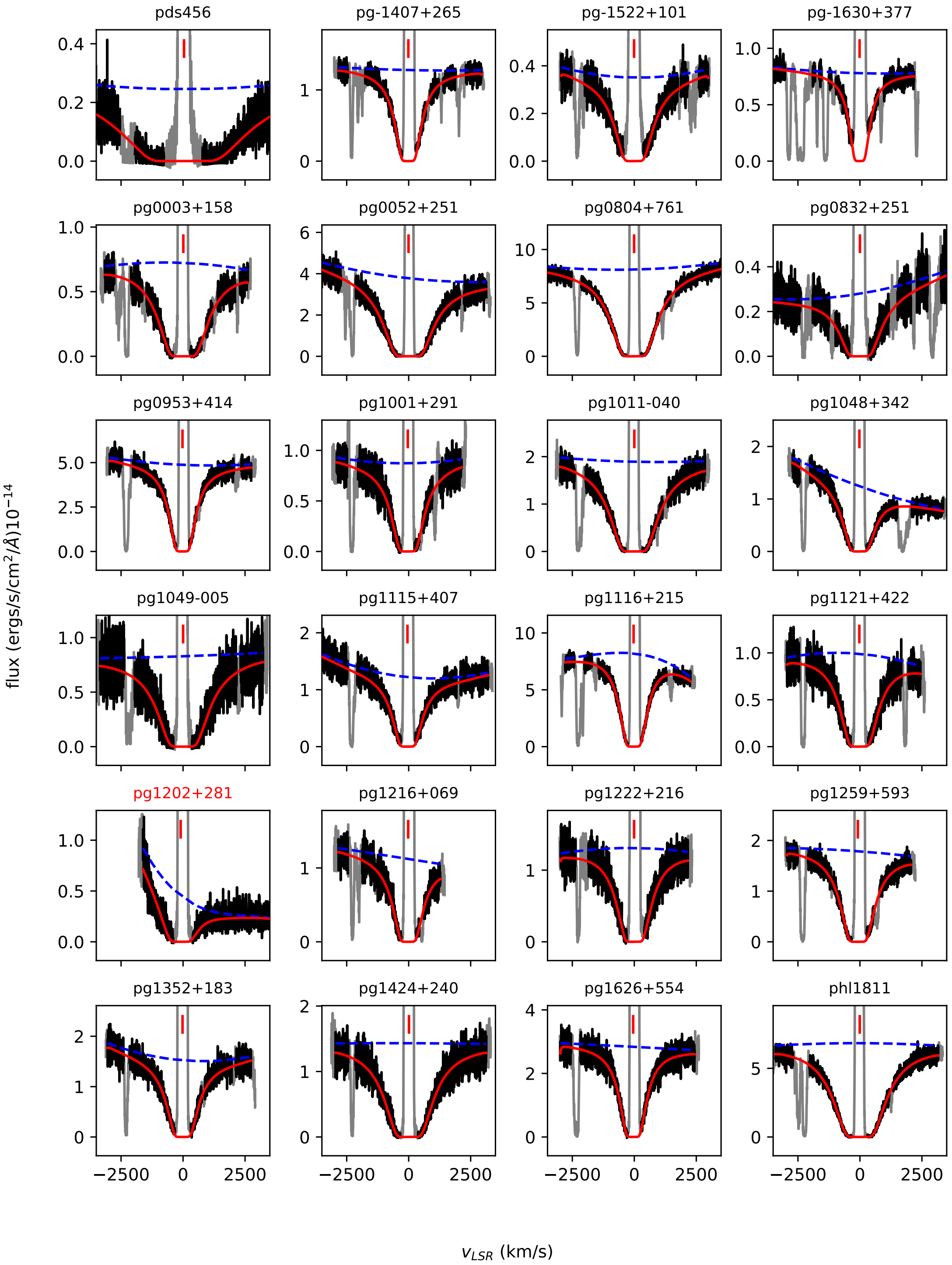

Figure C.4: Ly-α fit with ALIS to systems in the sample.

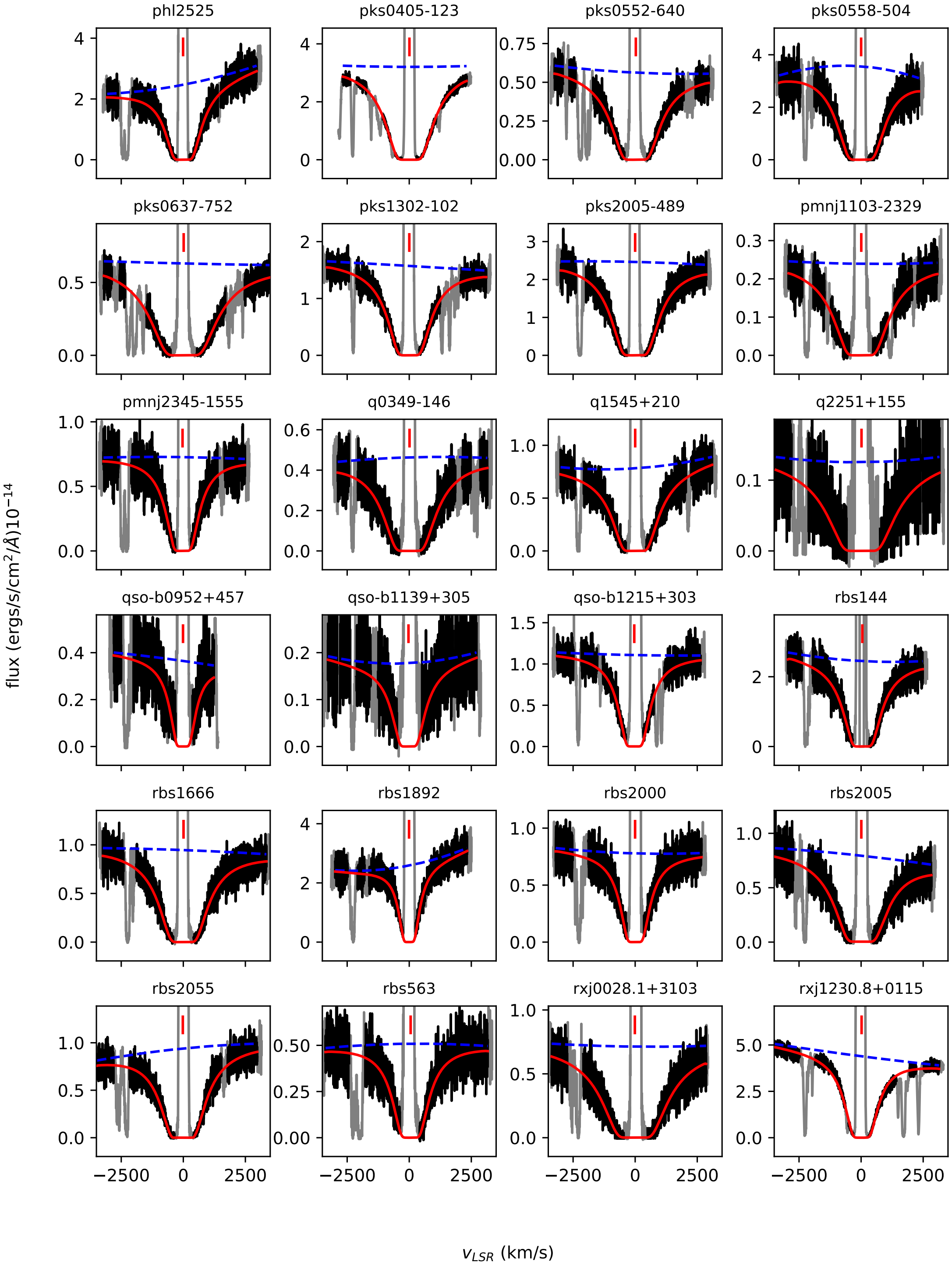

Figure C.5: Ly-α fit with ALIS to systems in the sample.

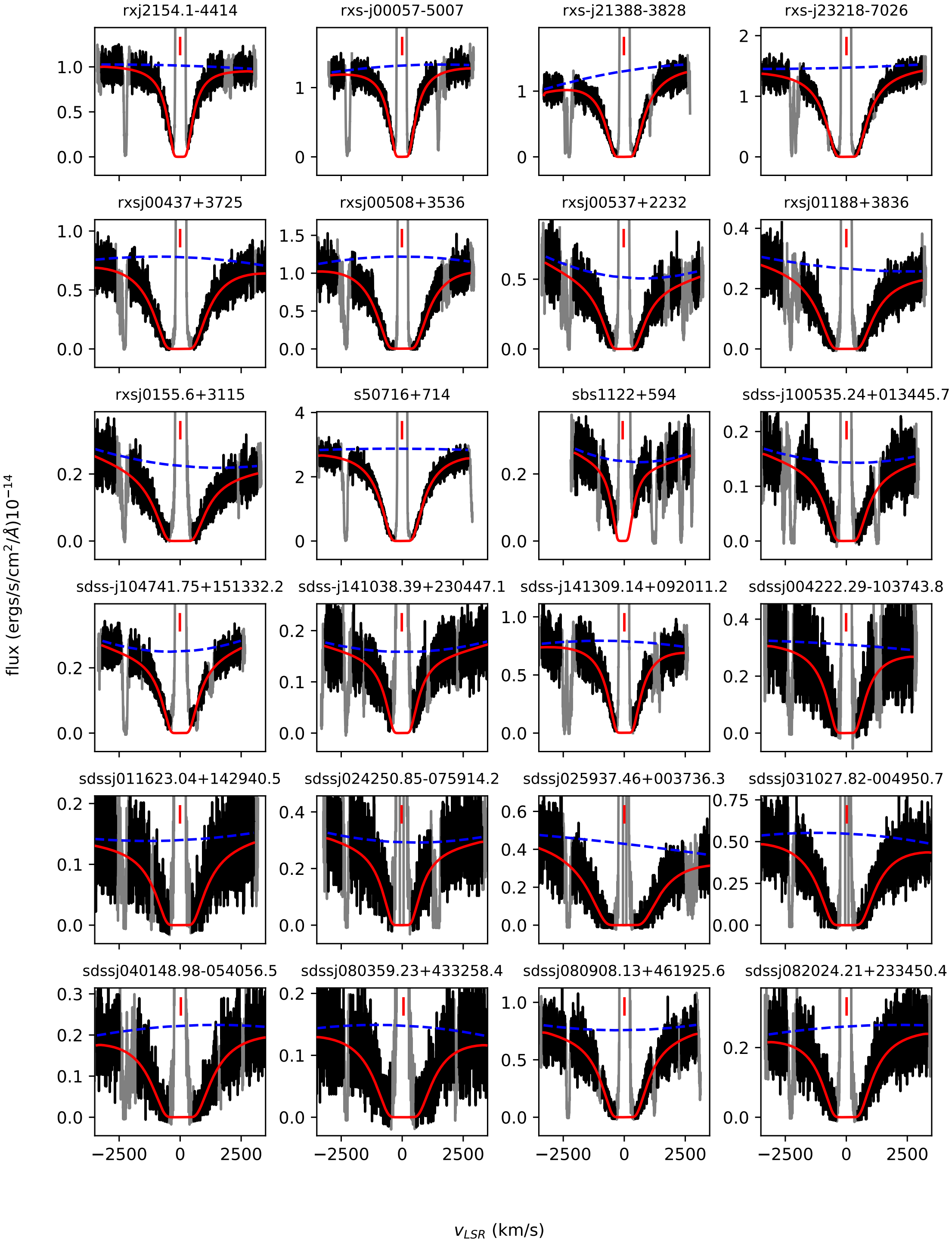

Figure C.6: Ly-α fit with ALIS to systems in the sample

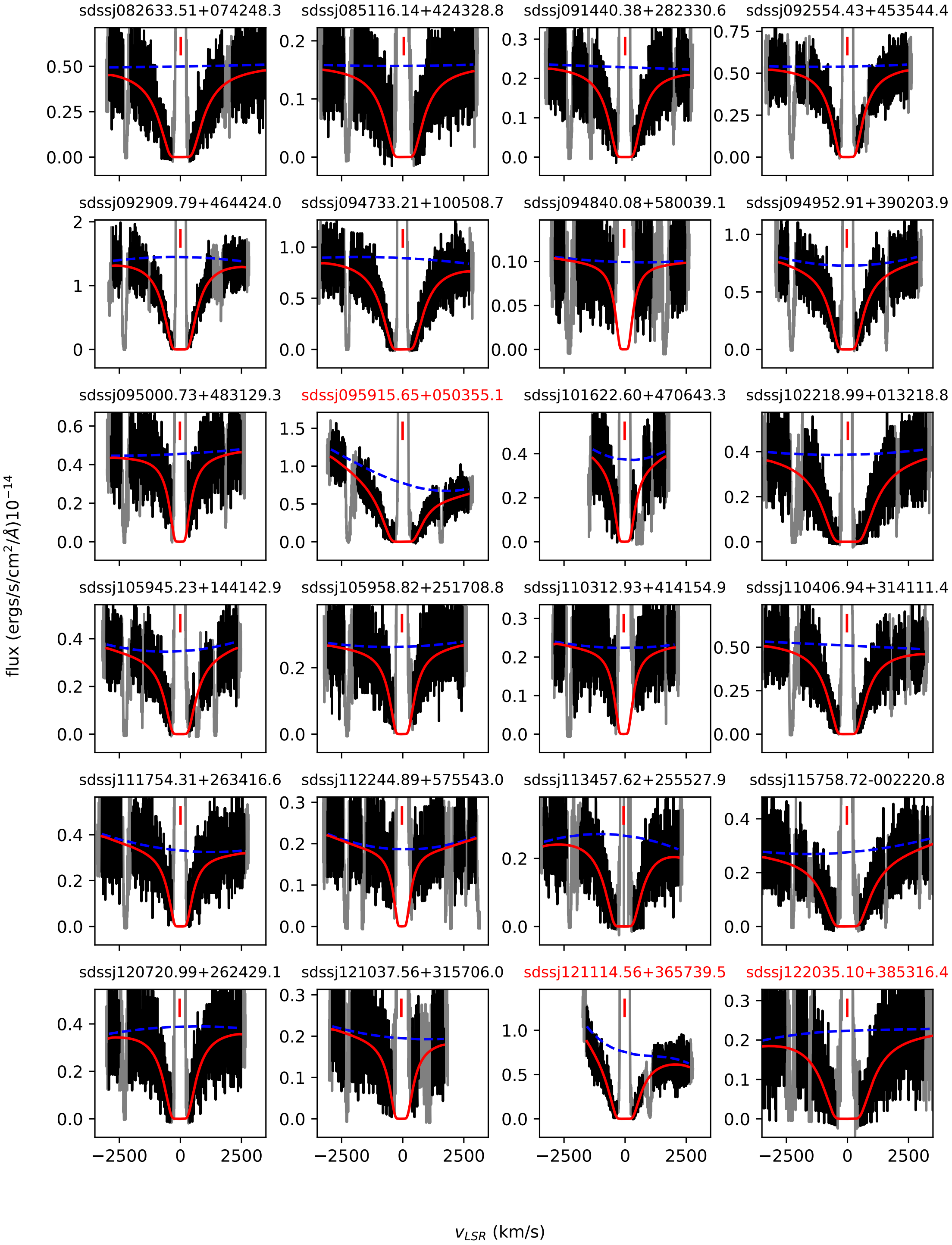

Figure C.7: Ly-α fit with ALIS to systems in the sample.

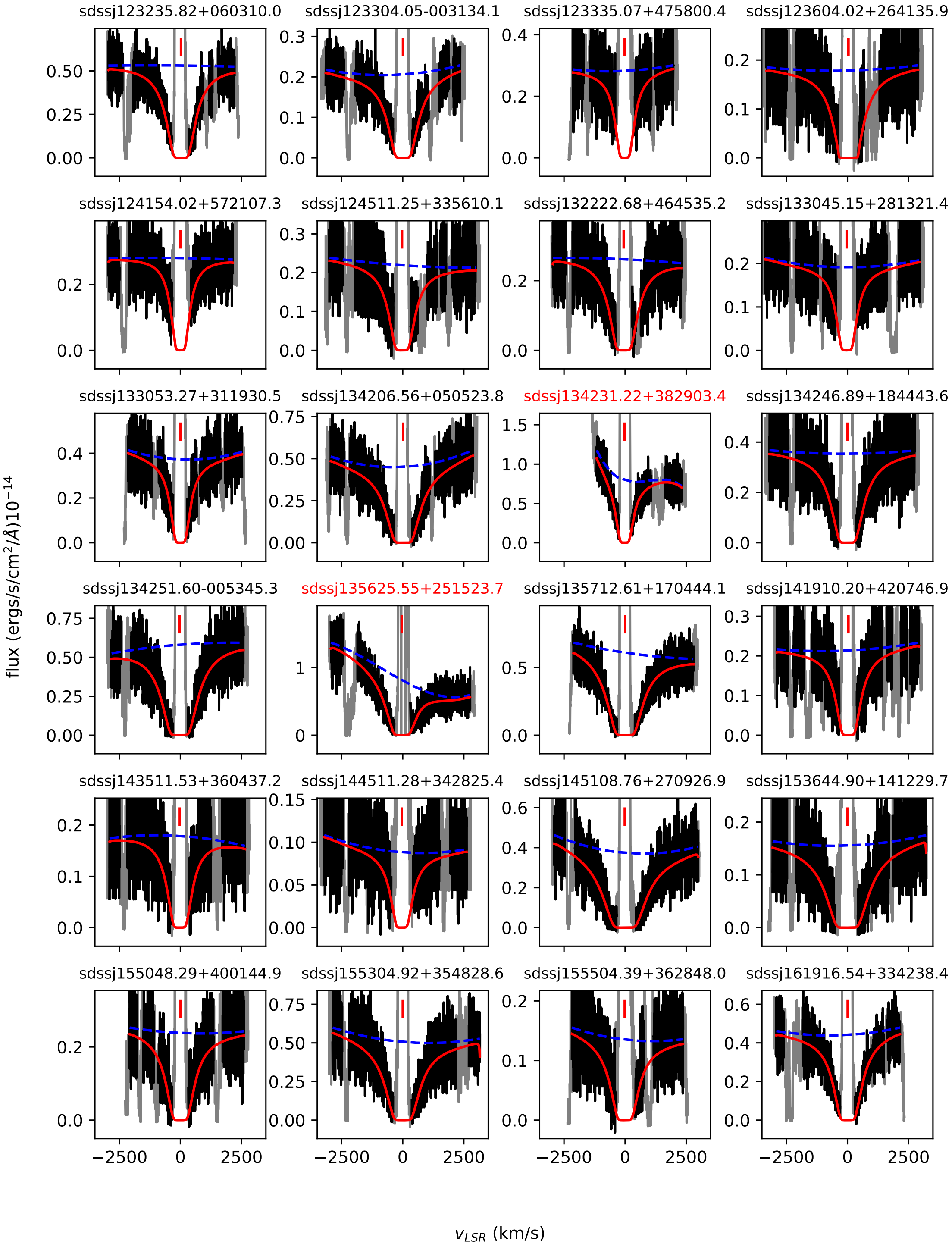

Figure C.8: Ly-α fit with ALIS to systems in the sample. The black line is the flux used to run the fit, the grey line is the normalized flux masked out, the dashed blue line is the continuum fitted by ALIS, the red line is the fit by ALIS, red vertical lines denote the velocity centroid of Milky Way lines. The zero velocity is at v_{LSR}.

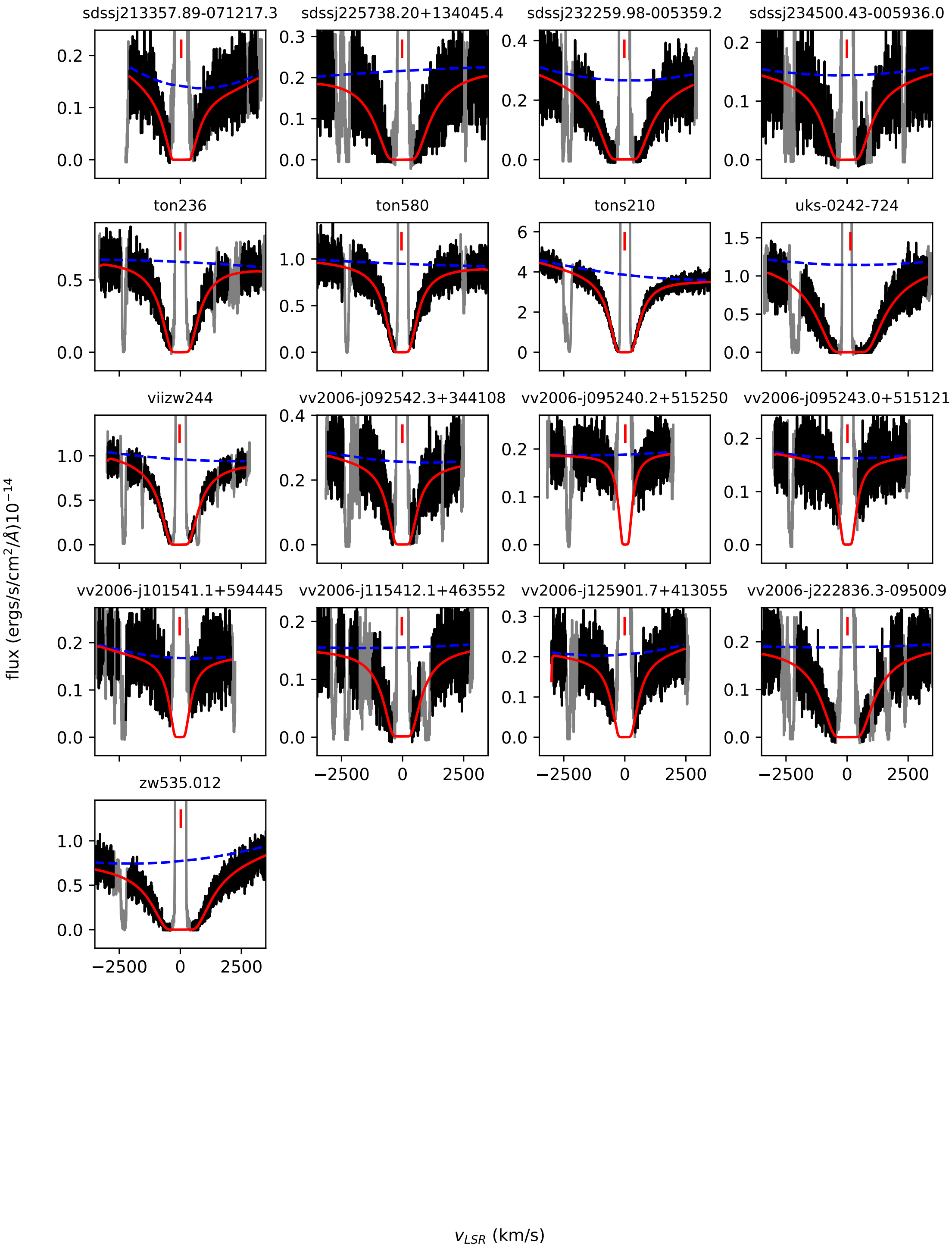

Figure C.9: Ly-α fit with ALIS to systems in the sample.

Annex D

Systems unable to fit Ly-alpha

In this section I show the spectra for which it was impossible to run ALIS to fit HI. Figure D.1 shows the region of the spectra around the rest-frame wavelength of Ly-α, and Table D.1 shows the ID given by Peeples et al. 2017 in the first data release of HSLA, the galactic latitude and longitude, S/N and z of the QSO. In Table D.1 QSO marked **A** all flux from the QSO were completely absorbed by Ly-limit systems, spectra marked **B** interlopers absorption dominated the spectra near the MW Ly-α. In the case of *NGC-4051* it was blended with the emission of the Ly-α of the QSO and possibly absorption from the QSO host galaxy, finally the case of *FBS0150+396* the spectra does not resemble QSO spectra, for this reason I decided to exclude it from the QSO sample.

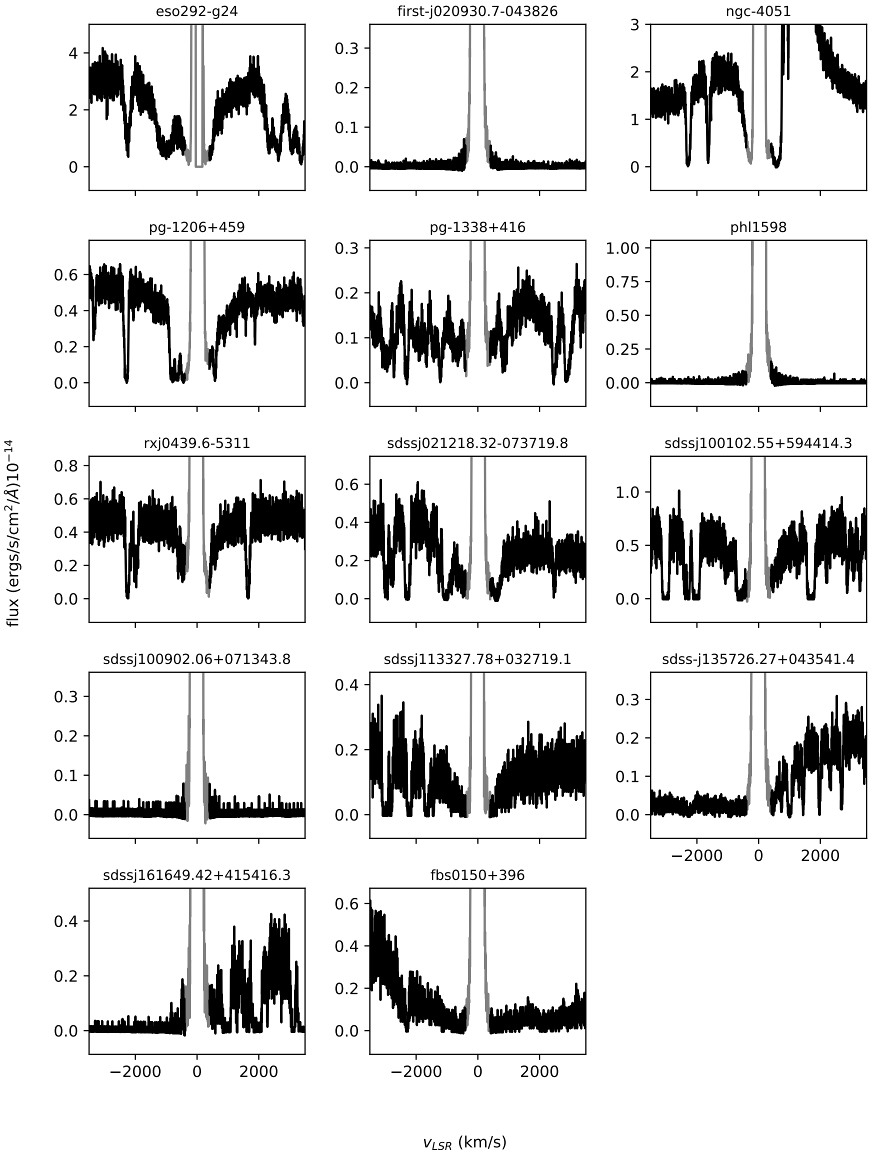

Figure D.1: QSO spectra from which it was impossible to fit Ly-α. The black lines are the flux of the qso, the gray line is the geocoronal emission from Earth's atmosphere. The plot is scaled to show the level of continuum near λ1215, in cases where the flux is completely absorbed the level of continuum closer to the absorption was used.

ID	Glon (°)	Glat (°)	S/N	z
ESO292-G24	334.8992[b]	-68.1571	22.3	0.03
FBS0150+396	135.5828	-21.4226	6.2	0.211
FIRST-J020930.7-043826[a]	165.9922	-60.8074	10.4	1.128
NGC-4051	148.8831	70.0851	19.6	0.002
PG-1206+459[b]	144.6291	69.6209	22.8	1.164
PG-1338+416[b]	90.587	72.4837	16.6	1.217
PHL1598[a]	40.5381	-40.9564	15.4	0.501
RXJ0439.6-5311[b]	261.216	-40.9268	16.9	0.243
SDSS-J135726.27+043541.4[a]	340.7675	62.5141	10.0	1.234
SDSSJ021218.32-073719.8[b]	171.1493	-62.6554	8.2	0.173
SDSSJ100102.55+594414.3[b]	152.5697	46.3865	10.8	0.747
SDSSJ100902.06+071343.8[a]	232.656	46.6973	5.1	0.456
SDSSJ113327.78+032719.1[b]	261.3508	59.8747	5.7	0.524
SDSSJ161649.42+415416.3[a]	66.2768	45.9124	6.5	0.441

Table D.1: COS-GAL spectra for which it was impossible to fit Ly-α absorption. Columns from left to right are: ID name as they appear in HSLA first data release Peeples et al. 2017 , Galactic longitude in degrees, Galactic latitude in degrees, S/N ratio as reported in HSLA first data release.

Annex E

AODM

Before deciding to use Voigt profile fitting to get column densities I tried using the AOD method and noticed that saturation could largely affect the column densities of Fe or Si, which are important to study the [α/Fe] ratio. Figure E.1 shows [α/Fe] measured in the atmosphere of stars in the MW, and the cluster of orange stars at the bottom are the [α/Fe] measured with AODM.

The large discrepancy between the [α/Fe] measured with Si or S, rises suspicion that Si is saturated, and that the measured [Si/Fe] is a lower limit. Also saturation from Fe could make [S/Fe] appear higher than it should. Also if Si and Fe are both saturated, then neither [α/Fe] is relevant, because it is both an upper limit and a lower limit.

To avoid any conflict with saturation, I decided to not use the AODM, and star Voigt profile fitting.

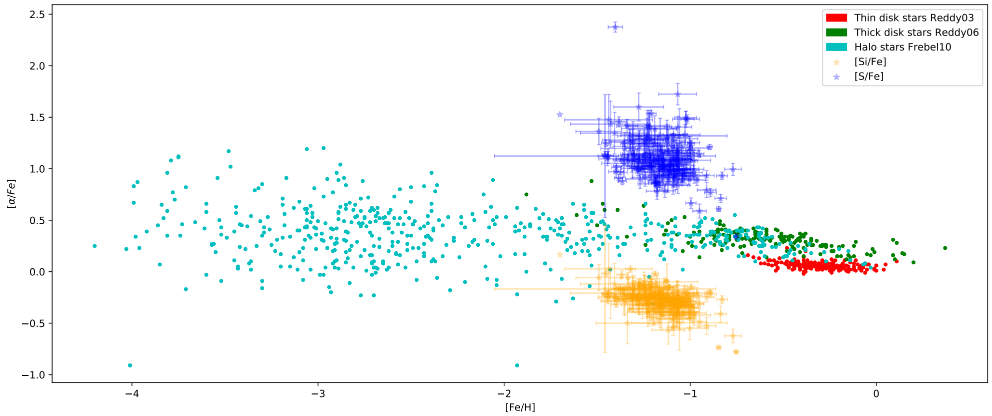

Figure E.1: Relative abundance of [Si/Fe]. Circles show [α/Fe] from the atmosphere of stars, they were obtained from literature. In cyan are stars in the Halo Frebel 2010; in green are stars found in the thick disk Reddy et al. 2006, and in red stars found in the Thin disk Reddy et al. 2003. Stars show the measured [α/Fe] measured with AODM from this work. Orange stars show [Si/Fe] and blue stars are [S/Fe].

Annex F

Identified lines at higher z

Ion	Line	Wavelength (Å)	f-value	Ref	Ion	Line	Wavelength (Å)	f-value	Ref
H I	λ1215	1215.6700	4.1640e-01	1	Mn II	λ2606	2606.4620	1.9800e-01	1
...	...	...	...	...	N II	λ1083	1083.9937	1.1100e-01	1
H I	λ911	911.7633	0.630e-17	5	Ni II	λ1370	1370.1320	7.6900e-02	1
O I	λ1302	1302.1685	4.8000e-02	1	Ni II	λ1709	1709.6042	3.2400e-02	1
O I	λ1355	1355.5977	1.1600e-06	1	Ni II	λ1741	1741.5531	4.2700e-02	1
B II	λ1362	1362.4610	1.0100e+00	3	Ni II	λ1751	1751.9157	2.7700e-02	1
C II	λ1036	1036.3367	1.1800e-01	1	S II	λ1250	1250.5780	5.4300e-03	1
C II	λ1334	1334.5323	1.2800e-01	1	S II	λ1253	1253.8050	1.0900e-02	1
Co II	λ1466	1466.2110	3.1000e-02	1	S II	λ1259	1259.5180	1.6600e-02	1
Co II	λ1574	1574.5508	2.5000e-02	1	Si II	λ1190	1190.4158	2.9200e-01	1
Co II	λ1941	1941.2852	3.4000e-02	1	Si II	λ1193	1193.2897	5.8200e-01	1
Co II	λ2012	2012.1664	3.6800e-02	1	Si II	λ1260	1260.4221	1.1800e+00	1
Fe II	λ1142	1142.3656	4.0100e-03	1	Zn II	λ2026	2026.1370	5.0100e-01	1
Fe II	λ1143	1143.2260	1.9200e-02	1	Zn II	λ2062	2062.6640	2.5300e-01	4
Fe II	λ1144	1144.9379	8.3000e-02	1	Si III	λ1206	1206.5000	1.6300e+00	1
Fe II	λ1608	1608.4511	5.7700e-02	1	C IV	λ1548	1548.2040	1.8990e-01	1
Mg II	λ2796	2796.3543	6.1550e-01	1	C IV	λ1550	1550.7810	9.4750e-02	1
Mg II	λ2803	2803.5315	3.0580e-01	1	Si IV	λ1393	1393.7602	5.1300e-01	1
Mn II	λ1197	1197.1840	2.1700e-01	1	Si IV	λ1402	1402.7729	2.5400e-01	1
Mn II	λ1199	1199.3910	1.6900e-01	1	O VI	λ1031	1031.9261	1.3250e-01	1
Mn II	λ2576	2576.8770	3.6100e-01	1	O VI	λ1037	1037.6167	6.5800e-02	1
Mn II	λ2594	2594.4990	2.8000e-01	1					

Table F.1: Ions identified in Section 3.2.1. Element and ion is show in Ion column, wavelength is in Angstrom, Ref is the reference number from which I got these values. Ref numbers are: 1 = citeMorton03, 2 = citeMorton00, 3= citeVerner96, 4= citeVerner94, 5= citeALIS

Annex G

Full table of QSO used here

ID	Glon (°)	Glat (°)	S/N	z	ID	Glon (°)	Glat (°)	S/N	z	ID	Glon (°)	Glat (°)	S/N	z
J141949.39+060654.0	351.9189	60.2851	6.8	1.648	B0120-28	227.7754	-82.9332	16.5	0.436	2XMM-J100420.0+051300	234.161	44.6222	11.4	0.161
PG-1630+377	60.3421	42.9393	36.8	1.478	SDSSJ110406.94+314111.4	195.4121	66.2495	9.1	0.435	PG1424+240	29.4874	68.2076	20.1	0.16
HB89-0232-042	174.4627	-56.1555	17.5	1.437	PG1222+216	255.0733	81.6598	19.1	0.432	PG1115+407	172.2337	66.6686	24.0	0.154
PG-1522+101	14.8922	50.1217	22.6	1.328	SDSSJ143511.53+360437.2	61.523	66.2579	5.7	0.429	PG0052+251	123.9075	-37.4378	24.7	0.154
LBQS-1435-0134	348.7184	51.3746	31.1	1.31	SDSSJ004222.29-103743.8	115.129	-73.3631	6.5	0.424	2MASX-J10053271-2417161	261.2302	24.8511	6.7	0.153
SDSS-J135726.27+043541.4	340.7675	62.5141	10.0	1.234	SDSSJ111754.31+263416.6	209.1002	69.16	7.9	0.422	PG1352+183	4.3748	72.8738	25.4	0.152
HE0435-5304	261.0247	-41.3746	11.5	1.231	CTS487	5.5445	-69.4435	19.0	0.42	SDSSJ232259.98-005359.2	80.2738	-56.2637	8.8	0.15
PG-1338+416	90.587	72.4837	16.6	1.217	SDSSJ133045.15+281321.4	42.3677	81.2298	7.5	0.417	SDSSJ135712.61+170444.1	2.8604	71.7802	14.8	0.15
PG-1206+459	144.6291	69.6209	22.8	1.164	SDSSJ110312.93+414154.9	172.5526	63.5238	7.6	0.403	RXSJ00537+2232	123.638	-40.3291	9.8	0.148
FIRST-J020930.7-043826	165.9922	-60.8074	10.4	1.128	SDSSJ153644.90+141229.7	22.878	49.4473	5.7	0.399	SDSSJ094733.21+100508.7	225.3726	43.5395	10.9	0.139
SDSS-J100535.24+013445.7	238.5271	42.7859	10.5	1.08	SDSSJ011623.04+142940.5	131.9646	-47.9392	6.3	0.395	PKS0558-504	257.9622	-28.5693	18.3	0.137
VV2006-J092542.3+344108	189.9464	45.7029	7.6	1.067	SDSSJ121037.56+315706.0	181.9613	79.9045	6.0	0.389	RXSJ0155.6+3115	138.7027	-29.6442	11.8	0.135
HE0439-5254	260.6931	-40.9014	16.9	1.053	HB89-0202-765	297.5486	-40.0452	8.1	0.389	IO-AND	122.2786	-23.1812	36.2	0.134
LBQS-0107-0235	134.0062	-64.7985	10.8	0.957	SDSS-J104741.75+151332.2	229.0848	58.908	23.2	0.385	PG1626+554	84.5149	42.1886	29.1	0.133
HB89-0107-025-NED05	134.0292	-64.7794	11.4	0.956	SDSSJ134246.89+184443.6	0.2433	75.525	7.5	0.383	VIIZW244	136.6575	32.6778	29.3	0.131
PG-1407+265	34.6687	72.5886	38.8	0.94	SDSSJ123335.07+475800.4	131.2436	68.8723	8.5	0.382	QSO-B1215+303	188.8749	82.0529	25.2	0.13
SDSSJ112244.89+575543.0	143.6452	55.4883	6.2	0.906	SDSSJ024250.85-075914.2	182.1522	-57.4171	6.4	0.377	MRK876	98.2694	40.3757	72.2	0.129
SDSSJ141910.20+420746.9	78.5766	66.6566	5.7	0.874	SDSSJ122035.10+385316.4	149.7092	76.592	5.3	0.376	IRAS-L06229-6434	274.3115	-27.3195	31.8	0.128
VV2006-J095243.0+515121	163.927	48.5444	9.1	0.862	SDSSJ132222.68+464535.2	107.7083	69.4433	7.2	0.374	MRK106	161.1387	42.8795	27.1	0.123
Q2251+155	86.111	-38.1839	5.4	0.859	3C48	133.9626	-28.7194	14.9	0.367	RBS2005	97.9384	-36.7987	14.6	0.12
SBS1122+594	141.8033	54.7097	11.9	0.851	SDSSJ094952.91+390203.9	183.5185	50.5948	10.4	0.366	HS-0033+4300	120.0257	-19.5089	5.1	0.12
SDSSJ101622.60+470643.3	169.0288	53.7423	6.7	0.822	1ES1553+113	21.9089	43.9642	34.9	0.36	RXJ1230.8+0115	291.2603	63.6598	64.9	0.117
VV2006-J222836.3-095009	53.2369	-52.1801	8.7	0.797	1ES1028+511	161.4385	54.4393	18.8	0.36	TONS210	224.9715	-83.1603	43.5	0.116
SDSS-J141038.39+230447.1	24.5712	71.6404	10.3	0.795	PG1049-005	252.2763	49.8783	10.5	0.359	IRAS-F04250-5718	266.9868	-41.9963	83.1	0.104
SDSSJ234500.43-005936.0	88.7929	-59.3884	6.4	0.79	B0117-2837	225.7307	-83.6507	23.1	0.348	UKS-0242-724	291.8094	-42.3515	15.4	0.101
SDSSJ102218.99+013218.8	242.16	46.0656	6.7	0.79	RXJ2154.1-4414	355.1792	-50.8646	27.3	0.344	PG0804+761	138.2789	31.0327	65.1	0.1
SDSSJ100102.55+594414.3	152.5697	46.3865	10.8	0.747	PG1216+069	281.0714	68.1433	22.5	0.331	IRAS-F22456-5125	338.5115	-56.6295	55.3	0.1
VV2006-J125901.7+413055	117.238	75.5287	9.6	0.745	SDSSJ092554.43+453544.4	174.3152	45.5962	12.0	0.329	2MASS-J10155924-2748289	265.6586	23.5932	5.3	0.1
SDSSJ091440.38+282330.6	198.1323	42.4466	7.4	0.735	PG0832+251	199.4907	33.1462	10.9	0.329	SDSSJ123235.82+060310.0	290.0851	68.4533	12.0	0.083
SDSSJ155304.92+354828.6	57.2591	50.6668	7.2	0.722	PG1001+291	200.0835	53.2069	20.3	0.327	SDSSJ031027.82-004950.7	180.5367	-47.5388	9.1	0.08
SDSSJ155504.39+362848.0	58.3163	50.2662	5.7	0.714	SDSSJ134251.60-005345.3	328.819	59.3665	8.4	0.326	RXSJ00437+3725	121.2326	-25.4243	17.5	0.079
SDSSJ124511.25+335610.1	133.7244	83.0607	5.8	0.711	SDSSJ120720.99+262429.1	214.6163	80.1361	6.7	0.322	RBS1666	358.7327	-31.0031	20.1	0.079
SDSSJ113457.62+255527.9	212.6185	72.8679	6.9	0.709	SDSSJ082633.51+074248.3	216.8903	24.6341	7.4	0.31	PKS2005-489	350.3731	-32.6008	22.6	0.071
SDSSJ144511.28+342825.4	56.7398	64.5904	5.9	0.697	S50716+714	143.981	28.0176	35.4	0.3	RBS563	272.2534	-39.2259	14.6	0.069
PKS0552-640	273.4656	-30.6114	29.7	0.68	RXS-J23218-7026	313.2924	-44.8373	31.8	0.3	SDSSJ145108.76+270926.9	39.9451	63.4336	8.5	0.065

Table G.1: COS-GAL QSOs used here. Columns from left to right are: ID name as they appear in HSLA first data release Peeples et al. 2017 , Galactic longitude in degrees, Galactic latitude in degrees, S/N ratio as reported in HSLA first data release.

ID	Glon (°)	Glat (°)	S/N	z	ID	Glon (°)	Glat (°)	S/N	z	ID	Glon (°)	Glat (°)	S/N	z
3C57	173.0773	-67.2617	24.3	0.67	TON580	194.9413	72.0306	20.4	0.289	MRK1148	123.0933	-45.4387	19.6	0.064
SDSSJ105958.82+251708.8	210.811	64.9832	7.9	0.662	4C25.01	114.0722	-36.2766	15.3	0.284	CAL-F-COPY	277.1769	-35.4212	16.9	0.064
SDSSJ080908.13+461925.6	173.3223	32.2889	11.6	0.658	PKS1302-102	308.5914	52.1613	27.4	0.278	1H1613-097	3.5308	28.4585	9.5	0.064
PKS0637-752	286.3684	-27.1584	24.8	0.653	2MASX-J16194054+2543233	43.5891	43.7	9.1	0.269	MR2251-178	46.1974	-61.3256	36.1	0.063
3C263	134.1592	49.744	37.4	0.646	Q1545+210	33.8982	49.4575	17.2	0.264	RBS144	299.4835	-65.836	22.1	0.062
VV2006-J115412.1+463552	149.2708	67.4951	8.4	0.642	SDSSJ134206.56+050523.8	333.8871	64.8712	8.5	0.263	MRK1513	63.6699	-29.07	30.1	0.062
SDSSJ105945.23+144142.9	232.8312	61.2037	9.1	0.631	SDSSJ115758.72-002220.8	275.7139	59.6441	6.9	0.26	RXSJ00508+3536	122.7965	-27.2596	17.3	0.058
HE0238-1904	200.4801	-63.6337	26.9	0.631	QSO-B0952+457	173.1141	50.7408	7.3	0.259	PG1011-040	246.5011	40.7487	29.7	0.058
PMNJ2345-1555	65.6728	-70.9852	14.5	0.621	FBQSJ1010+3003	198.4271	54.6252	15.5	0.256	IZW1	123.7485	-50.175	25.0	0.058
Q0349-146	205.4845	-46.3249	14.9	0.616	RXJ0439.6-5311	261.216	-40.9268	16.9	0.243	1H-2129-624	331.1426	-42.523	35.6	0.058
GALEX-J022614.4+001530	166.5701	-54.3763	9.6	0.615	SDSSJ133053.27+311930.5	61.2799	80.4299	9.0	0.242	MRK-1253	246.6971	42.3646	8.6	0.049
SDSSJ225738.20+134045.4	85.2834	-40.7284	5.5	0.594	ICRF-J122011.8+020342	284.9919	63.84	14.6	0.24	ZW535.012	120.1742	-17.1262	16.8	0.047
SDSSJ095000.73+483129.3	168.9598	49.0984	6.8	0.589	SDSSJ213357.89-071217.3	46.5909	-39.2102	7.2	0.239	FAIRALL9	295.0729	-57.8266	40.0	0.047
SDSSJ124154.02+572107.3	125.4838	59.7289	8.2	0.583	SDSSJ092909.79+464424.0	172.5843	46.01	16.0	0.239	KAZ238	110.9649	-28.3522	7.5	0.043
PKS0405-123	204.9271	-41.7563	78.2	0.572	PG0953+414	179.7861	51.7091	39.6	0.234	NGC-985	180.8371	-59.4902	44.8	0.042
SDSSJ040148.98-054056.5	196.4159	-39.9697	7.4	0.57	NEWQZ026	92.3171	-70.888	5.4	0.228	RBS2055	106.6723	-34.6585	19.8	0.04
VV2006-J095240.2+515250	163.8954	48.5293	10.7	0.554	PG1121+422	167.2577	66.8587	18.2	0.225	MRK1179	148.8953	-29.7454	6.9	0.037
SDSSJ025937.46+003736.3	176.1811	-48.5328	6.6	0.535	RXSJ01188+3836	128.7826	-23.9549	9.7	0.216	ESO-141-55	338.1834	-26.7112	38.0	0.037
VV2006-J101541.1+594445	151.1512	47.9586	8.8	0.526	FBS0150+396	135.5828	-21.4226	6.2	0.211	MRK841	11.2091	54.6321	18.2	0.036
SDSSJ113327.78+032719.1	261.3508	59.8747	5.7	0.524	SDSSJ123604.02+264135.9	219.2929	86.5458	6.0	0.209	MRK1392	2.754	50.264	27.7	0.036
HS1102+3441	188.5633	66.2186	18.7	0.508	RBS1892	345.8979	-58.3672	19.9	0.2	MARK509	35.9711	-29.8554	103.7	0.034
PHL1598	40.5381	-40.9564	15.4	0.501	PHL2525	80.6834	-71.3172	18.0	0.198	RXS-J00057-5007	320.7101	-65.4054	27.8	0.033
RXJ0028.1+3103	117.0873	-31.5443	10.8	0.5	PHL1811	47.4732	-44.8152	41.9	0.19	MRK817	100.2997	53.4783	47.4	0.031
SDSSJ155048.29+400144.9	63.9644	50.94	6.5	0.497	2MASX-J01013113+4229356	124.9137	-20.3398	7.4	0.19	MRK-279	115.0415	46.8647	7.1	0.03
HE0226-4110	253.9407	-65.7748	36.8	0.493	PMNJ1103-2329	273.1895	33.0796	15.6	0.186	ESO292-G24	334.8992	-68.1571	22.3	0.03
SDSSJ094840.08+580039.1	155.8267	45.7313	6.4	0.491	PDS456	10.3922	11.1635	9.3	0.184	MRK290	91.4892	47.9536	23.4	0.029
SDSSJ085116.14+424328.8	178.4853	39.4838	6.3	0.481	RXS-J21388-3828	4.5093	-48.4647	23.0	0.182	ESO-031–G-008	290.3276	-40.7937	8.3	0.027
QSO-B1139+305	197.1451	74.513	5.9	0.481	PG1116+215	223.3597	68.2091	45.0	0.176	MRK-335	108.7632	-41.4245	33.4	0.025
PG1259+593	120.5556	58.0478	35.5	0.477	SDSSJ021218.32-073719.8	171.1493	-62.6554	8.2	0.173	AKN-564	92.1385	-25.3368	7.7	0.024
SDSSJ161916.54+334238.4	54.5935	45.1764	11.5	0.471	RBS2000	350.1952	-67.5845	17.3	0.173	ESO462-G09	11.3254	-31.9488	7.9	0.019
SDSSJ123304.05-003134.1	293.114	61.9949	11.0	0.47	1SAXJ1032.3+5051	161.3704	54.5903	9.1	0.173	NGC-5548	31.9606	70.4958	165.8	0.017
SDSSJ082024.21+233450.4	199.8037	29.4163	7.9	0.47	SDSSJ134231.22+382903.4	82.8658	74.4054	9.9	0.171	NGC-7469	83.0986	-45.4667	64.0	0.016
SDSS-J141309.14+092011.2	354.0969	63.759	16.2	0.46	SDSSJ121114.56+365739.5	161.2592	77.0081	9.7	0.171	MRK-1044	179.6945	-60.4774	21.9	0.016
SDSSJ100902.06+071343.8	232.656	46.6973	5.1	0.456	PG1048+342	190.6024	63.4374	21.6	0.167	MRK352	125.0262	-31.0104	7.0	0.014
HE0153-4520	271.7958	-67.975	27.5	0.451	IRASF00040+4325	114.4161	-18.4214	23.7	0.166	NGC7714	88.2156	-55.5642	19.4	0.009
TON236	44.4333	55.3506	18.0	0.45	PG1202+281	205.9628	79.6131	6.4	0.165	NGC-3783	287.456	22.9475	30.3	0.009
PG0003+158	107.3184	-45.3258	24.2	0.45	SDSSJ135625.55+251523.7	29.2703	75.3127	7.7	0.164	NGC-3516	133.2357	42.4028	17.8	0.008
SDSSJ080359.23+433258.4	176.3972	30.995	6.1	0.448	NEWQZ008	165.7166	-66.3445	8.1	0.164	NGC-4051	148.8831	70.0851	19.6	0.002
3C-66A	140.143	-16.7669	23.8	0.444	HE0056-3622	293.7191	-80.898	28.8	0.164					
SDSSJ161649.42+415416.3	66.2768	45.9124	6.5	0.441	SDSSJ095915.65+050355.1	233.37	43.4835	10.8	0.162					

Table G.2: Continuation for Table G.1.

Annex H

High velocity cloud detections

High Velocity Clouds (HVCs) are defined as gaseous structures observed in H I 21 cm radio emission on as line absorption absorption against extra-galactic background sources at LSR velocities $|v_{LSR}| > 90\,\text{km/s}$ Richter et al. 2017. Having fit voigt profiles to all velocity component present in a velocity range of $|v_{LSR}| < 300\text{km/s}$ It's possible to find the detection rate of HVC in this sample, and compare it to the results of Richter et al. 2017, where they did visual inspection in almost exactly the same sample of spectra.

Table H.1 characterizes known HVC complexes around the MW, this is part of Table 3 from Richter et al. 2017, who compiled these characteristics from literature papers therein. The last column is the detection rate from the the Voigt profile fits from this work.

The spectra sample used in Richter et al. 2017 is a QSO+Galaxy COS spectra subsample from the HSLA, where S/N> 6 and had coverage in both G130 and G160 gratings. The main difference in this sample with the one used here is that here the S/N cutoff is 5, and I only used QSO spectra. For the detection rate $= \frac{N_{det}}{N_{tot}}$ the total number of sightlines is the number of sightlines that are pointing within the galactic coordinates of an HVC complex as described in Table H.1, and one of these sightlines is considered to have an HVC detection when at least one velocity component in the fitted absorption profile has $|v_{LSR}| > 90\,\text{km/s}$.

The detection rate here is 72.1% and the reported detection rate in Richter et al. 2017 is 80.2%. They aren't far off and I attribute the difference to them using a larger sample of spectra, but it could also be that visual inspection is not as accurate as this method.

The effects of HVCs to the overall metallicity in a sightline is not looked into further in this work.

HVC complex	l_{min} (°)	l_{max} (°)	b_{min} (°)	b_{max} (°)	v_{min} (km/s)	v_{max} (km/s)	Det. rate(Richter 2017)	Det. rate (This work)
Complex GCN	0	60	-60	-30	-350	-100	2/2	3/5
Complex GCP (Smith Cloud)	0	60	-30	0	80	200	1/1	1/1
Magellanic Stream (MS)	0	180	-90	-60	-500	-80	41/46	41/55
	60	120	-60	0	-500	-80		
	180	360	-90	-60	80	500		
	210	360	-60	-30	150	500		
	210	300	-30	0	150	500		
Leading Arm (LA) of MS	300	360	-30	0	150	500	8/10	4/5
	240	360	0	60	150	500		
Complex C	40	90	15	45	-250	-80	31/32	9/9
	60	110	25	65	-250	-80		
	110	150	35	65	-250	-80		
Outer Arm (OA)	45	90	0	15	-150	-80	0/0	0/0
	90	160	0	20	-150	-80		
Complex G	60	105	-20	0	-150	-80	0/0	0/0
Complex H	105	150	-20	20	-250	-80	2/2	4/4
Complex M	120	200	45	75	-150	-80	12/24	19/30
Complex A	145	175	30	45	-250	-140	5/6	3/5
	130	145	20	35	-250	-140		
Anti-Center (AC)	130	200	0	-60	-500	-80	2/6	0/0
AC Shell + ACO	160	210	-20	20	-130	-80	0/0	0/0
Complex WE	290	340	-30	0	80	150	0/1	0/1
Complex WA + WB	210	260	0	60	80	200	21/25	7/10
HVC toward LMC	275	285	-38	-28	80	150	0/0	1/1
Complex L	300	360	20	60	-200	-80	5/7	1/3
Total							130/162∼80.2%	93/129∼72.1%

Table H.1: HVC detection rate table and characteristics of HVC from Richter et al. 2017